Role of the organic cation in hybrid halide perovskites

A computational study

Maheswari, Sudeep

DOI
10.4233/uuid:bcd8f7e7-55f5-43d1-a90f-4679603dcbe5

Publication date
2019

Document Version
Final published version

Citation (APA)
Maheswari, S. (2019). *Role of the organic cation in hybrid halide perovskites: A computational study*. [Dissertation (TU Delft), Delft University of Technology]. https://doi.org/10.4233/uuid:bcd8f7e7-55f5-43d1-a90f-4679603dcbe5

ROLE OF THE ORGANIC CATION IN HYBRID HALIDE PEROVSKITES:

A COMPUTATIONAL STUDY

ROLE OF THE ORGANIC CATION IN HYBRID HALIDE PEROVSKITES:

A COMPUTATIONAL STUDY

Proefschrift

ter verkrijging van de graad van doctor
aan de Technische Universiteit Delft,
op gezag van de Rector Magnificus Prof. dr. ir. T. H. J. J. van der Hagen,
voorzitter van het College voor Promoties,
in het openbaar te verdedigen op dinsdag 10 september 2019 om 15:00 uur

door

Sudeep MAHESHWARI

Master of Science in Chemistry,
Indian Institute of Science Education and Research, Mohali, India,
geboren in Farrukhabad, India.

Dit proefschrift is goedgekeurd door de

Samenstelling promotiecommissie:

Rector Magnificus,	voorzitter
Prof. dr. L. D. A. Siebbeles	Technische Universiteit Delft, promotor
Dr. F. C. Grozema	Technische Universiteit Delft, promotor
Onafhankelijke leden:	
Prof. S. J. Picken	Technische Universiteit Delft
Prof. dr. F. M. Mulder	Technische Universiteit Delft
Prof. dr. J. M. V. A. Koelman	Technische Universiteit Eindhoven
Dr. T. L. C. Jansen	De Rijksuniversiteit Groningen
Overige leden:	
Dr. Jörg Meyer	De Universiteit Leiden

Printed by: GVO Drukkers & Vormgevers

Front & Back: Cover art designed by the author and drs. Ineke Jansen.

ISBN 978-94-6332-547-9

An electronic version of this dissertation is available at
http://repository.tudelft.nl/.

It is not knowledge, but the act of learning
not perfection but the act of getting there,
which grants the greatest enjoyment.

Carl Friedrich Gauß

CONTENTS

1 Introduction: Hybrid Halide Perovskites **1**
- 1.1 Hybrid halide perovskites as next-generation solar cell materials . . . 2
- 1.2 General structure and stability of perovskite materials . . . 3
- 1.3 Electric and optical properties . . . 5
  - 1.3.1 3-dimensional HHPs: electronic structure and charge transport . . . 5
  - 1.3.2 Low dimensional HHps: structure and optoelectronic properties . . . 7
- 1.4 Research aim and outline of this thesis . . . 8

References . . . 11

2 Effect of dipoles on electronic structure **15**
- 2.1 Introduction . . . 16
- 2.2 Methods . . . 18
- 2.3 Results and discussion . . . 19
  - 2.3.1 Effect of cation substitution on lattice size and band gap . . . 19
  - 2.3.2 Effect of dipole orientations . . . 20
  - 2.3.3 Localization effects due to dipole orientations . . . 21
- 2.4 Conclusions . . . 26

References . . . 28

3 Rotational dynamics and phase transitions **31**
- 3.1 Introduction . . . 32
- 3.2 Methodology . . . 33
  - 3.2.1 Molecular Dynamics . . . 33
  - 3.2.2 Monte Carlo . . . 34
  - 3.2.3 Domain detection . . . 35
- 3.3 Results and Discussion . . . 35
  - 3.3.1 Methylammonium lead iodide (MAPI) . . . 35
  - 3.3.2 Formamidinium lead iodide (FAPI) . . . 41
- 3.4 General discussion and conclusions . . . 47

References . . . 48

4 Mixed cation perovskites **51**
- 4.1 Mixed organic cation hybrid perovskites . . . 52
- 4.2 Methodology . . . 53
- 4.3 Discussion . . . 55
  - 4.3.1 Mixed $MA_{0.5}FA_{0.5}PbI_3$ configurations . . . 55
  - 4.3.2 Energy analysis of confurations . . . 56
  - 4.3.3 Deformation of Pb-I cage . . . 56
  - 4.3.4 Rotational-autocorrelation of MA and FA cation motion . . . 57

4.4 Conclusion . . . 57
References . . . 60

5 Computational design of 2D perovskites **63**
5.1 Introduction . . . 64
5.2 Computational Methods . . . 65
5.3 Results and Discussion . . . 66
5.3.1 $(C_4H_9\text{-}NH_3)_2BTBT$ . . . 67
5.3.2 $(C_4H_9\text{-}NH_3)_2PDI$ and $(C_4H_9\text{-}NH_3)_2NDI$ . . . 69
5.3.3 Charge transport properties . . . 70
5.4 Conclusion . . . 71
References . . . 72

6 One-dimensional hybrid halide perovskites derivatives **75**
6.1 Introduction . . . 76
6.2 Computational Methods . . . 77
6.3 $2,5\text{-DMASnI}_3$ . . . 77
6.3.1 Structure of $2,5\text{-DMASnI}_3$ . . . 77
6.3.2 Electronic structure of $2,5\text{-DMASnI}_3$ . . . 78
6.4 $2,5\text{-DMAI}_3$ . . . 79
6.4.1 Structure of $2,5\text{-DMAI}_3$ . . . 79
6.4.2 Electronic structure of $2,5\text{-DMAI}_3$ . . . 80
6.5 $(PyrC4{:}TCNQ)Pb_2I_8$ . . . 81
6.5.1 Introduction of charge transfer complex PyrC4:TCNQ . . . 81
6.5.2 Structure of $(PyrC4{:}TCNQ)Pb_2I_8$ . . . 81
6.5.3 Electronic structure of $(PyrC4{:}TCNQ)Pb_2I_8$ . . . 81
References . . . 84

Summary **85**

Samenvatting **89**

Acknowledgements **93**

A Appendix to chapter 3 **95**
A.1 Molecular dynamics parameters . . . 95
A.2 Directional scatter plots . . . 95
References . . . 103

Curriculum Vitæ **105**

List of Publications **107**

1

INTRODUCTION: HYBRID HALIDE PEROVSKITES

1

1.1. HYBRID HALIDE PEROVSKITES AS NEXT-GENERATION SOLAR CELL MATERIALS

One of the most important challenges currently faced by the modern society is the rapidly increasing need for energy. Until now this increasing need has been met by an increased usage of fossil fuels, however, this is not a sustainable solution. Rapid decrease of available oil reserves and negative environmental impact of using fossil fuels, for instance emission of green house gasses render fossil fuels unsustainable. The prime renewable source of energy is solar energy, which, if exploited sufficiently could provide the majority of our energy demands. This can be either by direct generation and use of electrical energy and by intermediate storage in the form of batteries or fuels. The major part of commercially supplied solar panels for direct energy conversion in the form electricity is based on silicon technology. However, silicon based solar cells have some important drawbacks, including relatively high production costs and a maximum efficiency that has not significantly improved over the last decades. Therefore, there is a continuing search for alternative materials and processes to reach higher conversion efficiencies, lighter and more flexible devices and lower production costs.

Hybrid halide perovskites (HHPs) are currently the most studied new materials for solar cell applications. In 2009 the first device using a HHP as the active material was constructed and had a overall power conversion efficiency of 3.8%. [1] In the ten years following this initial demonstration the efficiency has steadily increased and currently the best HHP-based cells have an efficiency of 24% [2] in single junction architectures. In addition, perovskite materials are also widely explored in the context of tandem architectures where an HHP-based cell is combined with another, more common, cell, most notably silicon-based. For such HHP-silicon tandem cells efficiencies have been reached up to 28%, surpassing the maximum reached efficiency of the best silicon-based single junction cells.[3] The development of HHP-based cells constitute the fastest increase in efficiency in photovoltaics, and the continuing improvement suggests that there is still room for substantially higher efficiencies. The high efficiencies, combined with the low processing costs already make HHP cells commercially interesting, especially in tandem configurations. While their application in photovoltaics is the main driver for research on HHP materials, they are also of interest as versatile, tunable semiconductors for other applications, for instance X-ray detectors and light emitting diodes (LEDs)[4–6]. In these application they can be either applied in the bulk solid 3D form, but in many case they are also used in the form of quantum dots or two-dimensional materials. For all these applications, it is of considerable interest to establish a detailed insight between the structure of HHP materials and their electronic properties, which is the central aim of this thesis. In the following sections, some of the basic properties of HHP materials are discussed, together with a brief outline of the contents of this thesis.

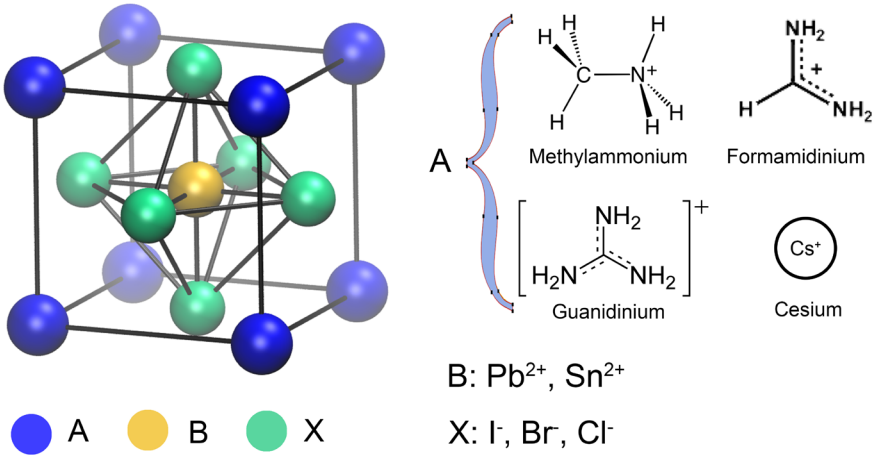

Figure 1.1: Schematic crystal structure of the ABX3 perovskite structure. In hybrid halide perovskites, A represents the organic cation (e.g. MA+, FA+), B the divalent metal (e.g. Pb2+, Sn2+) and X the halide (e.g. Cl-, Br-, I-).

1.2. GENERAL STRUCTURE AND STABILITY OF PEROVSKITE MATERIALS

Perovskites are crystalline materials that have the same crystal structure as calcium titanium oxide ($CaTiO_3$) with a general the chemical formula ABX_3, in which A and B are cations and X represents an anion. They are named after the Russian mineralogist L.A. Perovski who discovered the mineral form of $CaTiO_3$ in 1839.[7] Approximately two thousand of such perovskite materials are currently known to exist and theoretically many more have been predicted to be stable.[8] These materials exhibit a range of physical properties that are interesting in materials science, including superconductivity, magnetoresistance and a range of dielectric properties, making them valuable for application in electronic devices.[9–11] The sub-class of perovskites that we are interested in in this thesis, the hybrid halide perovskites (HHPs) have a general structure where the B ion is a doubly charged metal cation (Pb^{2+}, Sn^{2+}), X is a halide anion (I^-, Br^- or Cl^-) and A is a singly charged organic cation. The most studied example is methylammonium lead iodide (MAPI), which was the first perovskite to be considered for photovoltaic applications. The first synthesis of HHPs can be dated back to 1882[12]. Research on the fundamental optoelectronic properties of the crystalline three-dimensional HHPs was initiated by Weber and co-workers.[6, 13] The general crystal structure of HHPs is shown in Figure 1.1 and consist of a cubic lattice in which the monovalent cation A occupies the interstices formed by BX_6 octahedra. The possibility to form a stable cubic perovskite structure depends on the ionic radii of A, B and X according to the Goldsmith tolerance factor given in Equation 1.1. In this equation the r_A, r_B and r_X are the ionic radii of the species A, B and X, respectively.

$$t = \frac{r_A + r_X}{\sqrt{2} * (r_B + r_X)} \tag{1.1}$$

In terms of this Goldsmith factor[14], an undistorted crystal structure exists if $t \approx 1$, resulting in a cubic structure with a B-X-B angle of 180°. If $t < 1$, somewhat distorted tetragonal and orthorhombic phases arise. Transitions between the cubic, tetragonal and orthorhombic phases can be induced by changes in temperature, pressure and surrounding electric field. These low symmetry structures often have distorted BX_6 octahedra.[15]

If the A cation becomes too large, resulting in $t > 1$, no stable three-dimensional structure can be formed. In many case for $t > 1$ stable crystalline structures are found but they are of lower dimensionality. A major class of such lower dimensional materials are the two-dimensional HHPs. The group of Mitzi have pioneered the synthesis and characterization of such 2D HHPs in the 1990s and has explored their applicability in devices, for instance field effect transistors.[16] When combining large organic cations such as butylammonium with small ones (*e.g.* methylammonium) that fit into the metal-halide lattice it is possible to form multilayered structures where multiple layers of inorganic small-A layers are separated by the large organic cations. This leads to quantum confined systems where the electronic properties depend on the layer thickness.[17–19] In some cases, depending on the size and nature of the organic cations used, one-dimensional or zero-dimensional structures can be formed where the metal-halide octahedra are connected in one-dimensional chains or are fully disconnected.

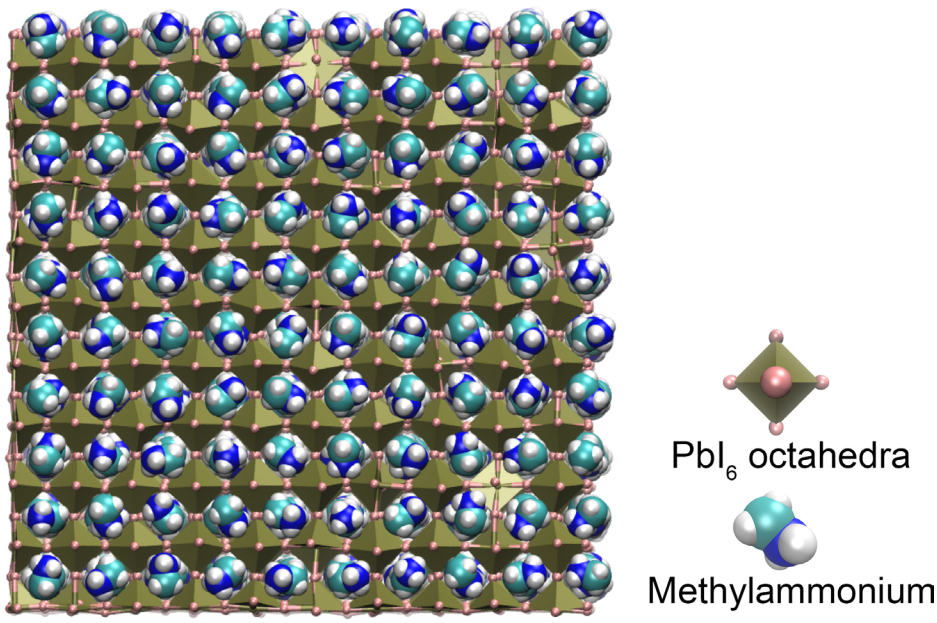

Figure 1.2: Model of $MAPbI_3$ with MA^+ cations at the interstices of PbI_6 octahedra

1.3. ELECTRIC AND OPTICAL PROPERTIES

As discussed above, perovskites can exhibit a wide range of properties that are of interest for opto-electronic applications. These properties can be tuned to a large extent by changing the composition of the materials. This is also true for the sub-class that we are interested in this thesis, the hybrid halide perovskites and their properties can be varied to achieve optimal properties for specific device applications. In the following sections, the electronic properties of hybrid halide perovskites are briefly summarized, both for the three-dimensional bulk materials and the low-dimensional materials.

1.3.1. 3-DIMENSIONAL HHPS: ELECTRONIC STRUCTURE AND CHARGE TRANSPORT

The electronic (band) structure of hybrid halide perovskites can be calculated using density functional theory (DFT) as implemented in a variety of electronic structure software packages. Typically, periodic boundary conditions are applied as such crystalline materials are characterized by electronic states that are delocalized over the whole three-dimensional structure. The value of the band gap calculated for $MAPbI_3$ using such DFT methods is 1.7 eV.[20] Experimentally, the first excitation peak in the optical absorption spectrum at room temperature is found at 1.6 eV, making it a good absorber for solar cell applications.[21] The calculated band diagram for $MAPbI_3$ in its cubic structure is shown in Figure 1.3 left.[22] The bands in green are the valence bands, while the ones in red are conduction bands. As can be seen in the band structure that the minima of direct conduction bands are slightly shifted from R-point. This splitting of conduction band leading to a slight indirect character in the band gap is due to Rashba-Dresselhaus spin-orbit coupling.[23, 24]

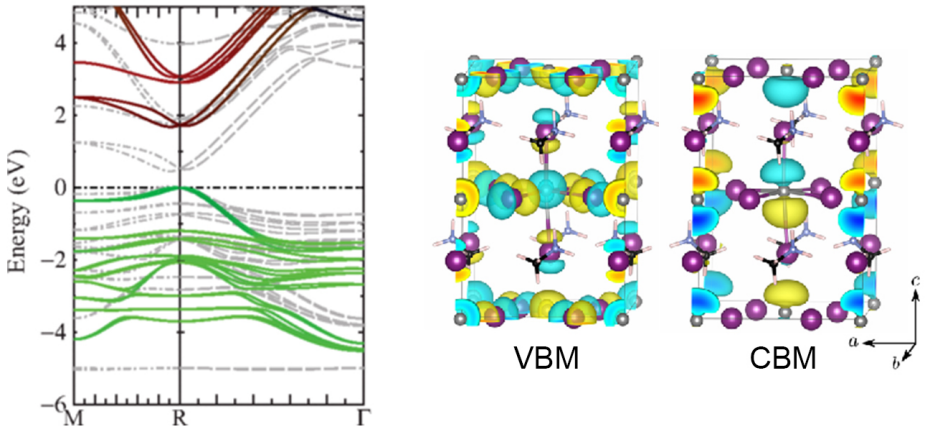

Figure 1.3: Bandstucture of methyalmmoniumleadiodide from reference [22] and charge density of this material from reference [25].

Photoexcitation of a semiconductor leads to the generation of an electron-hole pair. This pair can exist as two individual 'free' charges or they can be present as an exciton in which they are bound by Coulomb forces. Whether the charge exist as free charges or as a bound exciton depends on the exciton binding energy (EB). In materials with a high dielectric constant, the Coulomb interactions are effectively screened, resulting in low exciton binding energies and hence efficient formation of charges. In the case of a low dielectric constant, the screening is much less and a bound state is formed, which can easily decay back to the ground state radiatively. For $MAPbI_3$ in the tetragonal phase the exciton binding energy has been determined using magneto-optical measurements and a value of only 12meV has been found, explaining the exceptionally efficient formation of free charges on photoexcitation.[26] From DFT-based calculations for instance using Bethe–Salpeter equation theory considerably higher values of 45 meV higher have been found.[27–29] The exciton binding energy also depends considerably on the composition of the material. For $MAPbBr_3$ a value of 35 meV has been found. This is consistent with the trend in theoretical estimates and can be understood in terms of the reduced screening due to the smaller polarizability of the bromide compared to iodide. [30]

A relatively simple description that connects the electronic band structure to the mobility of charges in a semiconductor is the Drude model give in Equation 1.2.[31–33] In this equation e is electronic charge, τ is scattering time, m^* is effective mass and ω is the angular frequency. This equation relates the (frequency-dependent) charge carrier mobility to the effective mass of the charge and the scattering time. The effective masses of the electrons and holes can be obtained directly from the electronic band structure as the inverse of the curvature of the bands. The values of the effective mass can, at least qualitatively be compared to the experimentally observed mobility of charge carriers. Band structure calculations of different phases of $MAPbI_3$ have resulted in effective masses in the range of (0.1-0.15)m_0, in which m_0 is the rest-mass of a free electron.

$$\mu(\omega) = \frac{e\tau}{m^*}\left(\frac{1 - i\omega\tau}{1 + \omega^2\tau^2}\right) \tag{1.2}$$

A detailed analysis on the charge density distribution over the valence bands and conduction bands of $MAPbI_3$ reveals that the valence band is dominated by the iodide p-states, while the conduction band is mainly made up of the s-states in lead. This can be seen in Figure 1.3. The valence band maximum and conduction band minimum in cubic $MAPbI_3$ are at a Brillouin zone boundary; *i.e.* the R-point. This is in contrast to the sp^3-bonded semiconductors where both the valence bond maximum and the conduction band minimum occur at the gamma point. The presence of heavy atoms in $MAPbI_3$ results in significant spin-orbit coupling that has an effect on the band structure. This effect is seen in the conduction bands that are dominated by the p-orbitals of lead. Spin-orbit coupling results in reduction of theoretical band gap by approximately 1 eV and a reduction of the effective masses.[34, 35] The contribution of states in the organic cation (A) to the bands near the band gap are minor and these states have been reported to be several eV's below the valence band in the band structure. This shows that the direct contribution of these organic cations to the band structure is negligible, however, the organic cation has an effect on the geometry of the Pb-I framework. Therefore, the nature and dynamics of the organic cation has an indirect effect on the electronic properties.

1.3.2. LOW DIMENSIONAL HHPS: STRUCTURE AND OPTOELECTRONIC PROPERTIES

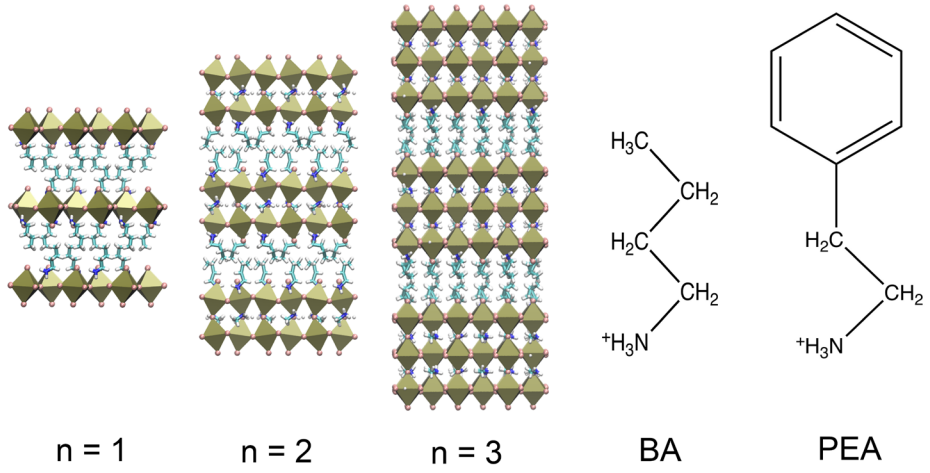

Figure 1.4: Schematic structure of the n=1,2,3 layered perovskite.

As discussed above, the formation of stable three-dimensional perovskite structure depends strongly on the nature of the organic cation A. The size of this cation can only be varied over a very small range since it has to fit into the metal-halide lattice. However, in many cases, stable periodic crystalline materials are still obtained. These are typically two- or one-dimensional. Examples of larger cations that lead to two-dimensional structures are n-butylammonium (BA^+) and phenyl-ethyl-ammonium (PEA^+) and can be seen in Figure 1.4. PEA_2PbI_4, consisting of a single layer of inorganic lead iodide octahedra capped by a layer of PEA^+ cations on the either side, was first described in the early 1990s and is one of the most studied materials for exploring the structural and optoelectronic properties of two-dimensional hybrid perovskites.[36, 37] The two-dimensional hybrid perovskites, for example PEA_2PbI_4 are characterized by a much larger band gap than their three-dimensional counterpart, 2.36 eV. Moreover, they exhibit high exciton binding energies (200-400 meV), resulting in a low yield of charges on photoexcitation and strongly excitonic behavior.[38, 39] This generally leads to high photoluminescence quantum yields in these materials and hence makes them suitable for applications such as light-emitting diodes (LEDs) or lasing.[40, 41] Quasi-two-dimensional perovskites are obtained when the large organic cation PEA^+ is mixed with a smaller organic cation that is able to form 3-dimensional structures such as MA^+. The thickness of the inorganic sheets of $PEA_2MA_{n-1}Pb_nI_{3n+1}$ can be tuned by controlling the relative stoichiometry of MA^+ and PEA^+. In $PEA_2MA_{n-1}Pb_nI_{3n+1}$ as the number of inorganic layers increase, the band gap decreases from 2.36 eV for n=1 to 1.94 eV for $n = \infty$, and with this the exciton binding energy also decreases.[37–39]

A second widely studied class of two-dimensional hybrid perovskites is based on BA^+ as the organic cation. For the pure two-dimensional material of $BA_2MA_{n-1}Pb_nI_{3n+1}$

with $n = 1$ a band gap of 2.24 eV has been reported.[42, 43] The band gap decreases to 1.52 eV for the three-dimensional materials ($n = \infty$). The absorption spectra of the $BA_2MA_{n-1}Pb_nI_{3n+1}$ series of hybrid perovskites with $n = 1-4$ exhibit peaks mainly attributable to electronic transitions inside the inorganic layers, *i.e.* from states that are a mix of *s*-orbitals on lead and *p*-orbitals on iodide to states that mainly consist of *p*-orbitals on iodide. The distortions of lead-halide octahedra, *i.e.* the Pb-X-Pb angles, affect the valence and conduction band energies, leading to a widening of the band gap and an increase in the exciton binding energy.[18, 43–45] The possibility to tune the exciton emission by varying the number of inorganic layers allows the use of two-dimensional perovskites for light emitting applications in the visible and near-infrared spectral region. PMA_2PbI_4 and PEA_2PbI_4 have been used to construct green and violet light-emitting devices respectively.[44]

The bulky organic cations BA^+ and PEA^+ have a very wide HOMO-LUMO gap, resulting in a very high tunneling barrier for transport between the different inorganic layers. This means that the charge transport perpendicular to the two-dimensional layers is very inefficient. Parallel to the layers, charge transport is much more efficient, although the effective mass of electrons and holes has been shown to be larger than for the three-dimensional materials because of the dielectric confinement.[46] These charge transport characteristics have important consequences for the application of these materials in devices. Solar cells based on two-dimensional perovskites require a good connection of the perovskite layers with the electrodes and hence require the perovskite layers to be aligned perpendicular to the electrodes. This vertical alignment of the inorganic layers is possible if the growth of the perovskite layers is guided in that direction. Another approach to improve inter-layer transport is by modifying the organic layer and introducing different organic cations that reduce the tunneling barrier between the different layers. This approach is explored in Chapter 5 of this thesis.

1.4. RESEARCH AIM AND OUTLINE OF THIS THESIS

In the preceding sections, the interesting properties of hybrid halide perovskites have been outlined. The properties are intricately linked to the geometric structure of the material. This is true for the crystal structure, but it is also clear that there are considerable structural fluctuations and disorder that can markedly affect the electronic properties. These fluctuations are in a large part due to the presence and mobile nature of the organic cations, however, the details of their effect on the electronic structure and on the phase behavior and stability are not know in detail. Important questions include the relation between the nature and dynamics of the organic cation and phase transitions; the effect of the organic cation on the electronic structure; the possibility of the formation of (localized) polarons stabilized by reorientation of the cations, and variations in the structural dynamics with temperature. Answering these questions using experimental approaches is rather difficult since in many cases the observed effects are due to the interplay of several different sources. Moreover, it is known that the observed properties are often strongly affected by subtleties in the preparation of samples and inclusion of defects can determine the opto-electronic properties to a large extent.

Computational methods are a promising approach to address these questions since

in computer simulations there is full control over the structure and specific interactions can be switched on and off to disentangle their roles. Additionally, it is possible to analyze the electronic structure and the geometric properties in detail, which is often (almost) impossible in experiments. In this thesis, two main computational techniques are used. The first of these are electronic structure calculations based on density functional theory (DFT). This allows to study the electronic band structure and the effect that changes in the geometry have on this. Such DFT calculations are performed for infinitely large periodic systems and are generally very time consuming. In practice, this means that it is impossible to use DFT methods to study large scale disorder in hybrid halide perovskites as this would involve very large repeating units in the calculations. The second approach used in this thesis involves molecular dynamics (MD) calculations, in which the interactions between atoms in the material are described in terms of an approximate force field that can be used to simulate structural and dynamic properties. Using such MD methods, it is possible to study large disordered systems and obtain ensemble properties that are averaged over relatively long time scales. This comes at the disadvantage of losing all information on the electronic structure. Nevertheless, MD simulations offer valuable insight in the dynamic properties, for instance in the context of phase transitions.

Chapter 2: In this chapter the effect of the nature and mutual orientation of organic dipoles in methylammonium lead iodide is investigated by DFT calculations. Several possible organic cations with varying dipole moment are included at the A site in the structure to replace methylammonium. It is shown, that for organic cations with a large dipole moment the mutual orientation of the dipoles has a significant effect on the band gap and the total energy of the systems. Importantly, the nature of the electronic states is shown be be strongly affected by the mutual orientation and the formation of localized states for electrons and holes is outlined.

Chapter 3: While in Chapter 2 the effect of alignment of organic dipole moments on the electronic structure is studied on a microscopic scale in systems containing up to four units cells as the repeat unit, such systems are too small to obtain a realistic insight in the possible disorder in the alignment of the organic dipoles. Therefore, in Chapter 3, the dynamics of organic cations in the perovskite structure and their role in the occurrence of phase transitions has been studied in detail by molecular dynamics simulations.

Chapter 4: Where Chapter 3 was dealing with details of the motion of organic cations in 'pure' hybrid halide perovskites, in practice, many of the best performing materials in solar cells are based on mixed-cation materials where two or more A-site cations are mixed, leading to more stable materials with optimal band gaps for solar cells. The organization of these cations when they are in the same materials is not understood and an important question is the possibility of phase separation. In this chapter we investigate models systems of materials containing two different organic cations, methylammonium and formamidinium, using the same methods as in Chapter 3 to unravel their behavior. The main conclusion is that the two types of cations have a preference for phase separation.

Chapter 5: As discussed in previous sections, increasing the size of the organic cation can result in lower-dimensional perovskite-like structures, for instance two-dimensional perovskites. The advantage of such materials is that the size of the organic cation is not dictated by Goldsmith's rule, offering the freedom to introduce (large) functional organic cations that can add new functionality in hybrid halide perovskites. In Chapter 5 we explore the introduction of such functional organic cations in two-dimensional halide perovskites using DFT calculations. It is shown that introduction of strongly electron donating or withdrawing organic cations leads to formation of localized states, either in the organic or the inorganic part of the material. It is also shown that the organic cation energy levels in the band structure can be tuned by changes in the structure of the material.

Chapter 6: Finally, in Chapter 6, some unconventional lower dimensional hybrid perovskites formed with large organic cations are explored using DFT calculations. Tin-based one-dimensional structures are formed with dimethyl aniline where the eventual structure depends very much on the synthesis conditions. Both in structures with and without tin interesting electronic properties are observed, although very different from those of two- and three-dimensional perovskites structures. A third one-dimensional perovskite-like structure that has been studied by DFT method in this chapter contains organic charge-transfer complexes. This is shown to result in the formation of charge separated states on optical excitation, with the hole in the Pb-I framework and the electron on the organic acceptor.

REFERENCES

[1] Kojima, A.; Teshima, K.; Shirai, Y.; Miyasaka, T. Organometal Halide Perovskites as Visible-Light Sensitizers for Photovoltaic Cells. *J. Am. Chem. Soc.* **2009**, *131*, 6050–6051.

[2] NREL Best Research Cell Efficiency, howpublished = https://www.nrel.gov/pv/assets/images/efficiency-chart.png, note = Accessed: 2019-03-11.

[3] Oxford PV sets world record, howpublished = https://www.oxfordpv.com, note = Accessed: 2018-12-03.

[4] Yakunin, S.; Sytnyk, M.; Kriegner, D.; Shrestha, S.; Richter, M.; Matt, G. J.; Azimi, H.; Brabec, C. J.; Stangl, J.; Kovalenko, M. V.; Heiss, W. Detection of X-ray photons by solution-processed lead halide perovskites. *Nat. Photon.* **2015**, *9*, 444.

[5] Song, J.; Li, J.; Li, X.; Xu, L.; Dong, Y.; Zeng, H. Quantum Dot Light-Emitting Diodes Based on Inorganic Perovskite Cesium Lead Halides (CsPbX3). *Adv. Mater.* **2015**, *27*, 7162–7167.

[6] Stranks, S. D.; Snaith, H. J. Metal-halide perovskites for photovoltaic and light-emitting devices. *Nat. Nanotechnol.* **2015**, *10*, 391.

[7] Richard A. Robie, J. R. F., Bruce S. Hemingway *Thermodynamic Properties of Minerals and Related Substances at 298.15 K and 1 Bar (105 Pascals) pressure and at Higher Temperatures*; U.S. Government Printing Office, 1979.

[8] Filip, M. R.; Giustino, F. The geometric blueprint of perovskites. *Proc. Natl. Acad. Sci. U.S.A.* **2018**, *115*, 5397–5402.

[9] Clearfield, A. Role of ion exchange in solid-state chemistry. *Chem. Rev.* **1988**, *88*, 125–148.

[10] Ogawa, M.; Kuroda, K. Photofunctions of Intercalation Compounds. *Chem. Rev.* **1995**, *95*, 399–438.

[11] Gamble, F. R.; Osiecki, J. H.; Cais, M.; Pisharody, R.; DiSalvo, F. J.; Geballe, T. H. Intercalation Complexes of Lewis Bases and Layered Sulfides: A Large Class of New Superconductors. *Science* **1971**, *174*, 493–497.

[12] Topsöe, H. Öfversight o.d.k. Dansk. *Vidensk. Selsk. Forh.* **1882**, *8*, 247.

[13] Kieslich, G.; Sun, S.; Cheetham, A. K. Solid-state principles applied to organic–inorganic perovskites: new tricks for an old dog. *Chem. Sci.* **2014**, *5*, 4712–4715.

[14] Goldschmidt, V. Die Gesetze der Krystallochemie. *Naturwissenschaften* **1926**, *14*, 477.

[15] Chen, Q.; Marco, N. D.; Yang, Y. M.; Song, T.-B.; Chen, C.-C.; Zhao, H.; Hong, Z.; Zhou, H.; Yang, Y. Under the spotlight: The organic–inorganic hybrid halide perovskite for optoelectronic applications. *Nano Today* **2015**, *10*, 355 – 396.

[16] Kagan, C. R.; Mitzi, D. B.; Dimitrakopoulos, C. D. Organic-inorganic hybrid materials as semiconducting channels in thin-film field-effect transistors. *Science* **1999**, *286*, 945–947.

[17] Mitzi, D. B.; Wang, S.; Feild, C. A.; Chess, C. A.; Guloy, A. M. Conducting Layered Organic-inorganic Halides Containing -Oriented Perovskite Sheets. *Science* **1995**, *267*, 1473–1476.

[18] Knutson, J. L.; Martin, J. D.; Mitzi, D. B. Tuning the Band Gap in Hybrid Tin Iodide Perovskite Semiconductors Using Structural Templating. *Inorg. Chem.* **2005**, *44*, 4699–4705.

[19] Mitzi, D. B.; Feild, C. A.; Harrison, W. T. A.; Guloy, A. M. Conducting tin halides with a layered organic-based perovskite structure. *Nature* **1994**, *369*, 467–469.

[20] G. Aulbur, W.; Jönsson, L.; W. Wilkins, J. Quasiparticle Calculations in Solids. *Solid State Phys.* **1999**, *54*.

[21] De Wolf, S.; Holovsky, J.; Moon, S.-J.; Löper, P.; Niesen, B.; Ledinsky, M.; Haug, F.-J.; Yum, J.-H.; Ballif, C. Organometallic Halide Perovskites: Sharp Optical Absorption Edge and Its Relation to Photovoltaic Performance. *J. Phys. Chem. Lett.* **2014**, *5*, 1035–1039.

[22] Brivio, F.; Butler, K. T.; Walsh, A.; van Schilfgaarde, M. Relativistic quasiparticle self-consistent electronic structure of hybrid halide perovskite photovoltaic absorbers. *Phys. Rev. B* **2014**, *89*, 155204.

[23] Whalley, L. D.; Frost, J. M.; Jung, Y.-K.; Walsh, A. Perspective: Theory and simulation of hybrid halide perovskites. *J. Chem. Phys.* **2017**, *146*, 220901.

[24] Kepenekian, M.; Robles, R.; Katan, C.; Sapori, D.; Pedesseau, L.; Even, J. Rashba and Dresselhaus Effects in Hybrid Organic–Inorganic Perovskites: From Basics to Devices. *ACS Nano.* **2015**, *9*, 11557–11567.

[25] Zheng, F.; Takenaka, H.; Wang, F.; Koocher, N. Z.; Rappe, A. M. First-Principles Calculation of the Bulk Photovoltaic Effect in CH3NH3PbI3 and CH3NH3PbI3–xClx. *J. Phys. Chem. Lett.* **2015**, *6*, 31–37, PMID: 26263087.

[26] Miyata, A.; Mitioglu, A.; Plochocka, P.; Portugall, O.; Wang, J. T.-W.; Stranks, S. D.; Snaith, H. J.; Nicholas, R. J. Direct measurement of the exciton binding energy and effective masses for charge carriers in organic-inorganic tri-halide perovskites. *Nat. Phys.* **2015**, *11*, 582 EP –, Article.

[27] Even, J.; Pedesseau, L.; Jancu, J.-M.; Katan, C. DFT and k · p modelling of the phase transitions of lead and tin halide perovskites for photovoltaic cells (Phys. Status Solidi RRL 1/2014). *Phys. Status Solidi Rapid Res. Lett.* **2014**, *8*.

[28] Zhu, X.; Su, H.; Marcus, R. A.; Michel-Beyerle, M. E. Computed and Experimental Absorption Spectra of the Perovskite CH3NH3PbI3. *J. Phys. Chem. Lett.* **2014**, *5*, 3061–3065.

[29] Godby, R. W.; Needs, R. J. Metal-insulator transition in Kohn-Sham theory and quasiparticle theory. *Phys. Rev. Lett.* **1989**, *62*, 1169–1172.

[30] Soufiani, A. M.; Huang, F.; Reece, P.; Sheng, R.; Ho-Baillie, A.; Green, M. A. Polaronic exciton binding energy in iodide and bromide organic-inorganic lead halide perovskites. *Appl. Phys. Lett.* **2015**, *107*, 231902.

[31] Drude, P. Zur Elektronentheorie der Metalle. *Ann. Phys.* **1900**, *306*, 566–613.

[32] Ashcroft, N.; Mermin, N. *Solid State Physics*; Cengage Learning, 2011.

[33] Fox, M. *Optical Properties of Solids*; Oxford University Press, 2001.

[34] Giorgi, G.; Fujisawa, J. I.; Segawa, H.; Yamashita, K. Organic - Inorganic hybrid lead iodide perovskite featuring zero dipole moment guanidinium cations: A theoretical analysis. *J. Phys. Chem. C* **2015**, *119*, 4694–4701.

[35] Whalley, L. D.; Frost, J. M.; Morgan, B. J.; Walsh, A. Impact of nonparabolic electronic band structure on the optical and transport properties of photovoltaic materials. *Phys. Rev. B* **2019**, *99*, 085207.

[36] Era, M.; Hattori, T.; Taira, T.; Tsutsui, T. Self-Organized Growth of PbI-Based Layered Perovskite Quantum Well by Dual-Source Vapor Deposition. *Chem. Mater.* **1997**, *9*, 8–10.

[37] Mitzi, D. A Layered Solution Crystal Growth Technique and the Crystal Structure of (C6H5C2H4NH3)2PbCl4. *J. Solid State Chem.* **1999**, *145*, 694 – 704.

[38] Quan, L. N.; Yuan, M.; Comin, R.; Voznyy, O.; Beauregard, E. M.; Hoogland, S.; Buin, A.; Kirmani, A. R.; Zhao, K.; Amassian, A.; Kim, D. H.; Sargent, E. H. Ligand-Stabilized Reduced-Dimensionality Perovskites. *J. Am. Chem. Soc.* **2016**, *138*, 2649–2655.

[39] Gan, X.; Wang, O.; Liu, K.; Du, X.; Guo, L.; Liu, H. 2D homologous organic-inorganic hybrids as light-absorbers for planer and nanorod-based perovskite solar cells. *Sol. Energy Mater. Sol. Cells* **2017**, *162*, 93 – 102.

[40] Tanaka, K.; Takahashi, T.; Kondo, T.; Umebayashi, T.; Asai, K.; Ema, K. Image charge effect on two-dimensional excitons in an inorganic-organic quantum-well crystal. *Phys. Rev. B* **2005**, *71*, 045312.

[41] Ishihara, T.; Hong, X.; Ding, J.; Nurmikko, A. Dielectric confinement effect for exciton and biexciton states in PbI4-based two-dimensional semiconductor structures. *Surf. Sci.* **1992**, *267*, 323 – 326.

[42] Cao, D. H.; Stoumpos, C. C.; Farha, O. K.; Hupp, J. T.; Kanatzidis, M. G. 2D Homologous Perovskites as Light-Absorbing Materials for Solar Cell Applications. *J. Am. Chem. Soc.* **2015**, *137*, 7843–7850.

[43] Stoumpos, C. C.; Cao, D. H.; Clark, D. J.; Young, J.; Rondinelli, J. M.; Jang, J. I.; Hupp, J. T.; Kanatzidis, M. G. Ruddlesden–Popper Hybrid Lead Iodide Perovskite 2D Homologous Semiconductors. *Chem. Mater.* **2016**, *28*, 2852–2867.

[44] Du, K.-z.; Tu, Q.; Zhang, X.; Han, Q.; Liu, J.; Zauscher, S.; Mitzi, D. B. Two-Dimensional Lead(II) Halide-Based Hybrid Perovskites Templated by Acene Alkylamines: Crystal Structures, Optical Properties, and Piezoelectricity. *Inorg. Chem.* **2017**, *56*, 9291–9302.

[45] Cortecchia, D.; Neutzner, S.; Srimath Kandada, A. R.; Mosconi, E.; Meggiolaro, D.; De Angelis, F.; Soci, C.; Petrozza, A. Broadband Emission in Two-Dimensional Hybrid Perovskites: The Role of Structural Deformation. *J. Am. Chem. Soc.* **2017**, *139*, 39–42.

[46] Gelvez-Rueda, M. C.; Hutter, E. M.; Cao, D. H.; Renaud, N.; Stoumpos, C. C.; Hupp, J. T.; Savenije, T. J.; Kanatzidis, M. G.; Grozema, F. C. Interconversion between free charges and bound excitons in 2D hybrid lead halide perovskites. *J. Phys. Chem. C* **2017**, *121*, 26566–26574.

2

EFFECT OF THE MAGNITUDE AND DIRECTION OF THE DIPOLE OF THE ORGANIC CATION ON THE ELECTRONIC STRUCTURE OF HYBRID HALIDE PEROVSKITES

This chapter is about ab-initio calculations (DFT and SOC-G_0W_0) of the optoelectronic properties of different hybrid-halide perovskites, namely X-PbI_3 (X=methylamonimum, formamidinium, guanidinium, hydrazinium, hydroxylammonium). These calculations shed a new light on how the substitution of different organic cations in the material influences its optoelectronic properties. Our simulations show a significant modification of the lattice parameter and band gap of the material upon cation substitution. These modifications are not only due to steric effects but also due to electrostatic interactions between the organic and inorganic part of the material. In addition to this, we demonstrate how the relative orientations of neighboring cations in the material modifies the local electrostatic potential of the system and its fundamental band gap. This change in the band gap is accompanied by the formation of localized and spatially separated electronic states. These localized states modify the carrier mobility in the materials and can be a reason for the formation and recombination of the charge carriers in these very promising materials.

This chapter is based on S. Maheshwari, S. Patwardhan, G. C. Schatz, N. Renaud, and F. C. Grozema, *Phys. Chem. Chem. Phys.* **2019**, *21*, 16564-16572

2.1. INTRODUCTION

Hybrid halide perovskites are currently among the most studied new materials for application in photovoltaic cells. The main driver for this is the rapid increase in the device efficiency over the last decade, reaching values over 23%.[1–3] The high efficiencies that have been obtained can be traced back to some of the basic properties of hybrid perovskite materials, i.e. a high absorption coefficient, long carrier lifetimes and diffusion lengths, a relatively charge carrier mobility, and the possibility to tune the properties by modification in the composition of the materials. [4–10] An additional advantage of hybrid perovskites is that they potentially have a very low production cost.[11]

The general ABX_3 structure of hybrid halide perovskite (HHP), materials allows for substitution of the organic cation (A), inorganic cation (B) and halide anions (X). Hence a large number structural variations have been reported, each leading to different optoelectronic properties of the materials. Among all the structures, methylammonium lead iodide ($CH_3NH_3PbI_3$) perovskites have been studied the most as it was the first to be used as a light absorber in mesoscopic solar cells.[12] Several theoretical studies have shown that the valence band of this material is mainly composed of *p*-orbitals of iodides whereas the conduction band consists primarily of *s*-orbitals of lead.[13]

Recently the static and dynamic effects related to the organic cation have emerged as a new avenue to understand and control the properties of HHPs. It has been shown for example that if the methylammonium cation is replaced by a slightly larger formamidinium cation the band gap is reduced by 0.05 eV, whereas when replaced by a smaller cesium ion, it increases by 0.16 eV.[14–16] Such modifications of the electronic structure stem from two main effects: steric hindrance for large organic cations that deform the lead-iodide lattice[17] and electrostatic effects for cations presenting a significant dipole moment. In addition, NMR and neutron diffraction studies have shown that these cations are to some extent free to rotate in the lead-iodide cage.[18] This dynamic behavior can also lead to significant modifications of the dielectric constant, rate of charge recombination and exciton binding energy of the material.[19]

We have demonstrated the role of the methylammonium cation dynamics in determining the mobility and lifetime of charge carriers.[20] Based on pulse-radiolysis microwave conductivity measurement we have shown that mobility and lifetime of charge carriers are significantly affected by the dynamic disorder in the $CH_3NH_3PbI_3$ perovskite. The transition to orthorhombic phase leads to an increase in the mobility and the half-lifetime of the charge carriers. This is attributed to the fact that in orthorhombic phase, the motion of the MA cation ceases thus expelling the dynamic disorder from the system. The free rotation of the cations also leads to a pronounced ferroelectric response of the material to an external field. [21, 22] This ferroelectric effect leads to the polarization of the whole lattice and promotes charge separation.[23] The similar orientation of the dipoles in these domains leads to local variations in the band gap.[23] Theoretical calculations have also shown that a random orientation of the dipoles can significantly localize the valence and conduction bands of the material. [24]

Cation	Structure	Dipole Moment
GA	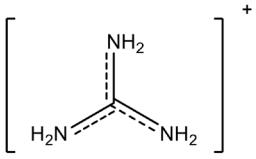	0
FM	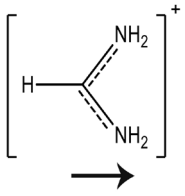	0.25
MA	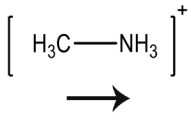	2.15
HZ	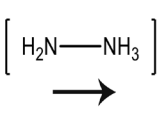	2.88
HA	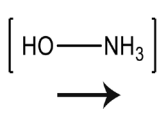	3.12

Table 2.1: The structures of the organic cations with the direction of their dipole moment. The dipole moment are reported in Debye.

In this chapter, we investigate the structure-property relationship of hybrid halide perovskites with a special emphasis on the role played by dipole moment of the organic cations. To understand the steric and electrostatic impact of the cation on the electronic properties of the material, we have chosen five organic cations with different size and dipole moment as shown in Table 2.1. We shown that, depending on the mutual orientation of the dipolar organic cations, localized states can be formed where electrons and holes are located in different parts of the material. This is expected to result in long carrier lifetimes, particularly at low temperatures where the organic cations are frozen in a fixed orientation.

2.2. METHODS

For the calculation of dipole moment, an augmented correlation consistent polarized valence (aug-cc-pVTZ) basis set was chosen along with BLYP functional combining the Becke exchange functional and LYP correlational functional in Gaussian 09.[25] Optimization of the different X-PbI_3 structures (where X=methylamonimum, formamidinium, guanidinium, hydrazinium, hydroxylammonium) were performed using projector augmented wave (PAW) pseudopotentials with the Van der Waals corrected PBE exchange-correlation functional as implemented in VASP 5.4.1.[26–30] An energy cut off of 500 eV and a gamma-centered Brillouin zone sampling grid of 8 X 8 X 8 were chosen for these calculations. The ionic positions were relaxed while conserving the lattice shape for continuous values of the lattice parameter. Band structure of the different X-PbI_3 materials were then computed at DFT level of theory at a denser mesh containing 600 k-points. The band gap was again computed at the SOC-G_0W_0 level of theory including local field effects.[26, 27, 29, 30] The electrostatic potential of the system was obtained using VASP with ionic and Hartree potential. Atomic charges on the atoms were obtained using Baders population analysis after DFT calculation.[31] The total energy of point charge system was computed with GULP, using Ewald summation to account for periodic boundary conditions.[32]

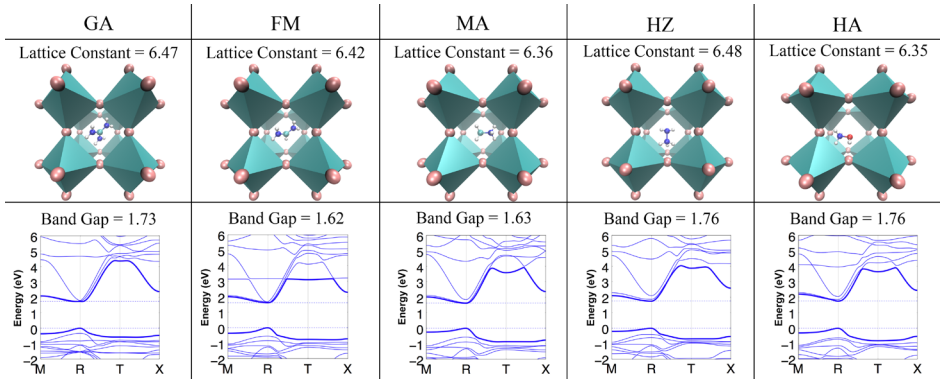

Figure 2.1: Band structure and optimized geometry of the X-PbI_3 system with X as the organic cation. The value of lattice constant is in Angström and value of band gap is in eV. The k-points in brillouin zone are M : $[\frac{1}{2},\frac{1}{2},0]$, R:$[\frac{1}{2},\frac{1}{2},\frac{1}{2}]$, T: $[0,0,0]$, X: $[0,\frac{1}{2},0]$.

Table 2.2: Total energy, structural parameters and band gap value for the optimized geometry of X-PbI_3 perovskite. The experimental data [*] is taken from references Weller et al. [18], Yin et al. [33] The lattice constant and bond length are in Angström and energy is in eV.

In X-PbI_3, X =	**GA**	**FM**	**MA**	**HZ**	**HA**
Lattice Constant	6.47	6.42 [6.36*]	6.36 [6.33*]	6.48	6.35
Bond Angles$_{\angle Pb-I-Pb}$	169	168	172	172	166
	169	174	169	167	168
	169	175	169	166	167
Average Angle$_{\angle Pb-I-Pb}$	169	173	170	168	167
Band Gap (DFT)	1.73	1.62	1.63	1.76	1.76
Band Gap (SOC-G_0W_0)	1.68	1.50 [1.47*]	1.55 [1.53*]	1.84	1.79

2.3. RESULTS AND DISCUSSION

2.3.1. EFFECT OF CATION SUBSTITUTION ON LATTICE SIZE AND BAND GAP

The geometry of the different X-PbI_3 (where X=GA, FM, MA, HZ, HA) structures was optimized to gain insight in the effect of cation substitution on the size of the unit-cell. The optimized value of the lattice constant and the corresponding optimized geometry are reported in Figure 2.1. The structural parameters of the optimized geometry and the electronic band gap are reported in Table 2.2. As seen in this table, the lattice constant computed at DFT-D3 level of theory for MA and FM are in good agreement with the experimental data. It is also seen that the lattice constant varies non-linearly with the size of the cation suggesting that there are more interactions that play a role than just the steric repulsion between the cation and lead-iodide framework. For example, despite being the smallest cation, HZ leads to a larger lattice constant than other cations. However as seen in Fig. 2.1, HZ has a large dipole moment. GA being the biggest in size among the five cations assumes unit-cell that is slightly smaller than HZ. This illustrates how both electrostatic effects and specific interactions, together steric effects, significantly influence the atomistic structure of these materials. Apart from affecting the size of unit cell, these interactions also have a significant impact on the Pb-I-Pb angles as seen in Table 2.2. The stronger are the steric and electrostatic interactions between organic cation and the Pb-I lattice, the larger the change in Pb-I-Pb angles from 180°. As seen in the Table 2.2 the average of the Pb-I-Pb angles deviates from the ideal 180° angle in the order FM < MA < GA < HZ < HA .

The optimized geometries obtained at the DFT-D3 level of theory, were used to compute the band structure of the materials. The resulting band structure and band gap are shown in Fig. 2.1 and Table 2.2. As seen in this figure, the values of the band gap obtained at the SOC G_0W_0 level of theory are in good agreement with the available experimental data. The values of the band gap show an increase in the order FM < MA < GA < HA ≈ HZ. This trend of increasing in band gaps coincides with the trend in the deviation of the Pb-I-Pb angle from the ideal 180°. Here the HZ cation shows an abnormally high band gap at the G_0W_0 level of theory, which is a result of larger lattice constant for the cation.

These calculations show that the Pb-I-Pb angles and the lattice constant of the system have a direct impact on the fundamental band gap of the material. The Pb-I-Pb angles are determined by the steric and electrostatic interactions in the system, and therefore indirectly affect the band gap of the system. This finding is consistent with the earlier reports of Filip et. al. [34]

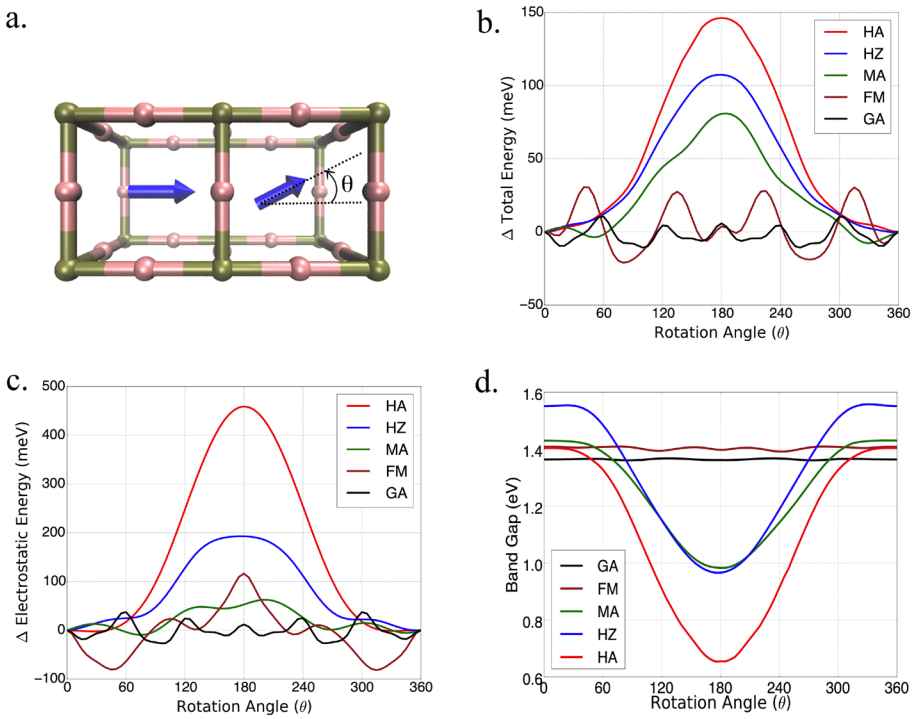

Figure 2.2: (a) Representation of the system considered to assess the impact of the dipole orientations. (b) The variation of total energy computed at the DFT level of theory. Energy of the system is normalized to one unit cell(c) Electrostatic energy variation computed point charge model (d) Band Gap variation with the rotation of the cation.

2.3.2. EFFECT OF DIPOLE ORIENTATIONS

To understand how disorder in the orientation of the dipolar organic cations affects the electronic properties of the perovskites we have studied variations in the electronic structure induced by the rotation of a dipole in extended systems. To achieve this, we have considered two neighboring unit cells as shown in Fig. 2.2. As seen in this figure, the orientation of one cation was kept fixed while continuously rotating the cation located in the neighboring unit cell. Throughout the calculations, the lead-iodide framework was kept fixed in a perfectly cubic arrangement to address only the effect of dipole rotation without any influence of lattice deformation. The values of the total energy obtained for the different cation arrangement are reported in Fig. 2.2B. As seen in this figure, a

considerable variation in the total energy of the system was observed upon rotation of the cations with high dipole moment, i.e. MA, HZ, and HA. For these cations a maximum energy ranging from 80meV to 150meV was obtained for anti-parallel orientations of the neighboring dipoles. These values are in good agreement with the ones reported by Quarti et. al.[35] It is also observed that the variation of the total energy for low dipole moment cations was much smaller, as expected.

To clarify whether repulsive dipole-dipole interactions are responsible for the trend in the total energy obtained from the DFT calculation we have separate calculated the electrostatic interactions in the systems using a point charge model. The variation of electrostatic energy per unit cell with the rotation of dipoles is shown in Fig. 2.2C. As seen in this figure, these variations follow the same trend as obtained from the DFT calculations, with a maxima in the anti-parallel configuration. This confirms the crucial role of electrostatic interaction in determining the cation arrangement in HHPs materials. The relatively low energy barriers for dipole rotation suggest that anti-parallel configurations of dipoles may exist even at room temperature, albeit in small concentrations.

Figure 2.2d shows the variations of the band gap upon rotation of the cations. As seen in this figure, a considerable reduction of the band gap was obtained for anti-parallel configurations of high dipole moment cations. The relative change in the band gap from a parallel to an anti-parallel configuration is 31% for MA, 38% for HZ and 53% for HA. In. contrast, the low dipole moment cations show minimal variation of band gap with change of mutual orientation of the cations. These calculations clearly show that even-though organic cations do not participate directly in the valence and conduction band levels, their orientations can significantly affect the energy of these bands via electrostatic interactions.

The band structures for the parallel and anti-parallel orientations of $MAPbI_3$ in Figure 2.3a,c clearly show a dependence on the orientation of the MA cation. An anti-parallel orientation of cations decreases the distance between the valence and conduction bands and is accompanied by a change in the curvature of the bands. These change in the electronic structure can be related to changes in the electrostatic potential due to the organic cation on rotation. The electrostatic potential is uniformly distributed across the system consisting of two unit cells when both dipoles have the same direction, as shown in Figure 2.3b. However, when the dipoles are anti-parallel, the potential distribution becomes non uniform between the adjoining unit cells. This variation is shown by calculating the difference between the electrostatic potential of systems with anti-parallel and parallel orientations of cations, $V_{net} = V_{anti-parallel} - V_{parallel}$ and is shown in Figure 2.3d. It can be seen here that the potential is lower at the interface of the unit cells, where the positive ends dipoles point towards each other and is higher at the interface where the tails of the dipoles are closer. The difference between the total electrostatic potentials at the two spatial locations is 1.2 eV.

2.3.3. LOCALIZATION EFFECTS DUE TO DIPOLE ORIENTATIONS

To understand the impact of orientations of neighboring cations on the the electronic states in the disordered perovskites, we have considered a system composed of four unit

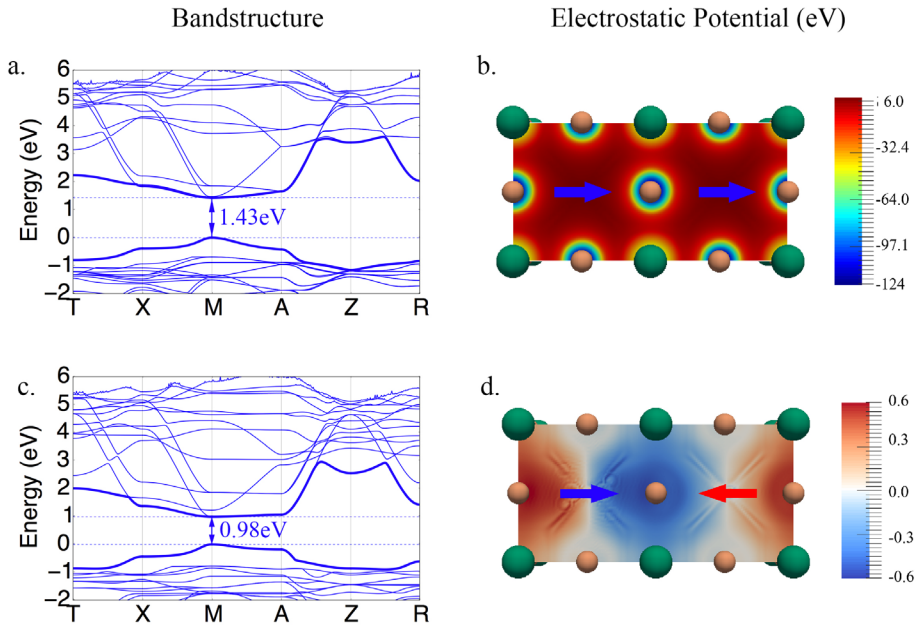

Figure 2.3: (a) Band structure for $MAPbI_3$ parallel orientation, (b) electrostatic potential distribution in this orientation of dipoles, (c) Band structure in anti-parallel orientation of dipoles and (d) difference of electrostatic potential of anti-parallel and parallel orientations, $V_{net} = V_{anti-parallel} - V_{parallel}$. The k-points in Brillouin zone are $T:[0,0,0], X:[0,0,\frac{1}{2}], M:[0,\frac{1}{2},\frac{1}{2}], A:[\frac{1}{2},\frac{1}{2},\frac{1}{2}], Z:[\frac{1}{2},0,0], R:[\frac{1}{2},0,\frac{1}{2}]$

cells as represented in Fig. 2.4 and 2.6. As seen in these figures, two different configurations of the organic cations were considered, one where the four cations are aligned in the same direction and the other where two neighboring cations are rotated by 180°, thus creating domains. The electronic structure of these systems was then studied for two different cations, i.e. MA (Fig. 2.4) and FM (Fig. 2.6). In each case, the band-decomposed charge density was extracted to visualize the electronic states corresponding to the valence band maximum and conduction band minimum.

As seen in Fig. 2.4a the electronic states of valence band maximum and conduction band minimum for $MAPbI_3$ are completely delocalized over the unit cell when all four dipoles are oriented in the same direction. The band gap of the system in this case is 1.43 eV. When the system with an anti-parallel orientation of dipoles is considered, the electronic states become localized at the interfaces between the newly created domains. The band gap in this configuration decreases to 0.41 eV, even lower than for the anti-parallel configuration of two unit cells in Figure 2.3. To understand the reason for this localization of states and the decrease of the band gap, the electrostatic potential was plotted again for the parallel and anti-parallel orientation of dipoles for the system consisting of four unit cells. As seen in Figure 2.5 the electrostatic potential stays uniformly distributed when all dipoles are in a parallel orientation, but becomes non-uniform for the anti-parallel orientation. It is important to note that the electrostatic potential in figures 2.3 and 2.4 were calculated for the full systems using the DFT electron density, and not just that of the dipolar cations. The anti-parallel orientation of the MA dipoles polarizes the electron distribution of the Pb-I framework, leading to an overall increase in electron density at the point where the dipoles are pointing towards each other. The difference in potential between the places of high and low relative potential increases from 1.2 eV to 2 eV when going from a system of two anti-parallel cations in a double unit cell to four anti-parallel cations in a quadruple unit cell. This shows that increasing the size of the organized domains leads to more pronounced electrostatic potentials at the interfaces between the domains. From the localization of the conduction band in the region where the MA dipoles point towards each other, it becomes clear that this is where an excess electron will be localized, while and excess positive charge will become localized at the negative end of the dipoles, as evident for the density for the valence band maximum, see Figure 2.4a. Thus we can conclude that the local electrostatic environment ihas a pronounced influence on the localization of the electronic bands in these materials, which results in a variation in the band gap. It should be noted that the number of unit cells that is at an interface between different aligned domains will be very small compared to those inside the larger domains. This means that in an experiments the band gap will be dominated by the states inside the domains that are characterized by a larger band gap.

To confirm the role played by electrostatic interactions in the localization of the electronic states we have performed the similar calculations with low dipole moment FM. The results presented in Fig. 2.6 show that the delocalization of the electronic state here is not affected by the rearrangement of the cations in this case. Furthermore, the band gap of the system is almost independent of the orientation of the cation. This clearly demonstrates that the rotation of cations with low dipole moment do not have a signif-

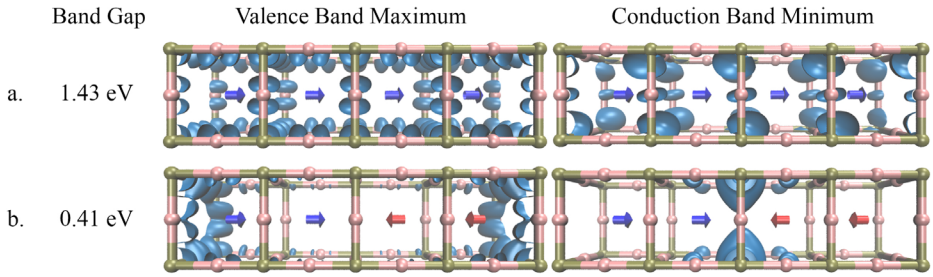

Figure 2.4: Band gap and distribution of electronic states of $MAPbI_3$ in case of (a) Parallel orientation of dipoles (b) Anti-parallel orientation of dipoles.

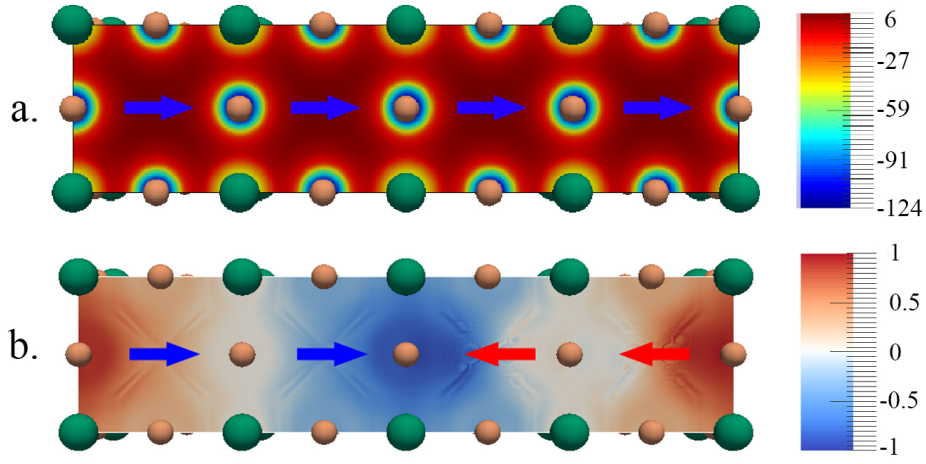

Figure 2.5: (a) Electrostatic potential distribution in case of parallel orientation of MA. (b) Electrostatic potential distribution in case of anti-parallel orientation of MA subtracted from the parallel orientation.

icant effect on the electronic structure of the material. Thus, only cations with significantly high dipole moment can alter the local electrostatic potential in the system and can significantly influence the electronic properties.

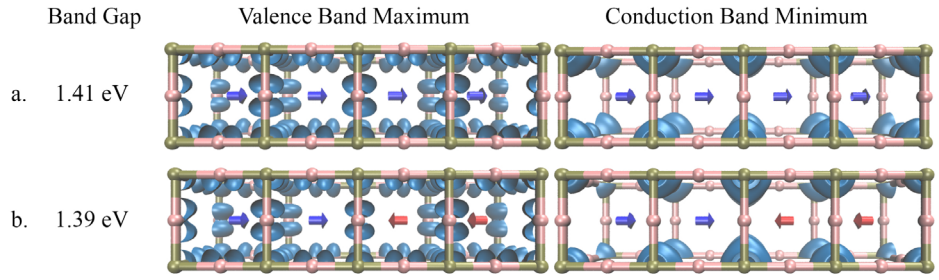

Figure 2.6: Band gap and distribution of electronic states of $FMPbI_3$ in case of (a) Parallel orientation of dipoles (b) Anti-parallel orientation of dipoles.

Table 2.3: The effective mass of electrons and holes for MA in bulk and in localized state in Figure 2.4b in three perpendicular directions. The direction X corresponds to the direction of dipoles and the directions Y and Z correspond to the two orthogonal directions. The effective masses are estimated from the respective band structures using band fitting method.

	Parallel dipoles	Anti-parallel dipoles		
	X, Y and Z	X	Y	Z
m^*_h	0.15	0.36	0.15	0.15
m^*_e	0.58	13.04	0.91	0.75

To gain insight in the effect of formation of localized electronic states on the effective mass of the charge carriers, we have calculated the effective mass in systems with uniform dipole directions and for the anti-parallel domains as reported in Table 5.2. For a uniform direction of dipoles the effective mass is the same in all directions and values of 0.1 m_0 and 0.58 m_0 are found for the hole and the electron, respectively. The effective masses for the system of four unit cells with anti-parallel dipoles were estimated by the band fitting method in the three orthogonal directions for the localized states, in which X corresponds to the direction of dipoles, Y and Z are two orthogonal directions. For the direction perpendicular to the orientation of the dipoles, effective mass values that are similar to those for the system without anti-parallel dipoles are obtained. This shows that similar charge mobilities can be expected in these direction. In the X-direction, corresponding to the direction of the dipoles, the effective masses are considerably larger. This shows that transport from one localized domain to the other is relatively inefficient and hence the charges will remain separated in their respective domains. This may results in slower recombination of electrons and holes in this material if the dipole orientations are static, as was found experimentally at low temperatures where the dipolar dynamics are frozen.

Different arrangements of cations of $MAPbI_3$ were considered to understand the conditions required for the formation of such localized states. A few of these conformations are shown in Fig. 2.7. Configuration a, where all the dipoles have the same orientation, is the most energetically favorable conformation. The introduction of disorder in the cation orientation without the creation of clear domains, such as in conformation b and c does not significantly change the band gap, nor does it lead to the formation of localized states. Only the creation of well-defined boundaries between domains, as in conformation d induce the formation of localized states at the domain walls. Note that the formation energy of such conformation is only 80 meV above the energy of conformation a. This energy difference suggests that the formation of such local domains can take place at room temperature.

2.4. CONCLUSIONS

The calculations presented in this chapter show that the substitution of cations with varying size and dipole moment in the lead iodide framework has a pronounced effect on the electronic structure of the material by modulating the bond angles Pb-I-Pb. The relative orientation of dipoles also significantly affects the electronic structure and band gap of the hybrid halide perovskites. The larger, the dipole moment of the organic cation, the larger its effect on the electronic structure. A larger dipole moment also leads to a larger energy barrier for the rotation of the dipoles. In case of MA, the barrier is 80 meV, indicating that at room temperature the anti-parallel configuration of dipoles can be accessed in small concentrations. Despite small concentrations of this configuration, significant effects on local electrostatic environment and the local electronic properties can be observed. The band gap of the system decrease upon the rotation of high dipole moment cations in anti-parallel orientation. This decrease is attributed to the change in the local electrostatic environment of the system. The anti-parallel orientation of dipoles results in formation of localized electronic states of valence and conduction bands. The valence band becomes localized in the region of higher electrostatic potential whereas the conduction band gets localized in the region of low electrostatic potential. This localization leads to a decrease in band gap of the system. The creation of these local domains also influences the effective masses of charge carriers as electrons and holes become heavier in the direction dipolar axis.

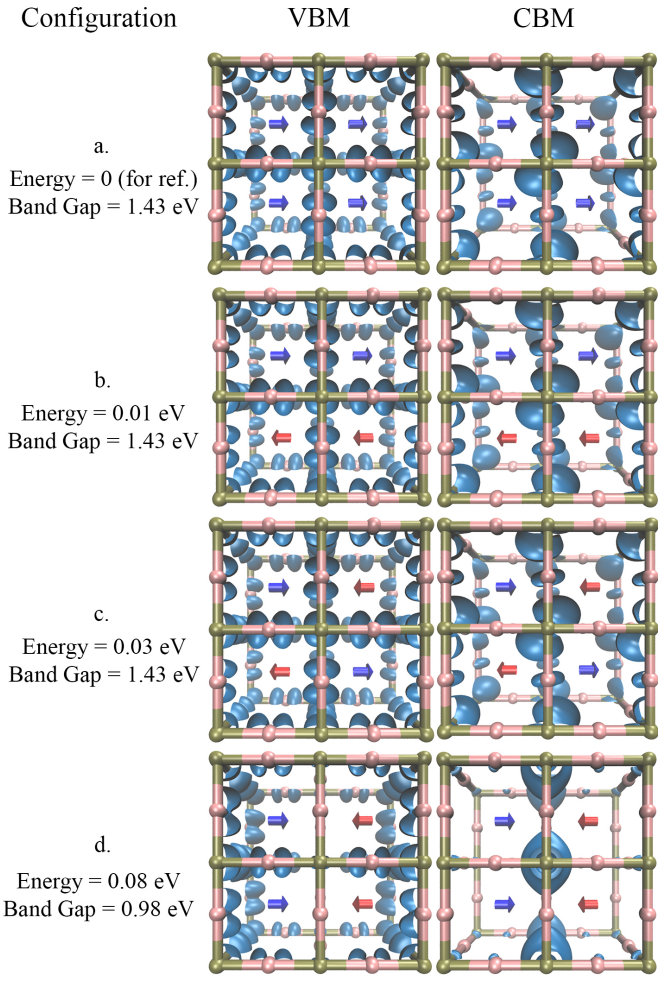

Figure 2.7: Distribution of electronic states of $MAPbI_3$ in four configurations for valence band maximum (VBM) and conduction band minimum (CBM). The total energy is normalized to one unit cell. High variation in energy and band gap is observed only in configuration d. The charge density is delocalized in configurations a, b and c but is localized in configuration d.

REFERENCES

[1] Brauer, J. C.; Lee, Y. H.; Nazeeruddin, M. K.; Banerji, N. Charge Transfer Dynamics from Organometal Halide Perovskite to Polymeric Hole Transport Materials in Hybrid Solar Cells. *J. Phys. Chem. Lett.* **2015**, *6*, 3675–3681.

[2] NREL Best Research Cell Efficiency, howpublished = https://www.nrel.gov/pv/assets/images/efficiency-chart.png, note = Accessed: 2018-05-14.

[3] Shin, S. S.; Yeom, E. J.; Yang, W. S.; Hur, S.; Kim, M. G.; Im, J.; Seo, J.; Noh, J. H.; Seok, S. I. Colloidally prepared La-doped BaSnO3 electrodes for efficient, photostable perovskite solar cells. *Science* **2017**, *356*, 167–171.

[4] Noh, J. H.; Im, S. H.; Heo, J. H.; Mandal, T. N.; Seok, S. I. Chemical management for colorful, efficient, and stable inorganic-organic hybrid nanostructured solar cells. *Nano Lett.* **2013**, *13*, 1764–1769.

[5] Sun, S.; Salim, T.; Mathews, N.; Duchamp, M.; Boothroyd, C.; Xing, G.; Sum, T. C.; Lam, Y. M. The origin of high efficiency in low-temperature solution-processable bilayer organometal halide hybrid solar cells. *Energy & Environ. Sci.* **2014**, *7*, 399.

[6] Xing, G.; Mathews, N.; Sun, S.; Lim, S. S.; Lam, Y. M.; Grätzel, M.; Mhaisalkar, S.; Sum, T. C. Long-Range Balanced Electron- and Hole-Transport Lengths in Organic-Inorganic CH3NH3PbI3. *Science* **2013**, *342*, 344–347.

[7] Stranks, S. D.; Eperon, G. E.; Grancini, G.; Menelaou, C.; Alcocer, M. J. P.; Leijtens, T.; Herz, L. M.; Petrozza, A.; Snaith, H. J. Electron-Hole Diffusion Lengths Exceeding 1 Micrometer in an Organometal Trihalide Perovskite Absorber. *Science* **2013**, *342*, 341–344.

[8] Quarti, C.; Mosconi, E.; Ball, J. M.; D'Innocenzo, V.; Tao, C.; Pathak, S.; Snaith, H. J.; Petrozza, A.; De Angelis, F. Structural and optical properties of methylammonium lead iodide across the tetragonal to cubic phase transition: implications for perovskite solar cells. *Energy Environ. Sci.* **2016**, *9*, 155–163.

[9] Eperon, G. E.; Stranks, S. D.; Menelaou, C.; Johnston, M. B.; Herz, L. M.; Snaith, H. J. Formamidinium lead trihalide: a broadly tunable perovskite for efficient planar heterojunction solar cells. *Energy Environ. Sci.* **2014**, *7*, 982–988.

[10] Eperon, G. E. et al. Perovskite-perovskite tandem photovoltaics with optimized band gaps. *Science* **2016**, *354*, 861–865.

[11] Snaith, H. J. Perovskites: The Emergence of a New Era for Low-Cost, High-Efficiency Solar Cells. *J. Phys. Chem. Lett.* **2013**, *4*, 3623–3630.

[12] Kojima, A.; Teshima, K.; Shirai, Y.; Miyasaka, T. Organometal Halide Perovskites as Visible-Light Sensitizers for Photovoltaic Cells. *J. Am. Chem. Soc.* **2009**, *131*, 6050–6051.

[13] Giorgi, G.; Fujisawa, J.-I.; Segawa, H.; Yamashita, K. Small Photocarrier Effective Masses Featuring Ambipolar Transport in Methylammonium Lead Iodide Perovskite: A Density Functional Analysis. *J. Phys. Chem. Lett.* **2013**, *4*, 4213–4216.

[14] Koh, T.; Fu, K.; Fang, Y.; Chen, S.; Sum, T.; Mathews, N.; Mhaisalkar, S.; Boix, P.; Baikie, T. Formamidinium-Containing Metal-Halide: An Alternative Material for Near-IR Absorption Perovskite Solar Cells. *J. Phys. Chem. C* **2014**, *118*, 16458–16462.

[15] Walsh, A. Principles of Chemical Bonding and Band Gap Engineering in Hybrid Organic–Inorganic Halide Perovskites. *J. Phys. Chem. C* **2015**, *119*, 5755–5760.

[16] Eperon, G. E.; Paternò, G. M.; Sutton, R. J.; Zampetti, A.; Haghighirad, A. A.; Cacialli, F.; Snaith, H. J. Inorganic caesium lead iodide perovskite solar cells. *J. Mater. Chem. A* **2015**, *3*, 19688–19695.

[17] Motta, C.; El-Mellouhi, F.; Kais, S.; Tabet, N.; Alharbi, F.; Sanvito, S. Revealing the role of organic cations in hybrid halide perovskite CH3NH3PbI3. *Nature Commun.* **2015**, *6*, 7026.

[18] Weller, M. T.; Weber, O. J.; Frost, J. M.; Walsh, A. Cubic Perovskite Structure of Black Formamidinium Lead Iodide, alpha-[HC(NH2)2]PbI3, at 298 K. *J. Phys. Chem. Lett.* **2015**, *6*, 3209–3212.

[19] Chen, T.; Foley, B. J.; Ipek, B.; Tyagi, M.; Copley, J. R. D.; Brown, C. M.; Choi, J. J.; Lee, S.-H. Rotational dynamics of organic cations in the CH3NH3PbI3 perovskite. *Phys. Chem. Chem. Phys.* **2015**, *17*, 31278–31286.

[20] Gélvez-Rueda, M. C.; Cao, D. H.; Patwardhan, S.; Renaud, N.; Stoumpos, C. C.; Schatz, G. C.; Hupp, J. T.; Farha, O. K.; Savenije, T. J.; Kanatzidis, M. G.; Grozema, F. C. Effect of Cation Rotation on Charge Dynamics in Hybrid Lead Halide Perovskites. *J. Phys. Chem. C* **2016**, *120*, 16577–16585.

[21] Stoumpos, C. C.; Malliakas, C. D.; Kanatzidis, M. G. Semiconducting Tin and Lead Iodide Perovskites with Organic Cations: Phase Transitions, High Mobilities, and Near-Infrared Photoluminescent Properties. *Inorg. Chem.* **2013**, *52*, 9019–9038.

[22] Kutes, Y.; Ye, L.; Zhou, Y.; Pang, S.; Huey, B. D.; Padture, N. P. Direct Observation of Ferroelectric Domains in Solution-Processed CH3NH3PbI3 Perovskite Thin Films. *J. Phys. Chem. Lett.* **2014**, *5*, 3335–3339.

[23] Leguy, A. M. A.; Frost, J. M.; McMahon, A. P.; Sakai, V. G.; Kochelmann, W.; Law, C.; Li, X.; Foglia, F.; Walsh, A.; O'Regan, B. C.; Nelson, J.; Cabral, J. T.; Barnes, P. R. F. The dynamics of methylammonium ions in hybrid organic-inorganic perovskite solar cells. *Nature Commun.* **2015**, *6*, 7124.

[24] Ma, J.; Wang, L. Nanoscale Charge Localization Induced by Random Orientations of Organic Molecules in Hybrid Perovskite CH3NH3PbI3. *Nano Lett* **2015**, *15*, 248–253.

[25] Frisch, M. J. et al. Gaussian09 Revision E.01. Gaussian Inc. Wallingford CT 2009.

[26] Blöchl, P. E. Projector augmented-wave method. *Phys. Rev. B* **1994**, *50*, 17953–17979.

[27] Kresse, G.; Joubert, D. From ultrasoft pseudopotentials to the projector augmented-wave method. *Phys. Rev. B* **1999**, *59*, 1758–1775.

[28] Grimme, S.; Antony, J.; Ehrlich, S.; Krieg, H. A consistent and accurate ab initio parametrization of density functional dispersion correction (DFT-D) for the 94 elements H-Pu. *J. Chem. Phys.* **2010**, *132*, 154104.

[29] Perdew, J. P.; Burke, K.; Ernzerhof, M. Generalized Gradient Approximation Made Simple. *Phys. Rev. Lett.* **1997**, *78*, 1396–1396.

[30] Perdew, J. P.; Burke, K.; Ernzerhof, M. Generalized Gradient Approximation Made Simple. *Phys. Rev. Lett.* **1996**, *77*, 3865–3868.

[31] Yu, M.; Trinkle, D. Accurate and efficient algorithm for Bader charge integration. *J. Chem. Phys.* **2011**, *134*, 064111.

[32] Gale, J. D. GULP: A computer program for the symmetry-adapted simulation of solids. *J. Chem. Soc., Faraday Trans.* **1997**, *93*, 629–637.

[33] Yin, W.-J.; Yang, J.-H.; Kang, J.; Yan, Y.; Wei, S.-H. Halide perovskite materials for solar cells: a theoretical review. *J. Mater. Chem. A* **2015**, *3*, 8926–8942.

[34] Filip, M. R.; Eperon, G. E.; Snaith, H. J.; Giustino, F. Steric engineering of metal-halide perovskites with tunable optical band gaps. *Nature Commun.* **2014**, *5*, 5757.

[35] Quarti, C.; Mosconi, E.; De Angelis, F. Interplay of orientational order and electronic structure in methylammonium lead iodide: Implications for solar cell operation. *Chem. Mater.* **2014**, *26*, 6557–6569.

3

THE RELATION BETWEEN ROTATIONAL DYNAMICS OF THE ORGANIC CATION AND PHASE TRANSITIONS IN HYBRID HALIDE PEROVSKITES

The rotational dynamics of organic cation in hybrid halide perovskites are intricately linked to the phase transitions that are known to occur in these materials, however, the exact relation is not clear. We have performed detailed model studies on methylammonium lead iodide and formamidinium lead iodide to unravel the relation between rotational dynamics and phase behavior. We show that the occurrence of the phase transitions is due to a subtle interplay between dipole-dipole interactions between the organic cations, specific (hydrogen bonding) interactions between the organic cation and the lead-iodide lattice, and deformation of the lead-iodide lattice in reaction to the reduced rotational motion of the organic cations. This combination of factors result in phase transitions at specific temperatures, leading to the formation of large organized domains of dipoles. The latter can have significant effects on the electronic structure of these materials.

This chapter is based on S. Maheshwari, M. B. Fridriksson, S. Seal, J. Meyer and F. C. Grozema, *J. Phys. Chem. C.* **2019**, *123*, 23, 14652-14661

3.1. INTRODUCTION

Hybrid halide perovskites are currently among the most studied emerging solar cell materials, with reported device efficiencies well over 20% within ten years after the first demonstration of a halide perovskite-based cell. [2–4] Hybrid halide perovskites consist of a general ABX_3 structure where B is a doubly charged metal ion such as lead or tin and X is a halide anion. A is a singly charged cation that, in the case of hybrid perovskites, is an organic ammonium compound such as methylammonium (MA) or formamidinium (FA). The metal and the halide ions together form an inorganic octahedral lattice with cages that are filled by the organic cations. The most common organic cation, methylammonium, has an asymmetric charge distribution resulting in a net dipole moment. At room temperature, the dipolar MA cation can rotate almost freely inside the metal-halide lattice. This leads to a high dielectric screening compared to halide perovskites with non-dipolar cations such as Cs^+.[5] It has also been proposed that the dipolar nature of MA plays an important role in the opto-electronic properties of hybrid halide perovskites, for instance through the formation of ferro-electric domains that promote formation of free charges on photo excitation or through polaronic effects that enhance the charge carrier lifetime.[6, 7] The rotational freedom of MA has been found to be highly dependent on temperature and specific phase transitions are known to occur. For instance, methylammonium lead iodide (MAPI) has a cubic structure at temperatures above 330 K, in which the MA can rotate freely. Between 170 K and 330 K a tetragonal phase is formed, in which the rotational motion is somewhat restricted. At temperatures below 170 K an orthorhombic phase is present where the rotational motion is fully absent.[8] In previous experimental work we have shown that the rotational freedom of the organic cation has a direct effect on the mobility and recombination kinetics of charges in MAPI.[9] Therefore, the rotational dynamics of organic cations in hybrid perovskites has received considerable attention, both experimentally and theoretically.[10–13] However, the relation to the phase behavior, and its effect on the opto-electronic properties of hybrid halide perovskites is not fully understood.

Most of the previous work has focussed on the rotation of the MA ion in MAPI as this is the most investigated of the hybrid perovskites in solar cells. Experimentally this includes solid-state NMR measurements,[14] single crystal x-ray measurements,[15] Raman spectroscopy[15] and quasielastic neutron scattering.[11] Theoretically, Monte Carlo simulations have been performed,[6, 16] as well as density functional theory studies[17, 18] and both *ab initio* molecular dynamics[19] and model potential molecular dynamics.[13] Most of these studies agree that at high temperatures the MA ion rotates freely without forming any ferroelectric or anti-ferroelectric domains, while below a certain phase transition temperature an orthorhombic phase is formed where the dipole rotation is frozen. The cause and effect relationship between the dipole dynamics and the phase transition is not fully understood. While most argue that the transfer to orthorhombic phase is the source of the restricted motion of the MA ions, some have suggested that the deformation of the lead iodide cage is caused by formation of ordered domains of dipoles at low temperatures.[17]

For formamidinium lead halide perovskites (FAPI) there is a lot less information. The

formamidinium (FA) cation is larger than MA, which may restrict its rotational motion by steric interactions. It also has an almost negligible dipole moment and it contains two nitrogen positions including hydrogens that can form hydrogen bonds with the lead iodide cage. FAPI exhibits a high temperature cubic perovskite structure [20] and a low temperature structure with octahedral tilting.[21] Carignano et al. have performed ab initio molecular dynamics simulations on FAPI and reported that at high temperatures there are preferential alignments of the FA ion due to hydrogen bonds with the cage.[22] They also concluded that FA rotates preferentially around the N - N axis, which has later been supported by other studies.[21, 22] Weber et al. reported that FA shows a certain ordering at low temperature where they align perpendicular with respect to their nearest neighbour do to the angle tilt of the cage.[23]

The time scale of the reorientation of the organic cation has been studied experimentally, for instance by neutron scattering experiments. For MAPI it was shown that the MA cation rotational dynamics is characterized by a timescale of 5 ps at room temperature and rocking or "wobbling" around the C3 axis that is much faster (≈1 ps).[6, 24] In a contradicting study, Leguy et. al. showed that the times scale for full reorientation of MA is 14 ps at room temperature.[6] Molecular dynamics simulations have also been performed to investigate the motion of the organic cation, either by ab initio dynamics or using classical force fields. From such simulations a reorientation time of approximately 7 ps has been obtained for both MA and FA.[19, 25, 26] For the FA cation in FAPI, neutron diffraction measurements have shown reorientation times of 4.7 ps and 2.8 ps for the long and short axis, respectively.[27]

In this chapter we have studied the relation between the reorientation dynamics of MA and FA in MAPI and FAPI and their phase transition behavior. Apart from just performing full molecular dynamics simulations, we have also performed a series of model calculations to clarify the role of specific interactions in the system. These model calculations include on-lattice Metropolis Monte Carlo simulations to study domain formation in a system with only dipole-dipole interactions and molecular dynamics simulations with a frozen cage. Together, these calculations give a new picture of the origin of the structural phase transitions in hybrid perovskites, which shows that they are caused by an interplay between dipole-dipole interactions, specific (hydrogen bonding) interaction between the organic cation and the inorganic cage and deformation of the metal halide cage.

3.2. METHODOLOGY

3.2.1. MOLECULAR DYNAMICS

The molecular dynamics (MD) simulations were performed on a super cell of 10x10x10 unit cells with periodic boundary conditions for MAPI and FAPI. The system size was chosen to access better statistics and independence of motion of dipoles in different parts of the system. Initial configuration was selected as cubic both for MAPI and FAPI with lattice constant of 6.21 Å for MAPI and 6.36 Å for FAPI as observed experimentally

at higher temperatures for both of these materials.[6, 28] The force field for the interatomic potentials was adopted from the work of Mattoni et. al.[13] The interactions in the force field are defined in form of three components i) inorganic-inorganic(U_{ii}), ii) inorganic-organic(U_{io}) and iii) organic-organic(U_{oo}) interactions. The U_{ii} and U_{io} are non-bonded interactions which are defined in terms of Buckingham and Lennard Jones parameters that take into account electrostatic and Van der Waals interactions respectively. U_{oo} interactions are defined as bonded interactions with parameters for bond stretching, angle bending and dihedral rotations for the organic cations. These parameters were obtained from the CHARMM forcefield using the SwissParam tool.[29–32] MD simulations were performed using the LAMMPS molecular dynamics simulation package.[33] The equations of motion were evaluated using time step of 1 fs and a cutoff of 17 Å for Lennard-Jones interactions and 18 Å for the Coulombic interactions. Simulations were performed in a sequence of three steps in which first step was annealing of system with an initial configuration of ordered orientations of MA/FA molecules. The annealing was performed from a higher temperature to the temperature required for the system over 3 nanoseconds. The second step was the equilibration of the system at the required temperature until the energy of system comes to an equilibrium. The third step was the production run from which a trajectory file covering 100 ps was obtained. The rotational dynamics of the organic cations in MAPI and FAPI was analyzed by examining the rotation-autocorrelation function, *C(t)* as defined in Equation 4.1 in terms of the dipole vectors μ_i of the MA and FA cations. For MA this vector coincides with the C-N axis, while for FA it is along the C-H bond.

$$C(t) = \frac{1}{N}\sum_{i=1}^{N} \vec{\mu}_i(t) \cdot \vec{\mu}_i(0) \tag{3.1}$$

This autocorrelation function gives a measure of how fast the orientations of the organic cations change with time. By definition, $C(t=0) = 1$ and decays to zero on average once the direction of the dipole has become completely random.

3.2.2. MONTE CARLO

The Metropolis Monte Carlo (MC) simulations were performed on a system consisting of 20x20x20 dipoles on a fixed grid with periodic boundary conditions. A cubic structure is assumed for all temperatures with a lattice constant of 6.29 Å. The only energy considered in the simulation is the (electrostatic) dipole-dipole interaction given by Equation 3.2. In this equation, p_i and p_j are the dipole moment vectors for both dipoles considered, r is the distance between the dipoles and $\hat{n}$ is a unitary directional vector between the two dipoles. Permittivity of vacuum is assumed. Only interactions between dipoles that are within three lattice distances of one another are considered. This is a reasonable assumption since the interaction energy is inversely proportional to the third power of the distance. The simulations were performed for both MA and FA dipoles at temperatures ranging from 100 K to 350 K with a 10 K interval.

$$E_{dd} = \frac{1}{4\pi\epsilon_0}\left(\frac{p_i \cdot p_j}{r^3} - \frac{3(\hat{n}\cdot p_i)(\hat{n}\cdot p_j)}{r^3}\right) \tag{3.2}$$

3.2.3. DOMAIN DETECTION

The domain detection aims to quantify how ordered or disordered the organic cations are at various temperatures in the MC and MD simulations based on dipole-dipole interaction. It does so by ordering all the dipoles in a simulation snapshot on a fixed grid and choosing a random dipole in the system. This dipole is the first dipole in the first domain. Next we evaluate which, if any of the six closest neighbors of the dipole belong in the same domain. This is done by comparing the orientations of those dipoles with the orientations that would minimize the dipole-dipole interaction energy between each of them and our first dipole. If their orientation is close enough to this minimum energy alignment they are added to the domain. The domain is then allowed to grow by evaluating the neighbors of the dipoles that were added to the domain. When all appropriate dipoles have been added to the domain the process is repeated considering all the dipoles in the system that have not been assigned to a domain. Finally, when all the dipoles have been assigned to a domain the average domain size is calculated. A large average domain size will then represent a more ordered system than a small one.

3.3. RESULTS AND DISCUSSION

Molecular dynamics and Monte Carlo simulations were performed both for MAPI and FAPI and we have subdivided the discussion in two parts. First we discuss the dipole dynamics and phase transitions in MAPI, after which we turn to FAPI. The results in both materials are compared and some general conclusions are presented after these sections.

3.3.1. METHYLAMMONIUM LEAD IODIDE (MAPI)

From the molecular dynamics simulation of MAPI, a trajectory of 100 ps is obtained after equilibration of the system. The rotation-autocorrelation function over these 100 ps, averaged over the 1000 MA dipoles in the system is shown in Figure 3.1a for temperatures between 100 K and 350 K. The rotation-autocorrelation plots show the randomization of the direction of the dipole moments with time.

At lower temperatures (100-250 K) the autocorrelation plots show a different trend than those at higher temperature. After an initial rapid decay, an almost constant value is obtained, indicating that no full randomization of the dipole direction occurs on the timescale of the simulations. The rapid initial decay corresponds to a wobbling-like motion where the dipolar molecule can move around in a cone but does not have enough rotational freedom for complete reorientation. The more pronounced initial decay at 150 K and 200 K, as compared to that at 100 K indicates that the cone in which movement takes place widens with temperature. In order to quantify the timescale of dipole relaxation times, the autocorrelation curves were fitted with a bi-exponential function given in Equation 3.3. A_1 and A_2 are the amplitudes of the two decay components characterized by the decay times τ_1 and τ_2. The two time constants can relate to different processes, *e.g.* the in-place wobbling motion and the full reorientation mentioned in the introduction. The parameters from fitting Equation 3.3 are summarized in Table 3.1.

$$y = A_1 \cdot e^{-t/\tau_1} + A_2 \cdot e^{-t/\tau_2} \tag{3.3}$$

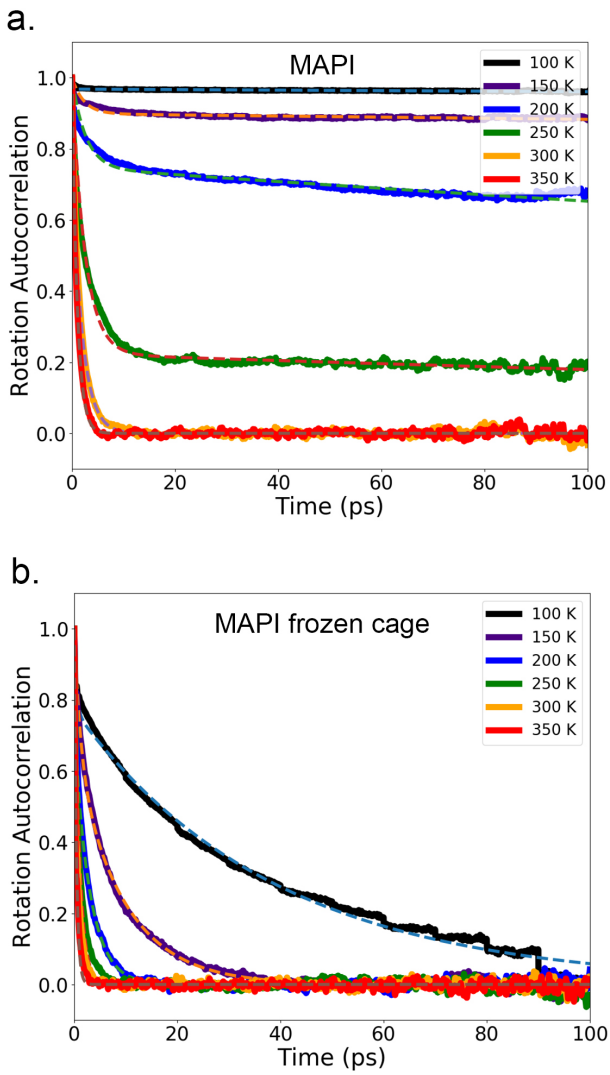

Figure 3.1: (a) Rotation-autocorrelation of the dipole direction averaged over 1000 dipoles for MA cations in a flexible lead iodide cage. (b) Rotation-autocorrelation of the dipole direction averaged over 1000 dipoles for MA cations in a frozen lead iodide cage

At temperatures of 250 K and lower, two very distinct timescales are found from the bi-exponential fit, a fast one that is typically in the order of 2.5 ps, and a very slow one that exceeds the time scale of the simulations. The fast initial decay corresponds to the in-place wobbling of the MA dipole, while the long-time decay corresponds to the full reorientation. The long-time decay constant of 450 ps and longer for these temperature indicate that the dipole orientation is virtually fixed on the time scale considered. Above 250 K the rotation-autocorrelation curves completely decay to zero within ≈ 5 ps. This indicates that at this temperature range, MA dipoles have full rotational freedom and behave almost liquid-like. At these temperatures the decay of the autocorrelation can be described with a single exponential function with characteristic time constants of 0.5 - 2.0 ps. It is interesting to note, that at these temperatures, no distinction can be made between the wobbling motion and full reorientation. The observed changes in rotational dynamics with temperature agree with experimentally observed phase dynamics and with earlier molecular dynamics simulation.[14, 34, 35]

Table 3.1: Rotation-autocorrelation decay time constants in picoseconds obtained after fitting the decay curves in Figure 3.1 using Equation 3.3. τ_1 corresponds to the faster decay time whereas τ_2 corresponds to the slower decay time constant.

	Flexible cage		**Frozen cage**	
T (K)	$\boldsymbol{\tau_1}$ **(ps) (A$_1$)**	$\boldsymbol{\tau_2}$ **(ps) (A$_2$)**	$\boldsymbol{\tau_1}$ **(ps) (A$_1$)**	$\boldsymbol{\tau_2}$ **(ps) (A$_2$)**
100	0.12 (0.03)	> 1000 (0.97)	0.42 (0.23)	38.75 (0.77)
150	2.26 (0.10)	> 1000 (0.90)	1.23 (0.35)	9.54 (0.65)
200	2.62 (0.25)	739.27 (0.75)	0.27 (0.30)	3.10 (0.70)
250	2.52 (0.78)	455.57 (0.22)	1.03 (1.00)	-
300	0.46 (0.25)	2.00 (0.75)	0.63 (1.00)	-
350	1.01 (1.00)	-	0.43 (1.00)	-

While the molecular dynamics simulations successfully describe the phase behavior in MAPI, at least qualitatively, the details of the relation between the dynamics of the MA cations and the phase transition is not fully clear. We have identified three possible effects that can play a role in this. The first is the deformation of the Pb-I cages. The reduced rotation of MA at low temperatures can either be caused by the deformation of the cages, or the reduced dipole rotation causes the deformation itself. The second effect is the interaction between the different MA cations in the system, which can lead to ordered domains with restricted rotational dynamics at low temperature. Finally, the third effect is related to specific interactions between the MA cation and the Pb-I cage structure, for instance hydrogen bonds between the ammonium and iodide ions. In order to clarify the importance of these three effects, we have performed a series of model simulations that are outlined below.

EFFECT OF CAGE DEFORMATION

In order to establish the importance of the deformation of the Pb-I framework on the rotational dynamics of the MA ions we have performed model calculations in which the

positions of Pb and I are frozen in the initial cubic conformation. In this way we can obtain insight in the motion of the organic cations in presence of specific interactions with the Pb-I cage and interactions with different organic cations, but in absence of deformation of the cage. As evident from Figure 3.1b and Table 3.1, the rotation-autocorrelation function decreases faster than for a flexible cage. The decay time of the autocorrelation function decreases uniformly as the temperature is increased from 100 K to 350 K. No sudden change is observed in the rotation time at 200 K for the frozen cage. This shows that the rotational motion of the organic cation is highly influenced by deformation of the Pb-I framework, especially at low temperatures.

EFFECT OF DIPOLE-DIPOLE INTERACTIONS

The second specific interaction we look at is dipole-dipole interactions between the MA ions. To investigate to what extent these interactions affect the alignment of MA, we have performed MC simulations at various temperatures. In these simulations only the dipole-dipole interaction energy is taken into account. Therefore, any formation of organized domains observed is solely due to these electrostatic interactions between MA ions, and not because of cage deformation or, for instance, hydrogen bonding with iodide. A convenient way to quantify the alignment of the MA dipolar ions with respect to each other is to look at snapshots of the simulations and divide all the ions into domains based on close range dipole-dipole interactions. A large domain then represents a certain long range ordering of dipoles. In Figure 3.2a the average domain size in the MC simulations is plotted versus the temperature. As these systems only depend on the dipole-dipole interaction energy, lowering the temperature, forces the dipoles to align more optimally with the other dipoles and especially their closest neighbors. This results in an exponential increase of average domain size as the temperature approaches 100 K, while at higher temperatures the systems is rather disordered as indicated by the smaller average domain size. This can be interpreted as a phase transition of sorts; at the temperature where $k_B T$ becomes comparable to the dipole-dipole interaction energy the ions align together due to their interactions with one another.

Figure 3.2b shows the same domain detection analysis on the MA ions in the MD simulations with a frozen cage. By comparing this to the simulations that only consider dipole-dipole interaction, we gain insight in the relative importance of the dipole-dipole interactions when specific interactions with the Pb-I cage are also taken into account. The frozen cage MD simulations show a similar trend in domain growth as the MC simulations. The increase in average domain size is however a lot smaller in this temperature range. This shows that with a surrounding cage, the MA ions are still affected by interaction with one another at low temperatures. However, the effect is less pronounced because specific interactions between the MA and the cage also play a role here.

To complete the comparison, we show the average size of domains of MA ions in the flexible cage MD simulations as a function of temperature in Figure 3.2c. These systems show a different behavior compared to the other two. First of all, the increase of the average domain size occurs at higher temperatures. Between 250 K and 200 K there is an

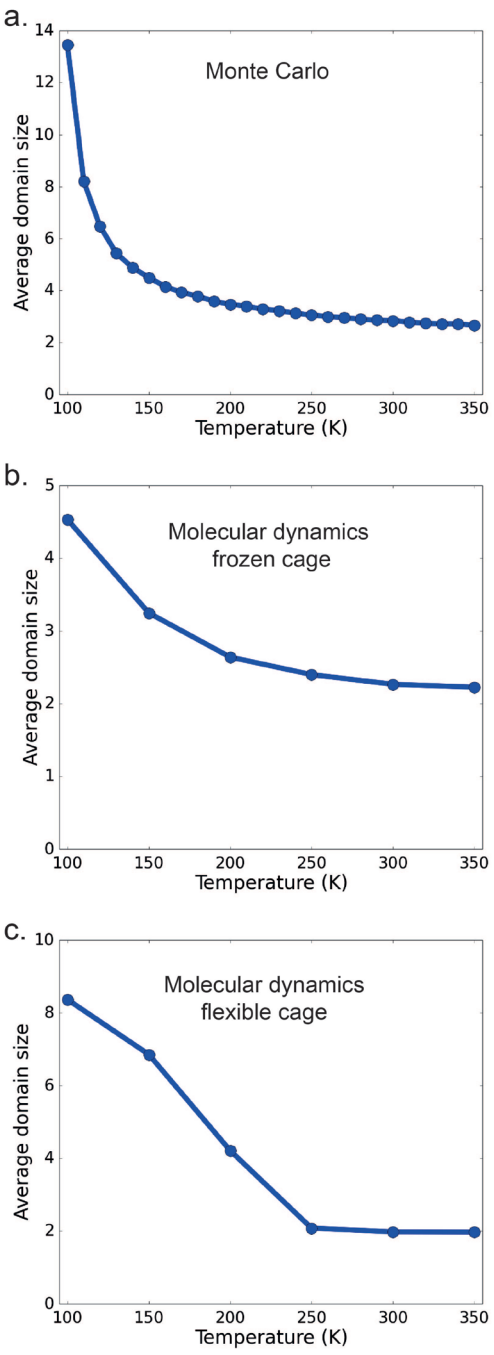

Figure 3.2: Average domain size (Number of dipoles) vs temperature (K) for methylammonium dipoles simulated with (a) Monte Carlo only considering dipole-dipole interaction, (b) molecular dynamics with frozen lead iodide cage, (c) molecular dynamics with flexible lead iodide cage

abrupt increase in the average domain size whereas, for the other systems notable increase was not seen until at roughly 150 K. Furthermore the nature of the increase is different compared to the MC system. In the case of the flexible MD simulations we do not observe a gradual exponential increase but instead an abrupt linear increase that seems to start saturating at the lowest simulated temperature. These differences are comparable to the difference we saw between rotation-autocorrelation plots for the flexible- and frozen-cage MD simulations. In the autocorrelation decays, an abrupt step was seen between 200 K and 250 K for flexible Pb-I cages, resulting in less reorientation of the methylammonium ions at the lower temperature. This was not seen in the case of the frozen cage.

EFFECT OF SPECIFIC INTERACTIONS BETWEEN MA AND CAGE

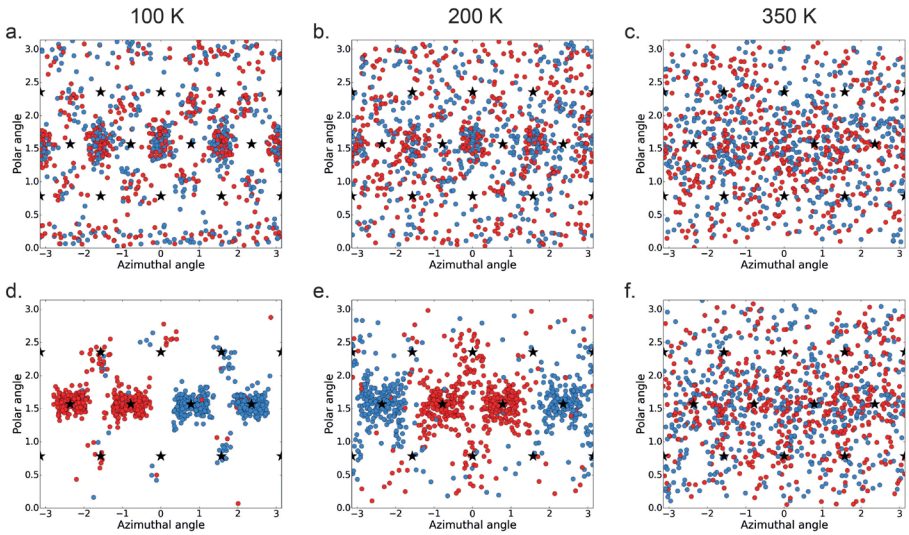

Figure 3.3: Orientations of all methylammonium dipoles in a single molecular dynamics system given in their polar and azimuthal angle. (a-c) frozen cage at 100 K, 200 K and 350 K and (d-f) flexible cage at 100 K, 200 K and 350 K.

Having investigated the effect of cage movement and dipole-dipole interaction, the final step is to understand the role of specific interactions between the lead-iodide cage and MA ion. To achieve this we have analyzed the MD simulations above in more detail, paying specific attention to the directions of the MA ions in a single system with respect to the lead iodide cage. This is done by plotting scatter plots with all MA directions obtained from a single simulation snapshot. Each point is then the direction of a single ion represented in its azimuthal and polar angles. We do this to observe whether certain ion directions within the cage become more prominent than others as the temperature is changed. Two different colors are used for the points to evaluate whether there is a difference between the neighboring layers in the system. Odd number layers are portrayed by blue points and even number layers are indicated in red. In these figures, the

stars represent the directions that correspond to an MA ion pointing directly towards an iodine molecule in a cubic cage. These plots are shown in Figure 3.3 for both MD simulations with flexible and frozen cage at 100 K, 200 K and 350 K. Similar figures were made for the other simulated temperatures and for the dipole-dipole MC simulations, these figures can be found in the supporting information. For the MC simulations the alignments were completely random at all temperatures. This is not surprising as there is no cage to affect the orientation of the MA ions.

Figures 3.3a-c show the directional ordering for the frozen-cage MD simulations at 100 K, 200 K and 350 K. At 350 K the alignment of the ions is random over the spherical surface; the reason for higher density at central polar angles is that this is a spherical surface projected on a rectangular graph. As the temperature is lowered to 200 K a structure emerges, with some orientations becoming more prominent than others. At 100 K this is even stronger. Surprisingly, the most common orientations are not directed towards iodines, as one would expect if the MA forms hydrogen bonds with the iodine. Furthermore, no difference is seen between different layers in these simulations.

Figures 3.3d-f represent the flexible cage MD simulations at 100 K, 200 K and 350 K. Again the alignment is random at 350 K and a more organized structure is formed when the temperature is lowered. In this case, however, the effect is much more pronounced with the ions aligning all in the same plane at the lowest temperature, and each adjacent layer aligning anti-parallel to its neighbor. Within each layer there are two main orientations, both where one would assume a hydrogen bond is formed. This is in agreement with previous studies were this alignment is attributed to the low temperature orthorombic phase.[13]

In order to get some insight on the dynamics of the specific interaction we have analyzed the timescale on which the hydrogen bonds are broken. These hydrogen bond life times are shown in Figure 3.4b as a function of temperature. It is clear from this figure that the time that hydrogen bonds exist in MA is very short, except at 100 K where a lifetime over 10 ps is obtained. This is consistent with the large degree of rotational freedom discussed above, even if the general direction is frozen, the wobbling motion still allows a considerable freedom for the MA to move around.

3.3.2. FORMAMIDINIUM LEAD IODIDE (FAPI)

In a similar way as for MAPI, full molecular dynamics simulations were performed for FAPI. A trajectory of the FA cations is obtained over 100 ps after equilibration of the system. The rotation-autocorrelation function averaged over the 1000 FA dipoles is shown as a function of time in Figure 3.5a. The simulations were performed at temperatures starting from 100 K to 350 K in steps of 50 K. The trends observed for FAPI exhibit substantial differences compared to those presented above for MAPI. The decay of the autocorrelation function shows a more gradual variation with temperature, indicating that in the same temperature range no strong phase transitions are observed. At 300 K and 350 K the rotation time for FA is larger than for MA as can be seen in Table 3.2. This is in agreement with experimental results [21, 27, 36] and can, at least in part, be attributed

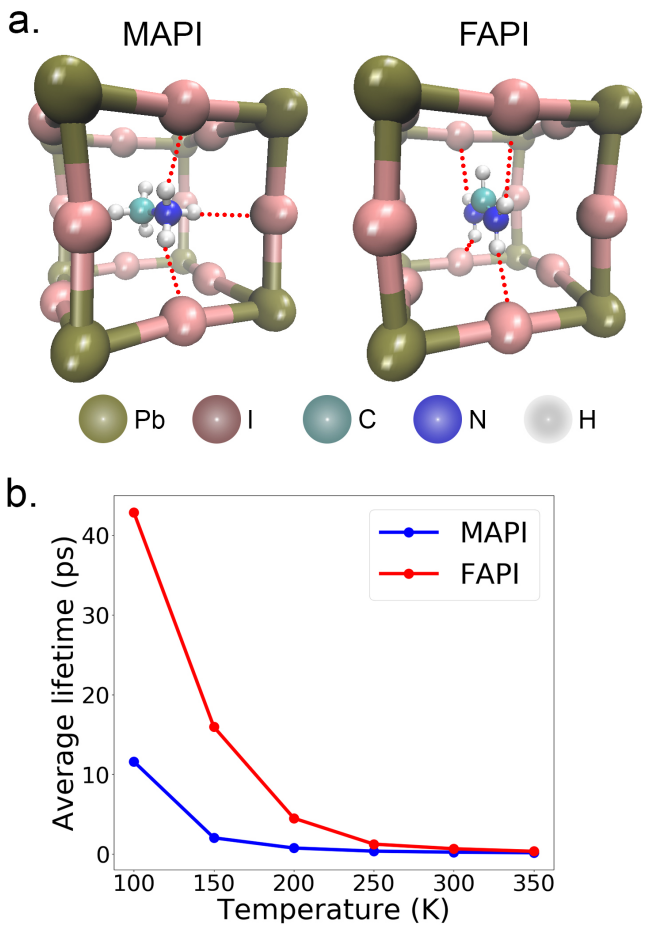

Figure 3.4: (a) The hydrogen bonds formed in MAPI and FAPI between the hydrogens of amine group and iodide atoms of the cage. (b) Hydrogen bond lifetime in picoseconds averaged for the hydrogen bonds formed for MAPI and FAPI.

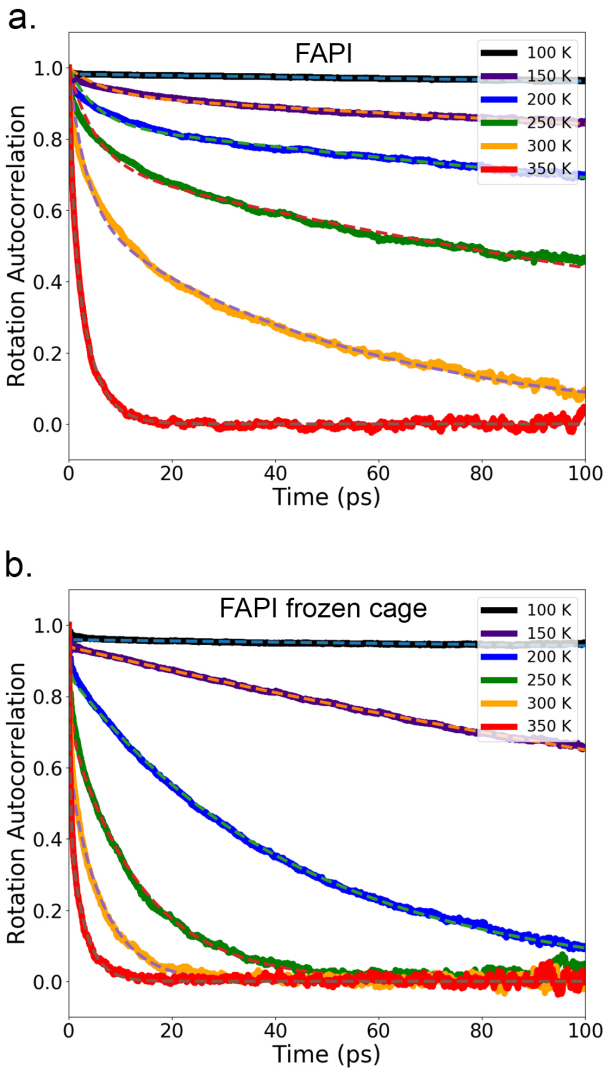

Figure 3.5: (a) Rotation-autocorrelation of the dipole direction averaged over 1000 dipoles for FA cations in a flexible lead iodide cage. (b) Rotation-autocorrelation of the dipole direction averaged over 1000 dipoles for FA cations in a frozen lead iodide cage

to the larger size of FA compared to MA. The other factor that influences these rotation times is the interactions of FA with the Pb-I cage in terms of hydrogen bonding. In order to unravel the different contributions to the observed rotational dynamics of FA in FAPI we have performed the same model calculations as for MAPI, as described below.

Table 3.2: Rotation-autocorrelation decay time constants in picoseconds obtained after fitting the decay curves in Figure 3.5 using Equation 3.3. τ_1 corresponds to the faster decay time whereas τ_2 corresponds to the slower decay time constant.

	Flexible cage		Frozen cage	
T (K)	τ_1 **(ps) (A$_1$)**	τ_2 **(ps) (A$_2$)**	τ_1 **(ps) (A$_1$)**	τ_2 **(ps) (A$_2$)**
100	0.05 (0.02)	> 1000 (0.98)	0.05 (0.04)	> 1000 (0.96)
150	7.14 (0.08)	> 1000 (0.92)	0.04 (0.06)	271.73 (0.94)
200	5.24 (0.16)	510.27 (0.84)	0.23 (0.14)	45.12 (0.86)
250	5.21 (0.27)	195.40 (0.73)	0.45 (0.28)	14.21 (0.72)
300	3.41 (0.40)	52.63 (0.60)	0.31 (0.41)	6.60 (0.59)
350	0.77 (0.34)	3.62 (0.66)	0.27 (0.54)	2.89 (0.46)

EFFECT OF CAGE DEFORMATION

The rotation-autocorrelation function for the motion of FA in a fixed Pb-I cage structure is shown as a function of time in Figure 3.5b. This figure and the rotation times in Table 3.2 show that also for the fixed cage, a gradual decrease in the rotation times is observed with increasing temperature. No abrupt changes due to phase transitions are formed. Comparison with Figure 3.5a shows that cage deformation leads to an overall slower dynamics, as was also the case for MAPI, however, the effect is not as pronounced as for MAPI. Nevertheless, these simulations show that the deformation of the Pb-I cage also plays a significant role in the rotation dynamics in FAPI.

EFFECT OF DIPOLE-DIPOLE INTERACTIONS

The effect of the dipole-dipole interactions on the FA alignment in FAPI was again evaluated by comparing the size of the ordered domains formed at various temperatures for the three different simulation types. That is, MC simulations considering only dipole-dipole interactions, molecular dynamics with a frozen Pb-I cages and fully flexible molecular dynamics simulations. The average domain size for these three cases is plotted as a function of temperature in Figure 3.6.

In the case of the MC simulations where only dipole-dipole interactions are considered the domain size is unaffected by the temperature in the considered temperature range, implying that the dipole-dipole interactions are not large enough to affect the ion alignments. This is due to the much smaller dipole moment of the FA ion compared to the MA ion. This results in dipole-dipole interactions that are much smaller than $k_B T$ at the temperatures considered, and hence the thermal energy is high enough to prevent

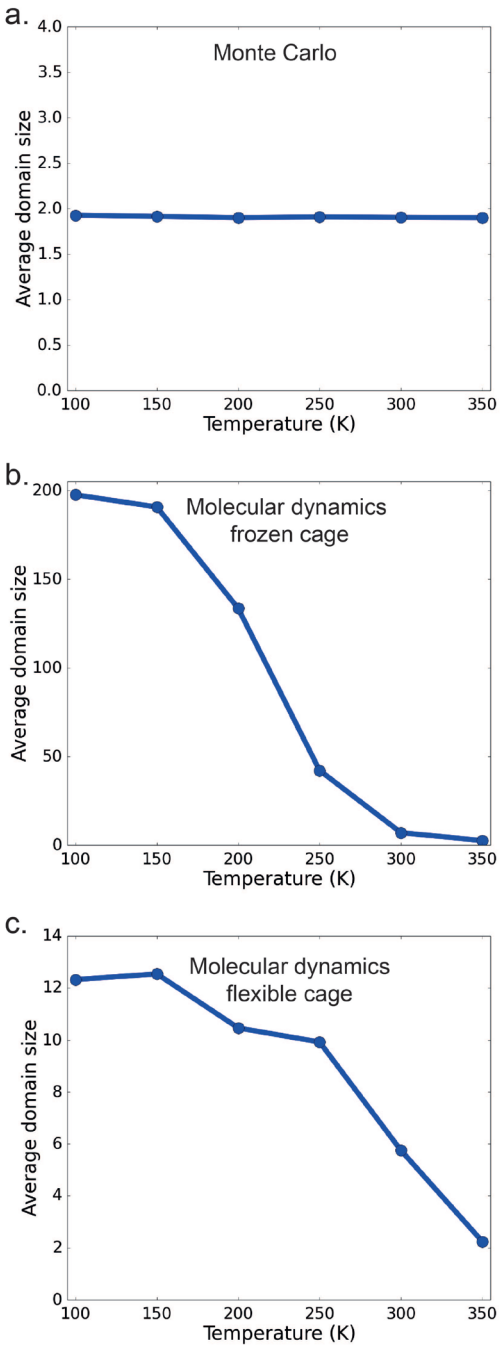

Figure 3.6: Average domain size (Number of dipoles) vs temperature (K) for formamidinium dipoles simulated with (a) Monte Carlo only considering dipole-dipole interaction, (b) molecular dynamics with frozen lead iodide cage, (c) molecular dynamics with flexible lead iodide cage.

the formation of domains. This implies that the phase transition in FAPI should not be affected by the dipole-dipole interaction of FA ions.

Interestingly, we observe an increase in domain size with lower temperatures for both molecular dynamics systems. This results in large domains at low temperatures, especially in the case of frozen cage. As we have excluded the possibility of a dipole-dipole effect it is likely that this happens due to some interaction between the ion and the cage that causes certain ion alignments to be more prominent than others.

EFFECT OF SPECIFIC INTERACTIONS BETWEEN FA AND CAGE

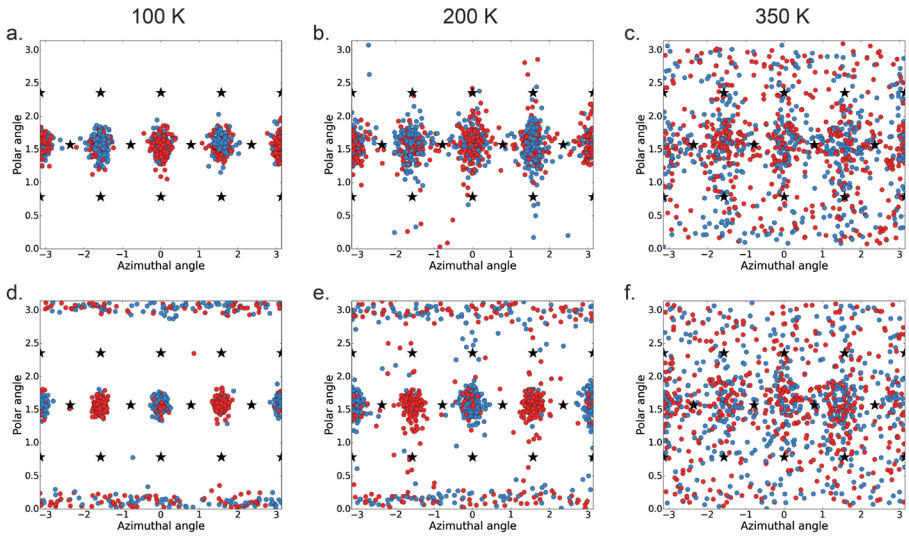

Figure 3.7: Orientations of all formamidinium dipoles in a single molecular dynamics system given in their polar and azimuthal angle. (a-c) frozen cage at 100 K, 200 K and 350 K and (d-f) flexible cage at 100 K, 200 K and 350 K.

To further investigate to what extent the FA ions interact with the lead iodide cage we again look at scatter plots with all dipole directions of the FA ions in a single system, both for molecular dynamics simulations with frozen and flexible cage. The obtained results at 100 K, 200 K and 350 K can be observed in Figure 3.7.

For both simulations we can already see that the ion alignment is not completely random at high temperatures as there is higher density at certain angles. In both cases these are angles that lead to the dipole of the FA ion pointing in-between two iodines. This can be explained through hydrogen bonding between iodine and the hydrogens on the nitrogen molecules. If the dipole points between two iodines the nitrogens can point towards the iodines, allowing the hydrogen bonds to form. As the temperature is lowered these alignments become more prominent in both cases.

This high degree of order in the FA orientation at low temperatures explains why large domains were observed for these systems above. If the ion alignments are restricted to only few possible orientations, large domains will be obatined even though the dipole-dipole interactions do not play any role in the alignment. One major difference is visible

between the low temperature simulations for frozen and flexible cage. For the flexible cage the FA ions align both in the azimuthal plane and perpendicular to it. In the frozen cage simulations the ions however only align in the azimuthal plane.

To gain insight in the timescale of the specific interaction we have again analyzed the hydrogen bond life-times as shown in figure 3.4b. The lifetimes observed for FAPI at low temperature are considerably longer than for MAPI. One may interpret this as an indication of stronger hydrogen bonds, however, the life time is affected by all the interactions in the system, including steric hindrance that hampers the rotational motion of FA in the Pb-I cage, and effect due to cage deformation.

3.4. GENERAL DISCUSSION AND CONCLUSIONS

It is clear from the simulations presented in this chapter that the phase behavior and the rotational dynamics of the organic cation are intricately linked for both MAPI and FAPI. For MAPI a very clear phase transition is observed at which the MA cation becomes immobilized, and at the same time the Pb-I lattice deforms. The phase transition is accompanied by the formation of domains in which the MA dipoles arrange in an ordered, energetically favorable structure. This domain formation is already observed if only the dipole-dipole interactions are taken into account but the effect becomes much stronger if the cations are embedded in the Pb-I lattice especially when the lattice is allowed to deform in reaction to the alignment. This points to a mechanism where phase transitions are induced by mutual alignment of the dipoles, both by interactions with neighboring dipole and specific interactions between the MA cations and the Pb-I lattice. This happens in a concerted way with the deformation of the Pb-I lattice, which strengthens this effect and makes the transition from freely rotating dipoles to ordered domains with fixed dipole directions more abrupt at certain temperature.

For FAPI a very similar picture emerges, however, in this case the dipole-dipole interactions in the non-dipolar FA cation are negligible. Simulations of the dipole dynamics in fixed, cubic Pb-I cage structures show that specific interaction between FA and the Pb and I ions, and between the quadrupolar FA ions, still lead to the formation of ordered domains, even if the Pb-I lattice is not allowed to deform. In the fully flexible MD simulations where full relaxation of the lattice is possible, this effect is strengthened and domain formation is more abrupt at a certain temperature. As discussed above, the formation of hydrogen-bond like conformations plays an important role in FAPI, which, combined with increased steric interactions leads to slower rotation dynamics of FA in FAPI.

We conclude that the phase transitions that occur in hybrid halide perovskites are caused by a complex interplay between dipole-dipole interactions, specific electrostatic and steric interactions between the organic cations and the metal halide lattice, and relaxation of the metal halide cage structure. This leads to large organized domains of organic cations, which can have important consequences for the electronic structure of these materials.

REFERENCES

[1] Maheshwari, S.; Fridriksson, M. B.; Seal, S.; Meyer, J.; Grozema, F. C. The Relation between Rotational Dynamics of the Organic Cation and Phase Transitions in Hybrid Halide Perovskites. *J. Phys. Chem. C* **2019**, *123*, 14652–14661.

[2] Brauer, J. C.; Lee, Y. H.; Nazeeruddin, M. K.; Banerji, N. Charge Transfer Dynamics from Organometal Halide Perovskite to Polymeric Hole Transport Materials in Hybrid Solar Cells. *J. Phys. Chem. Lett.* **2015**, *6*, 3675–3681.

[3] NREL Best Research Cell Efficiency, howpublished = https://www.nrel.gov/pv/assets/images/efficiency-chart.png, note = Accessed: 2018-05-14.

[4] Shin, S. S.; Yeom, E. J.; Yang, W. S.; Hur, S.; Kim, M. G.; Im, J.; Seo, J.; Noh, J. H.; Seok, S. I. Colloidally prepared La-doped BaSnO3 electrodes for efficient, photostable perovskite solar cells. *Science* **2017**, *356*, 167–171.

[5] Umari, P.; Mosconi, E.; De Angelis, F. Infrared Dielectric Screening Determines the Low Exciton Binding Energy of Metal-Halide Perovskites. *J. Phys. Chem. Lett.* **2018**, *9*, 620–627.

[6] Leguy, A. M. A.; Frost, J. M.; McMahon, A. P.; Sakai, V. G.; Kochelmann, W.; Law, C.; Li, X.; Foglia, F.; Walsh, A.; O'Regan, B. C.; Nelson, J.; Cabral, J. T.; Barnes, P. R. F. The dynamics of methylammonium ions in hybrid organic-inorganic perovskite solar cells. *Nat. Commun.* **2015**, *6*, 7124.

[7] Wu, X.; Trinh, M. T.; Niesner, D.; Zhu, H.; Norman, Z.; Owen, J. S.; Yaffe, O.; Kudisch, B. J.; Zhu, X.-Y. Trap States in Lead Iodide Perovskites. *J. Am. Chem. Soc.* **2015**, *137*, 2089–2096.

[8] Weller, M. T.; Weber, O. J.; Henry, P. F.; Pumpo, A. M. D.; Hansen, T. C. Complete structure and cation orientation in the perovskite photovoltaic methylammonium lead iodide between 100 and 352 K. *ChemComm* **2015**, *51*, 4180–4183.

[9] Gélvez-Rueda, M. C.; Cao, D. H.; Patwardhan, S.; Renaud, N.; Stoumpos, C. C.; Schatz, G. C.; Hupp, J. T.; Farha, O. K.; Savenije, T. J.; Kanatzidis, M. G.; Grozema, F. C. Effect of Cation Rotation on Charge Dynamics in Hybrid Lead Halide Perovskites. *J. Phys. Chem. C* **2016**, *120*, 16577–16585.

[10] Bernard, G. M.; Wasylishen, R. E.; Ratcliffe, C. I.; Terskikh, V.; Wu, Q.; Buriak, J. M.; Hauger, T. Methylammonium Cation Dynamics in Methylammonium Lead Halide Perovskites: A Solid-State NMR Perspective. *J. Phys. Chem. A* **2018**, *122*, 1560–1573.

[11] Whitfield, P. S.; Herron, N.; Guise, W. E.; Page, K.; Cheng, Y. Q.; Milas, I.; Crawford, M. K. Structures, Phase Transitions and Tricritical Behavior of the Hybrid Perovskite Methyl Ammonium Lead Iodide. *Sci. Rep.* **2016**, *6*, 35685.

[12] Poglitsch, A.; Weber, D. Dynamic disorder in methylammoniumtrihalogenoplumbates (II) observed by millimeterwave spectroscopy. *J. Chem. Phys* **1987**, *87*, 6373–6378.

[13] Mattoni, A.; Filippetti, A.; Saba, M. I.; Delugas, P. Methylammonium Rotational Dynamics in Lead Halide Perovskite by Classical Molecular Dynamics: The Role of Temperature. *J. Phys. Chem. C* **2015**, *119*, 17421–17428.

[14] Bernard, G. M.; Wasylishen, R. E.; Ratcliffe, C. I.; Terskikh, V.; Wu, Q.; Buriak, J. M.; Hauger, T. Methylammonium Cation Dynamics in Methylammonium Lead Halide Perovskites: A Solid-State NMR Perspective. *J. Phys. Chem. A* **2018**, *122*, 1560–1573.

[15] Guo, Y.; Yaffe, O.; Paley, D. W.; Beecher, A. N.; Hull, T. D.; Szpak, G.; Owen, J. S.; Brus, L. E.; Pimenta, M. A. Interplay between organic cations and inorganic framework and incommensurability in hybrid lead-halide perovskite $CH_3NH_3PbBr_3$. *Phys. Rev. Materials* **2017**, *1*, 42401.

[16] Frost, J. M.; Butler, K. T.; Walsh, A. Molecular ferroelectric contributions to anomalous hysteresis in hybrid perovskite solar cells. *APL Mater.* **2014**, *2*, 81506.

[17] Li, J.; Rinke, P. Atomic structure of metal-halide perovskites from first principles: The chicken-and-egg paradox of the organic-inorganic interaction. *Phys. Rev. B* **2016**, *94*, 45201.

[18] Bokdam, M.; Lahnsteiner, J.; Ramberger, B.; Schäfer, T.; Kresse, G. Assessing Density Functionals Using Many Body Theory for Hybrid Perovskites. *Phys. Rev. Lett.* **2017**, *119*, 145501.

[19] Lahnsteiner, J.; Kresse, G.; Kumar, A.; Sarma, D. D.; Franchini, C.; Bokdam, M. Room-temperature dynamic correlation between methylammonium molecules in lead-iodine based perovskites: An ab initio molecular dynamics perspective. *Phys. Rev. B* **2016**, *94*, 214114.

[20] Weller, M. T.; Weber, O. J.; Frost, J. M.; Walsh, A. Cubic Perovskite Structure of Black Formamidinium Lead Iodide, α-[HC(NH2)2]PbI3, at 298 K. *J. Phys. Chem. Lett.* **2015**, *6*, 3209–3212.

[21] Fabini, D. H.; Siaw, T. A.; Stoumpos, C. C.; Laurita, G.; Olds, D.; Page, K.; Hu, J. G.; Kanatzidis, M. G.; Han, S.; Seshadri, R. Universal Dynamics of Molecular Reorientation in Hybrid Lead Iodide Perovskites. *J. Am. Chem. Soc.* **2017**, *139*, 16875–16884.

[22] Carignano, M. A.; Saeed, Y.; Aravindh, S. A.; Roqan, I. S.; Even, J.; Katan, C. A close examination of the structure and dynamics of HC(NH2)2PbI3 by MD simulations and group theory. *Phys. Chem. Chem. Phys.* **2016**, *18*, 27109–27118.

[23] Weber, O. J.; Ghosh, D.; Gaines, S.; Henry, P. F.; Walker, A. B.; Islam, M. S.; Weller, M. T. Phase Behavior and Polymorphism of Formamidinium Lead Iodide. *Chem. Mater.* **2018**, *30*, 3768–3778.

[24] Chen, T.; Foley, B. J.; Ipek, B.; Tyagi, M.; Copley, J. R. D.; Brown, C. M.; Choi, J. J.; Lee, S.-H. Rotational dynamics of organic cations in the CH3NH3PbI3 perovskite. *Phys. Chem. Chem. Phys.* **2015**, *17*, 31278–31286.

[25] Govinda, S.; Kore, B. P.; Bokdam, M.; Mahale, P.; Kumar, A.; Pal, S.; Bhattacharyya, B.; Lahnsteiner, J.; Kresse, G.; Franchini, C.; Pandey, A.; Sarma, D. D. Behavior of Methylammonium Dipoles in MAPbX3 (X = Br and I). *J. Phys. Chem. Lett.* **2017**, *8*, 4113–4121.

[26] Handley, C. M.; Freeman, C. L. A new potential for methylammonium lead iodide. *Phys. Chem. Chem. Phys.* **2017**, *19*, 2313–2321.

[27] Taylor, V. C. A.; Tiwari, D.; Duchi, M.; Donaldson, P. M.; Clark, I. P.; Fermin, D. J.; Oliver, T. A. A. Investigating the Role of the Organic Cation in Formamidinium Lead Iodide Perovskite Using Ultrafast Spectroscopy. *J. Phys. Chem. Lett.* **2018**, *9*, 895–901.

[28] Weller, M. T.; Weber, O. J.; Frost, J. M.; Walsh, A. Cubic Perovskite Structure of Black Formamidinium Lead Iodide, α-[HC(NH2)2]PbI3, at 298 K. *J. Phys. Chem. Lett.* **2015**, *6*, 3209–3212.

[29] Vincent, Z.; A., C. M.; Aurélien, G.; Olivier, M. SwissParam: A fast force field generation tool for small organic molecules. *J. Comput. Chem. 32*, 2359–2368.

[30] Vanommeslaeghe, K.; Hatcher, E.; Acharya, C.; Kundu, S.; Zhong, S.; Shim, J.; Darian, E.; Guvench, O.; Lopes, P.; Vorobyov, I.; Mackerell Jr., A. D. CHARMM general force field: A force field for drug-like molecules compatible with the CHARMM all-atom additive biological force fields. *J. Comput. Chem.* **2010**, *31*, 671–690.

[31] Vanommeslaeghe, K.; MacKerell, A. D. Automation of the CHARMM General Force Field (CGenFF) I: Bond Perception and Atom Typing. *J. Chem. Inf. Model.* **2012**, *52*, 3144–3154.

[32] Vanommeslaeghe, K.; Raman, E. P.; MacKerell, A. D. Automation of the CHARMM General Force Field (CGenFF) II: Assignment of Bonded Parameters and Partial Atomic Charges. *J. Chem. Inf. Model.* **2012**, *52*, 3155–3168.

[33] Plimpton, S. Fast Parallel Algorithms for Short-Range Molecular Dynamics. *J. Comput. Phys.* **1995**, *117*, 1–19.

[34] Frost, J. M.; Walsh, A. What Is Moving in Hybrid Halide Perovskite Solar Cells? *Acc. Chem. Res.* **2016**, *49*, 528–535.

[35] Bakulin, A. A.; Selig, O.; Bakker, H. J.; Rezus, Y. L.; Müller, C.; Glaser, T.; Lovrincic, R.; Sun, Z.; Chen, Z.; Walsh, A.; Frost, J. M.; Jansen, T. L. C. Real-Time Observation of Organic Cation Reorientation in Methylammonium Lead Iodide Perovskites. *J. Phys. Chem. Lett.* **2015**, *6*, 3663–3669.

[36] Kubicki, D. J.; Prochowicz, D.; Hofstetter, A.; Péchy, P.; Zakeeruddin, S. M.; Grätzel, M.; Emsley, L. Cation Dynamics in Mixed-Cation (MA)x(FA)1–xPbI3 Hybrid Perovskites from Solid-State NMR. *J. Am. Chem. Soc.* **2017**, *139*, 10055–10061.

4

PACKING OF THE ORGANIC CATIONS IN MIXED-CATION HALIDE PEROVSKITES

The intermixing and dynamics of cations in mixed $FA_xMA_{(1-x)}PbI_3$ perovskites is not explored in detail because of the difficult crystal formation of these materials. The positions of cations methylammonium(MA) and formamidinium(FA) in the mixed $FA_xMA_{(1-x)}PbI_3$ can severely affect the energetics of the system and reorientation motion of these organic cations. The preference of the arrangement of the cations can also reveal the mechanism of formation of mixed cation hybrid perovskites. Molecular dynamics model simulations of these systems are used in our study to gain insights in the energetics of the system and dynamics of organic cations. These simulations are able to take into account large system size of 12000 atoms. Simulations on seven different models of mixed cation $FA_{0.5}MA_{0.5}PbI_3$ perovskites are performed. The energetics of these systems are studied to understand the preference of MA and FA cations to stay farther or closer to each other. It is also found that the motion of the organic cations varies in these arrangements and may include slowing down of reorientation in some cases.

4.1. MIXED ORGANIC CATION HYBRID PEROVSKITES

Devices based on hybrid halide perovskite layers that contain only a single type of organic cation, for instance methylammonium (MA^+), formamidinium (FA^+) or cesium(Cs^+) have saturated in terms of efficiency around 20%.[1–4] The central problem that these monocation perovskite materials suffer from is a lack of stability of their perovskite phases. The solution for overcoming the lack of stability and improving the absorption at the same time has been the introduction of mixed-cation and mixed halide perovskites. These mixed perovskites contain combinations of two or three A-site cations (from)FA^+, MA^+ and Cs^+) with either one or two halides (bromide(Br^-) and iodide(I^-)). The pure FA-based perovskites have a smaller band gap than the MA ones, but are unstable and prone to form a yellow α-$FAPbI_3$ phase. Mixing FA into a pure MA based lead iodide perovskite leads to a material with a lower band gap than the pure MA material, but with a stable perovskite phase.[5] It is also known that the mixed cation composition of hybrid perovskites exhibit lower hysteresis and result in higher efficiency photovoltaic devices.[6, 7]

Despite the successes in using these mixed cation MA/FA perovskite materials in solar cells, their structural properties and associated dynamics of the organic cations are not fully understood. This is due of the complicated crystallization process of these materials. The $FA_xMA_{(1-x)}PbI_3$ is known to crystallize in a cubic phase at room temperature for $x \geq 0.2$ and is tetragonal for $x = 0 - 0.1$. The lattice constant of the cubic lattice is found to increase with increasing the fraction of FA^+.[8] Kuno and coworkers have shown that in the thin films of these materials, the organic cations have a heterogeneous distribution.[9] Using magic angle spinning NMR, Emsley and coworkers have shown that both MA^+ and FA^+ have a different reorientation time in $FA_{0.67}MA_{0.33}PbI_3$. They have also shown that the reorientation of MA^+ is not isotropic and reorientation dynamics of FA^+ is also different from its pure phase. From these observations it was concluded that MA^+ exists in two different environments at lower temperature.[10] The structural dynamics of mixed halide $MAPbI_xBr_{3-x}$ and $MAPbBr_xCl_{1-x}$ perovskites were studied by Gallop et al.[11] They concluded from molecular simulations that a long lived component arises in the autocorrelation decay for the MA cation in the sub-ensemble of unit cells, whereas most MA cations behave similar to pure $MAPbX_3$. This was attributed to the existence of asymmetry in the lattice as a result of the variety of halides. The resulting asymmetric potential locks the organic cation in an energetic minimum, leading to reduced rotational dynamics. This illustrates the complexities in the rotational dynamics of the organic cations in the mixed $FA_xMA_{(1-x)}PbI_3$ perovskites.

The dynamics and electronic structure of mixed-cation perovskites are to a large extent determined by the distribution of the different organic cations over the material. As discussed in the previous chapter, the organic cations markedly affect each others dynamics and orientation, forming oriented domains at low temperature. The formation of these domains have direct consequences for the charge transport properties of mixed-cation perovskites.

In order to gain insight in the dynamics and energetic of mixed-cation perovskites, we have performed molecular dynamics simulations on different model systems of mixed

cation $FA_xMA_{(1-x)}PbI_3$ perovskites. Different model systems of $FA_{0.5}MA_{0.5}PbI_3$ were generated by placing the organic cations in an organized way in a 10x10x10 lattice. Seven of these arrangements were studied for energetics and cation dynamics. It is found that the motion of the organic cations varies in these arrangements. The effect of anisotropy of the organic cation is not restricted to just one unit cell but is experienced by several surrounding cations. This includes the slowing down of the rotational motion of the organic cations. An analysis of the different interaction energy component sheds a new light on the arrangement and preferred organization of cations in these mixtures.

4.2. METHODOLOGY

The molecular dynamics (MD) simulations were performed on a super cell of 10x10x10 unit cells with periodic boundary conditions. The different initial configurations for the 50% mixture of MA and FA were generated with a cubic unit cell size of 6.34065 Å. The unit cell size was computed using the already available knowledge of the lattice constants of MAPI and FAPI. The system size was chosen sufficiently large to obtain sufficient statistics and independence of the motion of dipolar cations in different parts of the system. The force field for the interatomic potentials was adopted from the work of Mattoni et. al.[12] The interactions in the force field are defined in form of three components i) inorganic-inorganic(U_{ii}), ii) inorganic-organic(U_{io}) and iii) organic-organic(U_{oo}) interactions. The U_{ii} and U_{io} are non-bonded interactions which are defined in terms of Buckingham and Lennard-Jones parameters that take into account electrostatic and Van der Waals interactions. U_{oo} interactions are defined as bonded interactions with parameters for bond stretching, angle bending and dihedral rotations for the organic cations. These parameters were obtained from the CHARMM forcefield using the SwissParam tool.[13–16] MD simulations were performed using the LAMMPS molecular dynamics simulation package.[17] The equations of motion were evaluated using time step of 1 fs and a cutoff of 17 Å for Lennard-Jones interactions and 18 Å for the Coulombic interactions. Simulations were performed in a sequence of three steps in which first step was annealing of system. The annealing was performed from a higher temperature to the temperature required for the system over 3 nanoseconds. The second step was the equilibration of the system at the required temperature of further simulation. The third step was the production run from which a trajectory file over 100 ps was obtained along with the total energy and its components for the system. The rotational dynamics of the organic cations was analyzed by examining the rotation-autocorrelation function, *C(t)* as defined in Equation 4.1 in terms of the dipole vectors μ_i of the MA and FA cations. For MA this vector coincides with the C-N axis, while for FA it is along the C-H bond.

$$C(t) = \frac{1}{N}\sum_{i=1}^{N} \vec{\mu}_i(t) \cdot \vec{\mu}_i(0) \tag{4.1}$$

This rotation-autocorrelation function gives a measure of how fast the orientations of the organic cations change with time. By definition, $C(t = 0) = 1$ and decays to zero on average once the direction of the dipole has become completely random.

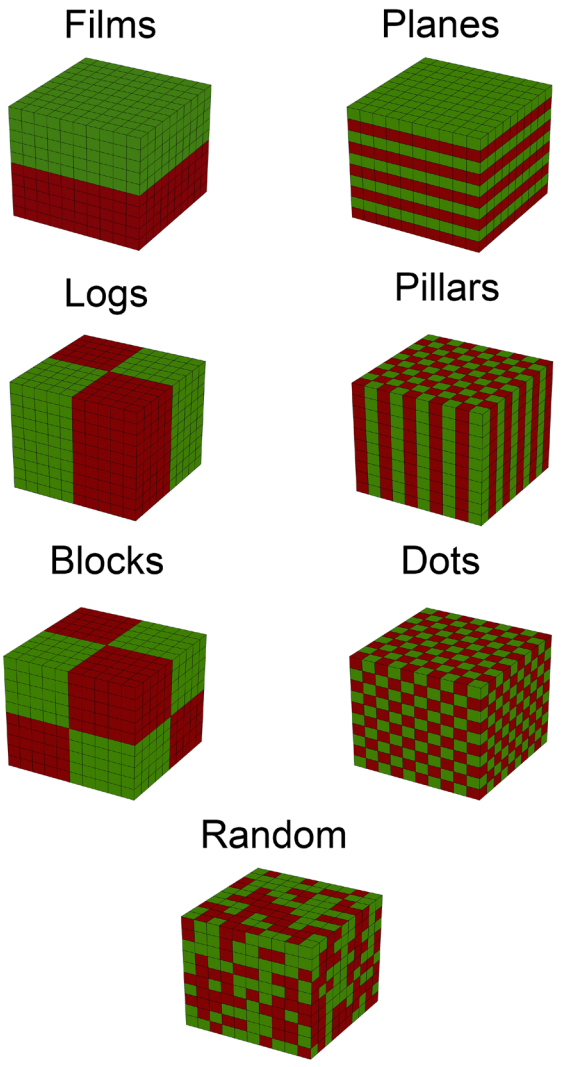

Figure 4.1: The model configurations for mixed cation $MA_{0.5}FA_{0.5}PbI_3$ system. The configurations indicated as Films, Logs and Blocks consist of large domains of the same cations whereas Planes, Pillars and Dots consist of a more inter-mixed configuration.

4.3. DISCUSSION

4.3.1. MIXED $MA_{0.5}FA_{0.5}PbI_3$ CONFIGURATIONS

In order to gain insight in the effect of the mutual organization of MA and FA cations seven different configurations have been constructed as illustrated in Figure 4.1. The configurations consist of sets of two similar types of arrangements which vary in the intermixing of MA and FA. In case of films the system consists of five layers of $FAPbI_3$ separated by five layers of $MAPbX_3$ and these layers are repeated in periodic fashion. In case of 'planes' each layer of $FAPbX_3$ is separated by a layer of $MAPbX_3$ and thus the organic cations are more inter-mixed. In the same way, other sets of configurations such as logs/pillars and blocks/dots have been generated. The trends in these configurations are compared with the random configuration of organic cations that may be closer to the experimental situation.

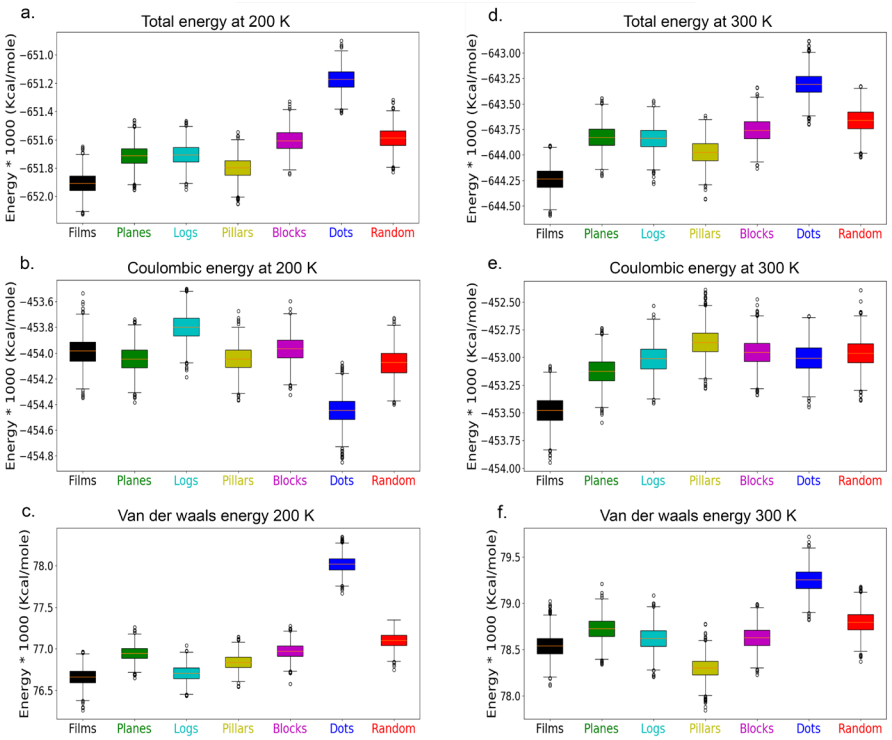

Figure 4.2: (a,d) Total energy of all the systems at 200 K and 300 K respectively. (b,e) Coulombic energy of all the systems at 200 K and 300 K respectively. (c,f) Van der waals energy of all the systems at 200 K and 300 K respectively.

Molecular dynamics simulations were performed for all the configurations shown in Figure 4.1 and an analysis of the different energy components was performed. The obtained energy trends are summarized in Figure 4.2 at temperatures of 200 K and 300 K. As is seen in Figure 4.2(a,b), the arrangement of the organic cations in the lattice results in

large variations in the total energy of system. Upon increase of temperature from 200 K to 300 K the absolute difference between the energy of different configurations increases but the overall trends remain the same. The 'film' configuration has the lowest energy whereas the 'dots' configuration is highest in energy. At room temperature, the average energies for different configurations cover a range of ≈ 1000 Kcal/mol for the 1000 unit cell system, or 1 Kcal/mol for each unit cell. This variation in energy is not very high, suggesting that all of these configurations can exist within the working temperature range of hybrid perovskites. An important thing to note here is that the 'film' configuration has the most 'phase-separated' arrangement of the two organic cations, whereas the 'dots' configuration represents the most uniformly mixed arrangement of the cations. The lower energy of the 'film' configuration indicates that a phase-separated configuration is most stable for these mixed-cation films.

4.3.2. ENERGY ANALYSIS OF CONFURATIONS

To understand the effect of the arrangement of the organic cations on the total energy of the system, the individual components of energy that lead to the interaction between the two organic cations are compared. The Coulomb and Van der Waals components of the interaction energy are summarized in Figure 4.2 c, d, e and f at 200 K and 300 K. The total electrostatic energy is negative, indicating attractive interactions. This is easily understood since the electrostatic interactions keep the Pb-I lattice together. The trend in the electrostatic energy changes somewhat from 200 K to 300 K. At 200 K, the Coulomb interactions are more favorable for the mixed configurations of 'planes', 'pillars' and 'dots. as compared to their counterparts of de-mixed configurations i.e. 'films', 'logs' and 'blocks'. As the temperature increases and the cations gain enough energy to reorient in the octahedral voids of PbI_6, the de-mixed configurations become most stable. At 300 K the electrostatic interactions are most favorable when similar cations are together when the cations are free to reorient. The Van der Waals interactions are also compared for these systems and the overall energy is always positive. This shows that repulsive Van der Waals interaction balance the strongly attractive electrostatic interaction in the Pb-I lattice. At 200K, in Figure 4.2 c it can be seen that the Van der Waals interactions are least repulsive when the organic cations are optimally mixed. This trend is partially retained at higher temperature, 300 K. The overall observation from these comparisons of the total energy for different configurations is that the phase-separated structures are most stable, indicating that strongly intermixed structures that are expected in experiments are meta-stable at best.

4.3.3. DEFORMATION OF Pb-I CAGE

In order to gain insight in the effect that the distribution of the organic cations has on the deformation of the Pb-I cages the radial distribution function for the lead and iodide atoms was calculated and shown in Figure 4.3. It is clear that the differences between different configuration are rather small. In the case of films the maxima and minima in the peaks of the radial distribution exhibit the least variation. This variation increases in case of other arrangements and is highest in case of pillars. This shows that in the 'pil-

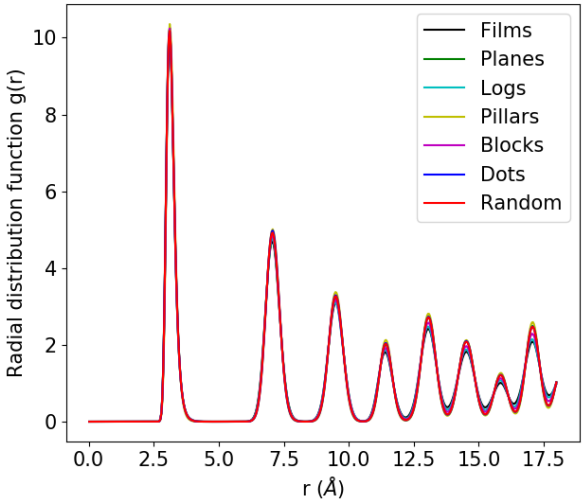

Figure 4.3: Radial distribution function plotted as distance of iodide (I^-) atoms as function of distance from lead $Pb^{(2+)}$atoms at 300 K

lars' arrangement the iodide-lead distance varies the least whereas in films the variation is largest. This variation suggests increased motion of the Pb-I atoms in the demixed configurations than in the mixed ones.

4.3.4. ROTATIONAL-AUTOCORRELATION OF MA AND FA CATION MOTION

The different organization of the two organic cations in the perovskite structure may also have an effect on the rotational dynamics of the organic cations. This can be characterized by the rotation autocorrelation function shown in Figure 4.4a,b. The rotational decay of MA is similar for all configurations, which shows that the motion of MA cation is minimally affected by the surrounding cations. The small variation that is observed is consistent with the average hydrogen bond lifetimes shown in Figure 4.4c. The rotational decay pattern for FA cations is in general slower than that for MA, as also observed for the pure systems in Chapter 3. For films and pillars a particularly slow autocorrelation decay pattern is observed for FA here, consistent with longer hydrogen bond lifetimes. The observed small differences are likely to be caused by interactions with the (deformed) lattice.

4.4. CONCLUSION

In conclusion, we have modeled seven different configurations for $MA_{0.5}FA_{0.5}PbI_3$ with a motivation to assess the effects of the degree of mixing of MA and FA on the energy of system and on the energy of the system and rotational dynamics of MA and FA. From these calculations it can be seen that the mixed organic cation configurations are ener-

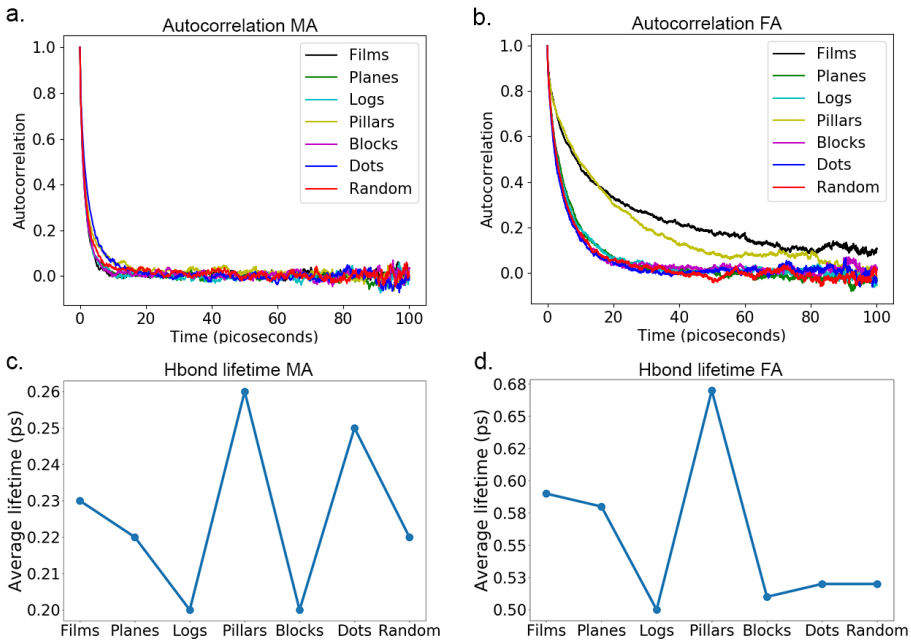

Figure 4.4: At the temperatures of 300K (a) Rotation autocorrelation plotted for all MA in the system, (b) Rotation autocorrelation for all FA in the system, (c) Hydrogen bond lifetime for all the MA cations in the configurations and (d) Hydrogen bond lifetime for all the FA cations in the configurations

getically less favourable than the demixed configurations. This can in part be traced back to the specific interactions between the different components in the system but a more detailed analysis is required in the future to draw definite conclusions on the origins.The system of mixed cation $MA_{0.5}FA_{0.5}PbI_3$ will thus tend to form in a de-mixed configuration. The motion of the MA cations is affected less by the surrounding cations but for FA cations, some configurations can make the motion of this cation slower.

REFERENCES

[1] Son, D.-Y.; Lee, J.-W.; Choi, Y. J.; Jang, I.-H.; Lee, S.; Yoo, P. J.; Shin, H.; Ahn, N.; Choi, M.; Kim, D.; Park, N.-G. Self-formed grain boundary healing layer for highly efficient CH3 NH3 PbI3 perovskite solar cells. *Nat. Energy.* **2016**, *1*, 16081.

[2] Momblona, C.; Gil-Escrig, L.; Bandiello, E.; Hutter, E. M.; Sessolo, M.; Lederer, K.; Blochwitz-Nimoth, J.; Bolink, H. J. Efficient vacuum deposited p-i-n and n-i-p perovskite solar cells employing doped charge transport layers. *Energy Environ. Sci.* **2016**, *9*, 3456–3463.

[3] Pool, V. L.; Dou, B.; Van Campen, D. G.; Klein-Stockert, T. R.; Barnes, F. S.; Shaheen, S. E.; Ahmad, M. I.; van Hest, M. F. A. M.; Toney, M. F. Thermal engineering of FAPbI3 perovskite material via radiative thermal annealing and in situ XRD. *Nat. Commun.* **2017**, *8*, 14075 EP –, Article.

[4] Kim, Y. G.; Kim, T.-Y.; Oh, J. H.; Choi, K. S.; Kim, Y.-J.; Kim, S. Y. Cesium lead iodide solar cells controlled by annealing temperature. *Phys. Chem. Chem. Phys.* **2017**, *19*, 6257–6263.

[5] Binek, A.; Hanusch, F. C.; Docampo, P.; Bein, T. Stabilization of the Trigonal High-Temperature Phase of Formamidinium Lead Iodide. *J. Phys. Chem. Lett.* **2015**, *6*, 1249–1253.

[6] Sun, Y.; Peng, J.; Chen, Y.; Yao, Y.; Liang, Z. Triple-cation mixed-halide perovskites: towards efficient, annealing-free and air-stable solar cells enabled by Pb(SCN)2 additive. *Sci. Rep* **2017**, *7*, 46193.

[7] Zhang, Y.; Grancini, G.; Feng, Y.; Asiri, A. M.; Nazeeruddin, M. K. Optimization of Stable Quasi-Cubic FAxMA1–xPbI3 Perovskite Structure for Solar Cells with Efficiency beyond 20%. *ACS Energy. Lett.* **2017**, *2*, 802–806.

[8] Weber, O. J.; Charles, B.; Weller, M. T. Phase behaviour and composition in the formamidinium–methylammonium hybrid lead iodide perovskite solid solution. *J. Mater. Chem. A* **2016**, *4*, 15375–15382.

[9] Chatterjee, R.; Pavlovetc, I. M.; Aleshire, K.; Hartland, G. V.; Kuno, M. Subdiffraction Infrared Imaging of Mixed Cation Perovskites: Probing Local Cation Heterogeneities. *ACS Energy Lett.* **2018**, *3*, 469–475.

[10] Kubicki, D. J.; Prochowicz, D.; Hofstetter, A.; Péchy, P.; Zakeeruddin, S. M.; Grätzel, M.; Emsley, L. Cation Dynamics in Mixed-Cation (MA)x(FA)1–xPbI3 Hybrid Perovskites from Solid-State NMR. *J. Am. Chem. Soc.* **2017**, *139*, 10055–10061.

[11] Gallop, N. P.; Selig, O.; Giubertoni, G.; Bakker, H. J.; Rezus, Y. L. A.; Frost, J. M.; Jansen, T. L. C.; Lovrincic, R.; Bakulin, A. A. Rotational Cation Dynamics in Metal Halide Perovskites: Effect on Phonons and Material Properties. *J. Phys. Chem. Lett.* **2018**, *9*, 5987–5997.

[12] Mattoni, A.; Filippetti, A.; Saba, M. I.; Delugas, P. Methylammonium Rotational Dynamics in Lead Halide Perovskite by Classical Molecular Dynamics: The Role of Temperature. *J. Phys. Chem. C* **2015**, *119*, 17421–17428.

[13] Vincent, Z.; A., C. M.; Aurélien, G.; Olivier, M. SwissParam: A fast force field generation tool for small organic molecules. *J. Comput. Chem. 32*, 2359–2368.

[14] Vanommeslaeghe, K.; Hatcher, E.; Acharya, C.; Kundu, S.; Zhong, S.; Shim, J.; Darian, E.; Guvench, O.; Lopes, P.; Vorobyov, I.; Mackerell Jr., A. D. CHARMM general force field: A force field for drug-like molecules compatible with the CHARMM all-atom additive biological force fields. *J. Comput. Chem.* **2010**, *31*, 671–690.

[15] Vanommeslaeghe, K.; MacKerell, A. D. Automation of the CHARMM General Force Field (CGenFF) I: Bond Perception and Atom Typing. *J. Chem. Inf. Model.* **2012**, *52*, 3144–3154.

[16] Vanommeslaeghe, K.; Raman, E. P.; MacKerell, A. D. Automation of the CHARMM General Force Field (CGenFF) II: Assignment of Bonded Parameters and Partial Atomic Charges. *J. Chem. Inf. Model.* **2012**, *52*, 3155–3168.

[17] Plimpton, S. Fast Parallel Algorithms for Short-Range Molecular Dynamics. *J. Comput. Phys.* **1995**, *117*, 1 – 19.

5

COMPUTATIONAL DESIGN OF 2D PEROVSKITES WITH FUNCTIONAL ORGANIC CATIONS

Two-dimensional halide perovskites are a class of materials in which two-dimensional layers of perovskite are separated by large organic cations. Conventionally the two-dimensional perovskites incorporate organic cations as spacers but these organic cations also offer a route to introduce specific functionality in the material. In this work we demonstrate, by density functional theory calculations, that the introduction of electron withdrawing and electron donating molecules leads to the formation of localized states, either in the organic or the inorganic part. Furthermore, we show that the energy of the bands located in the organic and inorganic parts can be tuned independently. The organic cation levels can be tuned by changing the electron withdrawing/donating character, while the energy levels in the inorganic part can be modified by varying the number of inorganic perovskite layers. This opens a new window for the design of 2D perovskites with properties tuned for specific applications.

This chapter is based on from S. Maheshwari, T. J. Savenije, N. Renaud, and F. C. Grozema, *J. Phys. Chem. C* **2018**, 122 (30), pp 17118–17122.

5.1. INTRODUCTION

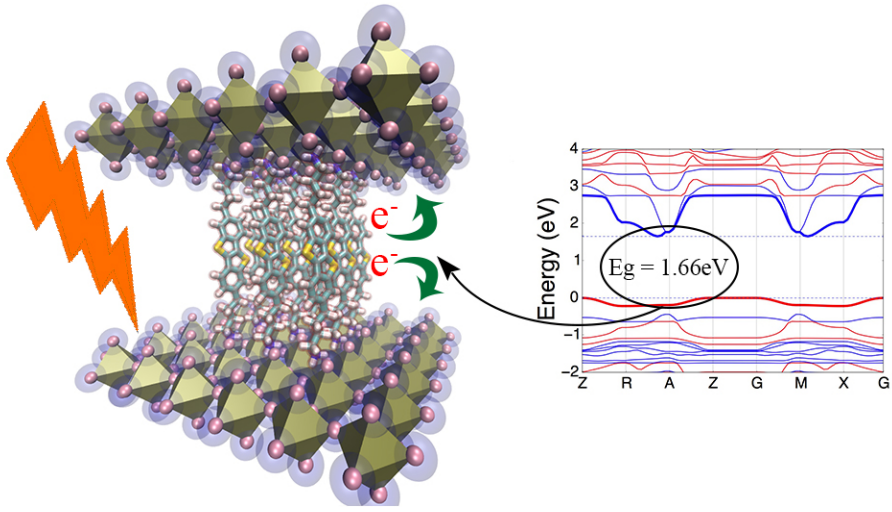

The two-dimensional versions of hybrid halide perovskites are an emerging class of opto-electronic materials displaying robust environmental stability as compared to their 3D counterparts.[1] These materials have not been studied as extensively as the 3D equivalents but they have been considered for applications such as photodetectors [2], lasers[3], field effect transistors[4] and light emitting devices[4, 5]. They structurally differ from the 3D perovskites because the organic cation in these materials is not limited in size by Goldschmidt tolerance factor. This allows for the introduction of a wider choice of bulkier organic cations, including aromatic and divalent ones. Previous theoretical studies on the 2D perovskites with varying organic cations, have predicted that a change in the structure of the organic cation can result in a modulation of the steric effects, electronic structure and electronic properties of the material.[6] In a separate study with similar systems it was shown that the 2D perovskites assume similar effective masses for the charge carriers in both valence and conduction bands.[7]

2D A_2MX_4 or BMX_4 perovskites consists of bulky monovalent cation A^+ or divalent cation B^{2+} as the organic component. MX_4 is the tetrahalogenide or inorganic component of the material consisting for instance of Pb^{2+} (M) and I^- (X) atoms. The basic crystal packing of these hybrid materials is a self-assembled, layered structure where single sheets of corner shared MX_6 octahedra and bilayers of organic cations are stacked alternately, held together by Coulombic and Van der Waals forces.[8] The interest in these materials is not new as their quantum-well structure has been studied for over two decades. In 1988 Goto and coworkers first reported a high exciton binding energy for one such material. The exciton binding energy for $(C_{10}H_{21}NH_3)_2PbI_4$ was found to be ten times higher than that of PbI_2.[9] This difference was attributed to the two-dimensional character of the exciton and the small dielectric constant of the long alkyl chains. The 2D perovskites also display much more efficient photoluminescence than their 3-dimensional counterparts because of the existence of bound excitons in the metal halide sheets. The

quantum and dielectric confinement due to the organic cation strongly affects the exciton binding energy of the material, which is generally in the range of 200 − 300 meV.[10] Therefore, the charge carriers in these materials primarily exist in the form of bound excitons at room temperature.[11] The chemical and physical properties of 2D perovskites are highly tunable as compared to those of its 3D counterpart. This is because the layer thickness of the 2D sheets can be modulated by introducing organic cations of different size.[12, 13]

When the monovalent large organic cations are mixed with the small cations like methylammonium and formamidinium, which are generally used to form 3D perovskites, it is possible to create so-called Ruddlesden-Popper phases of hybrid perovskites. The divalent large organic cations on the other hand form Dion-Jacobson 2D perovskites which were recently developed by Mao et. al with composition of aminomethylpiperidinium organic cations.[14] Within both Ruddlesden-Popper and Dion-Jacobson perovskite structures the inorganic layers incorporate smaller organic cation and are separated from each other through spacers of the bulky organic cations.[13–15] These quasi-2D materials have been demonstrated to be useful as the active material in photovoltaic cells, albeit with considerably lower efficiency than their fully 3D counterpart. [13, 16] We have recently shown that the exciton binding energy strongly depends of the number of inorganic layers in between the bulky organic cations. The binding energy was found to decrease from 370 meV for the purely 2D materials to 80 meV for a material with four inorganic lead-iodide layers between the organic part.[17] This shows that modifications in the number of inorganic layers do not only affect the bandgap of the material, but also the efficiency of charge generation.

Until now, most of the bulky organic cations used in 2D or quasi-2D perovskite materials mainly contribute in defining the physical attributes of the material including dimensionality of the system and their phase behavior.[18, 19] These organic cations have large HOMO-LUMO gap and thus the electronic properties of the resulting materials is fully determined by the properties of the inorganic layers.[20] In this chapter, we aim to introduce new designs for the 2D layered perovskites by incorporating unconventional organic cations between the inorganic layers of leadiodide. We have investigated the electronic structure of these 2D and quasi-2D perovskites where the organic cations as strong electron donor and acceptor are introduced. We show that this leads to either valence band maxima or conduction band minima that are localized in the organic spacer layer. The positioning of these localized bands with respect to the bands in the inorganic part can be tuned by introducing additional electron donating or electron withdrawing substituents. Such materials are expected to exhibit enhanced formation of free charges upon photoexcitation, even for pure 2D systems where the exciton binding energy is very high.

5.2. COMPUTATIONAL METHODS

We have investigated the electronic structure and charge transport properties of 2D perovskites in which the the organic cation contains 2,7-Dibutylammonium[1]benzothieno[3,2-

b][1]benzothiophene (BTBT), N,N-Bis(n-butylammonium)perylene-3,4,9,10-tetracarboxylic diimide (PDI) and N,N-Bis(n-butylammonium)naphthalene-1,4,5,8-tetracarboxylic diimide (NDI) chromophores as the functional component. These organic chromophores are well-know from organic electronics and offer a chance to combine the properties of perovskites and organic semiconductors.[21–24] The optimization of the X-PbI_4 structures was performed using projector augmented wave (PAW) pseudopotentials with van der Waals corrected PBE-sol exchange correlation functional as implemented in VASP 5.4.1.[25–30] Relativistic effects were included fully for the core electrons for each atom and the scalar relativistic approximation was applied for the valence electrons. An energy cutoff of 500 eV and a gamma centered brillouin zone sampling grid of 4 X 4 X 2 were chosen for the calculations. The ionic positions were relaxed while conserving the tetragonal lattice shape for continuous values of lattice parameter. Band structures of the different X-PbI_4 geometries were then computed at the DFT level of theory at a denser mesh in the direction of high symmetry.

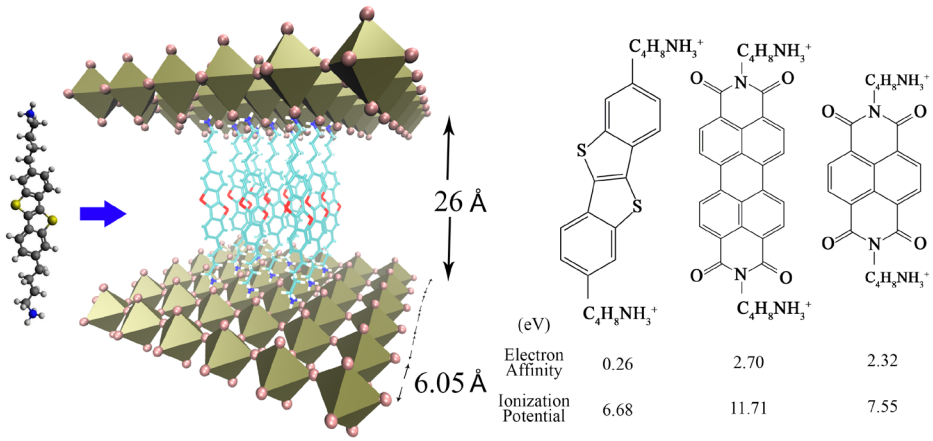

Figure 5.1: (nBu-NH_3)$_2$BTBT as the organic molecule between the inorganic sheets of with PbI_4 layer depicting Pb-Pb distance as 6.05Åand the interlayer distance as 26Å. The molecular structure of BTBT, PDI and NDI functional organic molecules and their electron affinity and ionization potential values.

Table 5.1: The lattice constants for the tetragonal unit cell of the optimised geometry of X-PbI_4, where X =(nBu-NH_3)$_2$BTBT, X =(nBu-NH_3)$_2$PDI and X =(nBu-NH_3)$_2$NDI.

	BTBT	PDI	NDI
a (Å)	6.05	6.05	6.05
c (Å)	26.00	28.00	23.7

5.3. RESULTS AND DISCUSSION

To introduce organic cations with added functionality to the 2D perovskite materials we have chosen electron donating and electron withdrawing compounds that are well-know

from organic electronics. We have performed DFT calculations on 2D sheets of leadiodide where conjugated chromophores with amonium groups coupled by alkyl linker are introduced. The structure of these organic cations together with their electron affinity and ionization potential values are shown in Figure 5.1. As seen in this figure, the electron affinity is high for the electron acceptor molecules PDI and NDI and much smaller for the electron donor molecule BTBT. The ionization potential is lowest for BTBT and higher for the electron acceptors PDI and NDI.

5.3.1. $(C_4H_9\text{-}NH_3)_2BTBT$

The geometry optimization of X-PbI_4 where X referes to the functional organic cation, was performed to obtain the lattice constants for a tetragonal lattice. The system with electron donating cation X = (nBu-NH_3)$_2$BTBT is referred to as BTBT further. The optimised geometry for BTBT assumes a unit cell with lattice parameters ***a***=6.05Åand ***c***=26.00 Åas shown in Figure 5.1 and reported in Table 5.1. Here ***a*** corresponds to the in-plane distance between the neighboring lead atoms and ***c*** corresponds to the distance between the planes of the inorganic sheets of leadiodide. The lattice constant ***a*** is smaller as compared to that of the reported Ruddlesden Popper phase 2D perovskites with butylammonium as the organic cation and having Pb-Pb distance of 6.216Å. [15] A smaller distance between the lead and iodide atoms in the inorganic sheet ensures stronger coupling between neighboring atoms, leading to improved charge transport. The band structure computed for the optimized geometry of BTBT is shown in the Figure 5.2a. It is plotted with different colors for the bands located on the organic molecule and the lead-iodide perovskite sheet. A bandgap of 1.66 eV is obtained for this system, close to the band gap for methylammonium leadiodide.[31]. The value of the bandgap is considerably lower than that of the single layer lead iodide perovskite with butylammonium as the organic cation and shows the effect of the organic cation on the bandgap tunibility of the 2D system of lead iodide.[15] To visualize the valence band maximum and conduction band minimum a band-decomposed charge density was extracted as shown in Figure 5.2b. The highest valence band for BTBT is localized on the aromatic core of organic cation, whereas the lowest conduction band is localized on the lead iodide layers. This clearly shows that BTBT acts as a donor of electrons in this organic-inorganic system of 2D perovskites.

The electron donating nature of the organic molecule can be modified by introduction of electron donating(-NH_2) and withdrawing(-F) groups on the aromatic core, see Figure 5.2c,d. The substitution of electron donating -NH_2 groups leads to a shift of the bands localized on the organic cation to higher energy whereas substitution of -F groups leads to the shift of the bands of the organic cation to lower energy. These substitutions have a negligible effect on the position of the perovskite bands. The bandgap of the system decreases to 1.03eV with electron donating amine groups whereas fluorides lead to increase in bandgap to 2.42 eV. This shows that the bands localized on the organic part of the material can be modified, indepedent of the band on the inorganic part. Similarly, we can modify the electronic structure of the inorganic part by changing the number of inorganic layers. We have computed the band structure for Ruddlesden-Popper structure with multiple layers of perovskite (N=2 and N=3) in between the organic layers. The

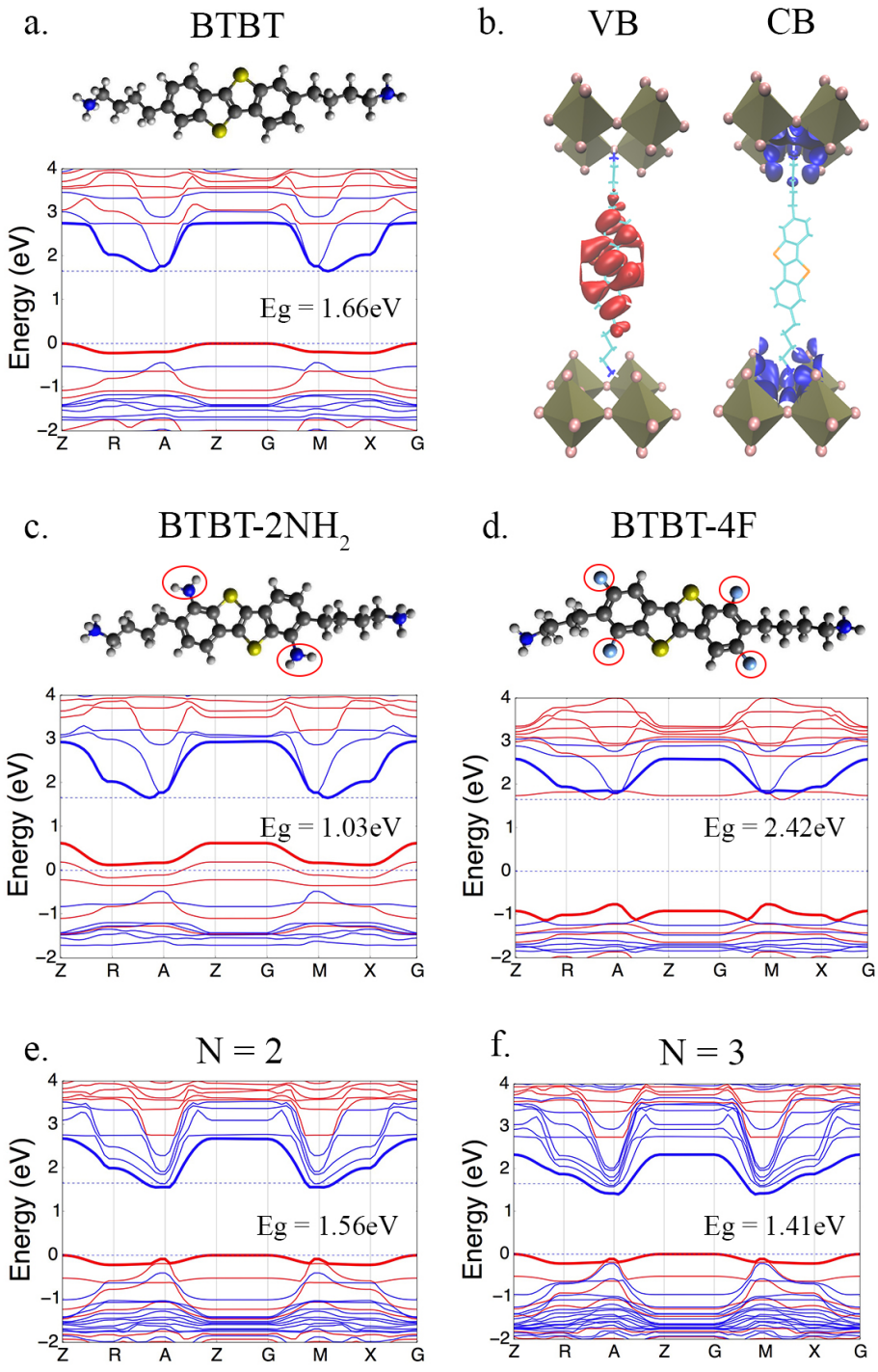

Figure 5.2: (a) The band structure of optimized geometry of X-PbI_4 where X=(nBu-NH_3)$_2$BTBT. The bands in blue are localised on PbI_4 sheets whereas bands in red are localised on the organic cation. (b) Band decomposed charge density for valence band maximum and conduction band minimum for BTBT. (c) Band structure for -NH_2 substitution on BTBT. (d) Band structure for -F substitution on BTBT. (e) Band structure for n=2 in (nBu-NH_3)$_2$BTBTPb_nI_{3*n+1}. (f) Band structure for n=3 in (nBu-NH_3)$_2$BTBTPb_nI_{3*n+1}.

band structures for these materials are shown in Figure 5.2e,f. The bandgap of the system decreases with increasing the perovskite layers which is 1.56eV for N=2 and 1.41eV for N=3. This is caused by a movement of the conduction bands, localised on the inorganic part, to lower energies.

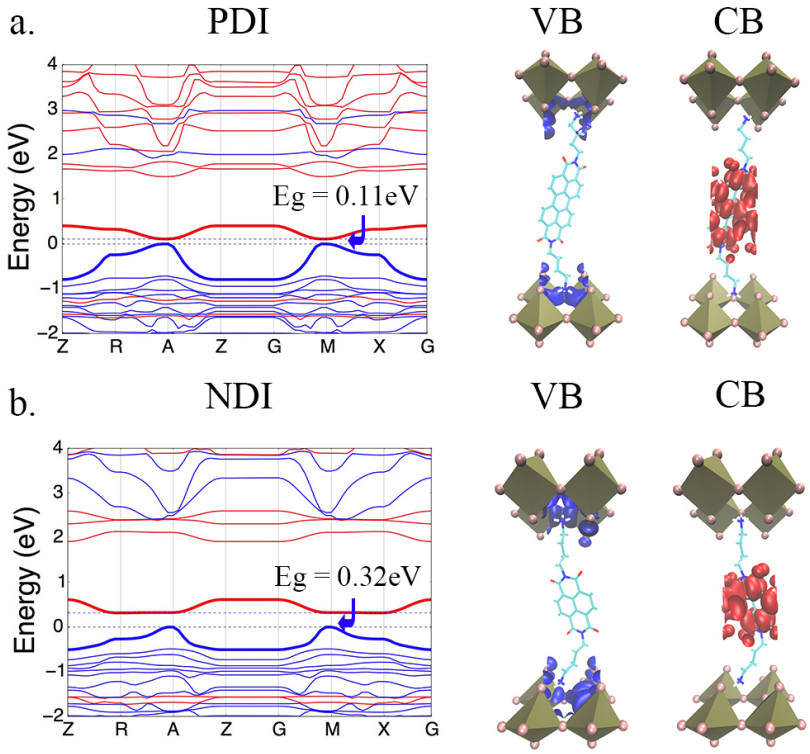

Figure 5.3: (a) The band structure of optimized geometry of (nBu-NH_3)$_2$PDIPbI_4. The bands in blue depicitng contribution from the inorganic PbI_4 whereas bands in red depicting contribution from (nBu-NH_3)$_2$PDI. (b) The band structure of optimized geometry of (nBu-NH_3)$_2$NDIPbI_4. The bands in blue depicitng contribution from the inorganic PbI_4 whereas bands in red depicting contribution from (nBu-NH_3)$_2$NDI. Band decomposed charge density for valence band maximum and conduction band minimum can be seen with each bandstructure.

5.3.2. (C_4H_9-NH_3)$_2$PDI AND (C_4H_9-NH_3)$_2$NDI

To study the effect of the introduction of electron withdrawing groups the cations X = (nBu-NH_3)$_2$PDI and (nBu-NH_3)$_2$NDI (referred to as PDI and NDI) were considered. The optimized lattice constants for both of these compounds are reported in Table 5.1. The in-plane Pb-Pb distance is the same for all the three structures investigated, indicating that changes in the core of the organic cation have only a small effect on the distance between the lead atoms in the 2D inorganic sheets. In the optimized geometry for PDI and NDI molecules π-stacked structures can be observed. Such π-stacking was not observed

for BTBT due to the smaller size of its core. The formation of π-stacks is important in these systems as it can introduce pathway for charge transport through the organic layers. The band structures computed for the optimized geometry of PDI-PbI_4 and NDI-PbI_4 are shown in Figure 5.3. The band gap of these systems is much lower than for the BTBT system, 0.11 eV and 0.32 eV, respectively. A band decomposition of the charge density for the PDI and NDI systems shows that the highest valence band is localised on the lead iodide layer, while the lowest conduction band is localised on aromatic core of the organic molecule. This is opposite to what was observed for the electron donating BTBT cation above.

5.3.3. CHARGE TRANSPORT PROPERTIES

Table 5.2: The effective mass of electrons and holes for BTBT, PDI and NDI within the 2D sheets and perpendicular to the sheets.

	BTBT		PDI		NDI	
	m_h^*	m_e^*	m_h^*	m_e^*	m_h^*	m_e^*
within sheets	3.88	0.12	0.32	7.83	0.24	1.83
perpendicular to sheets	209.9	293.1	64.5	49.3	21.7	27.7

To gain insight in the charge transport properties these systems with electron donors and acceptor, the effective masses were calculated by a band fitting method for the highest valence band and lowest conduction band for the various combinations of organic cations with leadiodide sheets in Table 5.2. The effective masses within the 2D sheet are lower than those perpendicular to the sheet in all cases. This indicates, as expected, that transport perpendicular to the inorganic layers is very inefficient as compared to the in-plane transport. For the 2D system with BTBT the effective mass of the electrons is 0.12 which is much lower compared to the effective mass for holes which is 3.88. This is because of the localization of the respective bands. The electrons are in the inorganic layers where they can move easily, while the holes are in the BTBT layer where transport relies on coupling between the different molecules that are relatively far apart. For PDI and NDI the effective masses are opposite to those for BTBT, the hole mass is lower than the electron mass. As shown above, in PDI and NDI the hole is localized in the inorganic layer where it can move freely, whereas the electrons are on the organic part where transport relies on π-π-interaction between neighboring molecules. The electronic structure of these materials is considerably different than those previously published for 2D Ruddlesden-Popper phases containing butylammonium as the organic cation spacers. The effective masses for both electrons and holes in these phases is in the range of $0.08m_e - 0.14m_e$. Also the organic cations here do not participate in charge transport.[13] Thus the inclusion of novel organic cations in organic layers offers a possibility to improve the charge transport in the organic part by engineering the π-stacking in this layer.

5.4. CONCLUSION

In conclusion of this chapter we have performed a DFT based study of 2D hybrid perovskites where functional organic cations are incorporated that have strongly electron donating or withdrawing capacities. We show that the energies of these organic molecules can be such that either the valence band or the conduction band becomes localized on the organic part of the materials. This is stark contrast to the commonly used organic cations that only serve as a spacer layer that does not affect the electronic properties. We also show that it is possible to tune the alignment of the energy levels in the organic part by introducing additional donating and accepting groups such as amines or fluorines. This tuning leaves the band energies in the inorganic part unaffected. A similar tuning can be done in the inorganic part by varying the number of inorganic perovskite layers between the organic part of the materials. These results illustrate that the properties of two-dimensional halide perovskites can be tuned by introduction of functional organic units. This offers a new approach to tune the properties of these materials to develop stable 2D perovskites with specific functionality, for instance improved charge separation for photovoltaic applications.

REFERENCES

[1] Smith, I. C.; Hoke, E. T.; SolisIbarra, D.; McGehee, M. D.; Karunadasa, H. I. A layered hybrid perovskite solarcell absorber with enhanced moisture stability. *Angew. Chem.* **2014**, *126*, 11414–11417.

[2] Dou, L.; Wong, A. B.; Yu, Y.; Lai, M.; Kornienko, N.; Eaton, S. W.; Fu, A.; Bischak, C. G.; Ma, J.; Ding, T.; Ginsberg, N. S.; Wang, L.-W.; Alivisatos, A. P.; Yang, P. Atomically thin two-dimensional organic-inorganic hybrid perovskites. *Science* **2015**, *349*, 1518–1521.

[3] Deschler, F.; Price, M.; Pathak, S.; Klintberg, L. E.; Jarausch, D.-D.; Higler, R.; Hüttner, S.; Leijtens, T.; Stranks, S. D.; Snaith, H. J.; Atatüre, M.; Phillips, R. T.; Friend, R. H. High photoluminescence efficiency and optically pumped lasing in solution-processed mixed halide perovskite semiconductors. *J. Phys. Chem. Lett.* **2014**, *5*, 1421–1426.

[4] Kagan, C. R.; Mitzi, D. B.; Dimitrakopoulos, C. D. Organic-inorganic hybrid materials as semiconducting channels in thin-film field-effect transistors. *Science* **1999**, *286*, 945–947.

[5] Tan, Z.-k.; Moghaddam, R. S.; Lai, M. L.; Docampo, P.; Higler, R.; Deschler, F.; Price, M.; Sadhanala, A.; Pazos, L. M.; Credgington, D.; Hanusch, F.; Bein, T.; Snaith, H. J.; Friend, R. H. Bright light-emitting diodes based on organometal halide perovskite. *Nature Nanotechnology* **2014**, *9*, 687–692.

[6] Fraccarollo, A.; Cantatore, V.; Boschetto, G.; Marchese, L.; Cossi, M. Ab initio modeling of 2D layered organohalide lead perovskites. *The Journal of Chemical Physics* **2016**, *144*, 164701.

[7] Pedesseau, L.; Sapori, D.; Traore, B.; Robles, R.; Fang, H.-H.; Loi, M. A.; Tsai, H.; Nie, W.; Blancon, J.-C.; Neukirch, A.; Tretiak, S.; Mohite, A. D.; Katan, C.; Even, J.; Kepenekian, M. Advances and promises of layered halide hybrid perovskite semiconductors. *ACS Nano* **2016**, *10*, 9776–9786, PMID: 27775343.

[8] Ahmad, S.; Kanaujia, P. K.; Beeson, H. J.; Abate, A.; Deschler, F.; Credgington, D.; Steiner, U.; Prakash, G. V.; Baumberg, J. J. Strong photocurrent from two-dimensional excitons in solution-processed stacked perovskite semiconductor sheets. *ACS Appl. Mater. Interfaces* **2015**, *7*, 25227–25236, PMID: 26497547.

[9] Ishihara, T.; Takahashi, J.; Goto, T. Exciton state in two-dimensional perovskite semiconductor $(C_{10}H_{21}NH_3)_2PbI_4$. *Solid State Communications* **1989**, *69*, 933–936.

[10] Muljarov, E. A.; Tikhodeev, S. G.; Gippius, N. A.; Ishihara, T. Excitons in self-organized semiconductor/insulator superlattices: PbI-based perovskite compounds. *Phys. Rev. B* **1995**, *51*, 14370–14378.

[11] Yani, C.; Yong, S.; Jiajun, P.; Junhui, T.; Kaibo, Z.; Ziqi, L. 2D Ruddlesden–Popper perovskites for optoelectronics. *Advanced Materials* **2018**, *30*, 1703487.

[12] Rodriguez-Romero, J.; Hames, B. C.; Mora-Seró, I.; Barea, E. M. Conjugated organic cations to improve the optoelectronic properties of 2D/3D perovskites. *ACS Energy Lett.* **2017**, *2*, 1969–1970.

[13] Stoumpos, C. C.; Cao, D. H.; Clark, D. J.; Young, J.; Rondinelli, J. M.; Jang, J. I.; Hupp, J. T.; Kanatzidis, M. G. Ruddlesden–Popper Hybrid Lead Iodide Perovskite 2D Homologous Semiconductors. *Chem. Mater.* **2016**, *28*, 2852–2867.

[14] Mao, L.; Ke, W.; Pedesseau, L.; Wu, Y.; Katan, C.; Even, J.; Wasielewski, M. R.; Stoumpos, C. C.; Kanatzidis, M. G. Hybrid Dion–Jacobson 2D Lead Iodide Perovskites. *J. Am. Chem. Soc.* **2018**, *140*, 3775–3783.

[15] Cao, D. H.; Stoumpos, C. C.; Farha, O. K.; Hupp, J. T.; Kanatzidis, M. G. 2D homologous perovskites as light-absorbing materials for solar cell applications. *J. Am. Chem. Soc.* **2015**, *137*, 7843–7850.

[16] Tsai, H. et al. High-efficiency two-dimensional Ruddlesden–Popper perovskite solar cells. *Nature* **2016**, *536*, 312–316.

[17] Gelvez-Rueda, M. C.; Hutter, E. M.; Cao, D. H.; Renaud, N.; Stoumpos, C. C.; Hupp, J. T.; Savenije, T. J.; Kanatzidis, M. G.; Grozema, F. C. Interconversion between free charges and bound excitons in 2D hybrid lead halide perovskites. *J. Phys. Chem. C* **2017**, *121*, 26566–26574.

[18] Needham, G. F.; Willett, R. D.; Franzen, H. F. Phase transitions in crystalline models of bilayers. 1. Differential scanning calorimetric and x-ray studies of (C12H25NH3)2MCl4 and (NH3C14H29NH3)2MCl4 salts (M = Mn2+, Cd2+, Cu2+). *J. Phys. Chem.* **1984**, *88*, 674–680.

[19] Saparov, B.; Mitzi, D. B. Organic–Inorganic Perovskites: Structural Versatility for Functional Materials Design. *Chem. Rev.* **2016**, *116*, 4558–4596, PMID: 27040120.

[20] Mitzi, D. B.; Chondroudis, K.; Kagan, C. R. Design, structure, and optical properties of organicinorganic perovskites containing an oligothiophene chromophore. *Inorg. Chem.* **1999**, *38*, 6246–6256.

[21] Ebata, H.; Izawa, T.; Miyazaki, E.; Takimiya, K.; Ikeda, M.; Kuwabara, H.; Yui, T. Highly soluble [1]Benzothieno[3,2-b]benzothiophene (BTBT) derivatives for high-performance, solution-processed organic field-effect transistors. *J. Am. Chem. Soc.* **2007**, *129*, 15732–15733.

[22] Yang, J.; Xiao, B.; Tajima, K.; Nakano, M.; Takimiya, K.; Tang, A.; Zhou, E. Comparison among Perylene Diimide (PDI), Naphthalene Diimide (NDI), and Naphthodithiophene Diimide (NDTI) Based n-Type Polymers for All-Polymer Solar Cells Application. *Macromolecules* **2017**, *50*, 3179–3185.

[23] Marcon, V.; Breiby, D. W.; Pisula, W.; Dahl, J.; Kirkpatrick, J.; Patwardhan, S.; Grozema, F.; Andrienko, D. Understanding StructureMobility Relations for Perylene Tetracarboxydiimide Derivatives. *J. Am. Chem. Soc.* **2009**, *131*, 11426–11432.

[24] Herbst, W.; Hunger, K.; Wilker, G.; Ohleier, H.; Winter, R. *Industrial Organic Pigments: Production, Properties, Applications, Third Edition*; Wiley, 2005.

[25] Blöchl, P. E. Projector augmented-wave method. *Phys. Rev. B* **1994**, *50*, 17953–17979.

[26] Kresse, G.; Joubert, D. From ultrasoft pseudopotentials to the projector augmented-wave method. *Phys. Rev. B* **1999**, *59*, 1758–1775.

[27] Grimme, S.; Antony, J.; Ehrlich, S.; Krieg, H. A consistent and accurate ab initio parametrization of density functional dispersion correction (DFT-D) for the 94 elements H-Pu. *The Journal of Chemical Physics* **2010**, *132*, 154104.

[28] Perdew, J. P.; Burke, K.; Ernzerhof, M. Generalized gradient approximation made simple [Phys. Rev. Lett. 77, 3865 (1996)]. *Phys. Rev. Lett.* **1997**, *78*, 1396–1396.

[29] Perdew, J. P.; Burke, K.; Ernzerhof, M. Generalized gradient approximation made simple. *Phys. Rev. Lett.* **1996**, *77*, 3865–3868.

[30] Perdew, J. P.; Ruzsinszky, A.; Csonka, G. I.; Vydrov, O. A.; Scuseria, G. E.; Constantin, L. A.; Zhou, X.; Burke, K. Restoring the density-gradient expansion for exchange in solids and surfaces. *Phys. Rev. Lett.* **2008**, *100*, 136406.

[31] Eperon, G. E.; Stranks, S. D.; Menelaou, C.; Johnston, M. B.; Herz, L. M.; Snaith, H. J. Formamidinium lead trihalide: a broadly tunable perovskite for efficient planar heterojunction solar cells. *Energy Environ. Sci.* **2014**, *7*, 982–988.

6

ONE-DIMENSIONAL HYBRID HALIDE PEROVSKITES DERIVATIVES

This chapter is based on M. E. Kamminga, M. C. Gélvez-Rueda, S. Maheshwari, I. S. van Droffelaar, J. Baas, G. R. Blake, F. C. Grozema and T. T. M. Palstra, *J. Solid State Chem.* **2019**, 270, 593 – 600

6.1. INTRODUCTION

The previous chapters in this thesis have dealt mainly with three-dimensional hybrid halide perovskites that have the same basic crystal structure as the inorganic parent compound $CaTiO_3$. For the two-dimensional varieties of these discussed in the previous chapter the crystal structure already deviates markedly from the basic perovskite structure, especially for the single layer derivatives. Nevertheless, the basic building blocks, the PbI_6 octahedra are still clearly recognizable in the structure, even if they organize in two-dimensional layers separated by large organic moieties. Given a certain combination of lead, halide and organic cation, it is almost impossible to predict the structure in which they will form crystalline materials. An excellent example of this is the work of Kamminga et al. who reported a series compounds that are related to the widely studied two-dimensional material containing phenyl-ethyl-ammonium (PEA) as the organic cation (see chapter 1).[1] It was shown that increasing the length of the alkyl linker between the ammonium and the phenyl leads to marked changes in the crystal structure. While the basic PEA-based materials exhibits a structure where the lead-iodide octahedra assemble in a perovskite-like corner-sharing structure, the longer organic cations result in structure with edge-shared or face-shared octahedra. This effectively leads to lower-dimensional structures which clearly emerges in their opto-electronic properties, for instance a larger band gap.

In this chapter we explore the electronic properties of three compounds that can be considered to be one-dimensional The first two stem from attempts to synthesize a tin-iodide perovskite derivative with 2,5-dimethyl-aniline (DMA) as the organic ammonium cation. Depending on the synthesis conditions, two different highly crystalline materials may be obtained: 2,5-$DMASnI_3$ that exhibits a one-dimensional perovskite-like structure or an organic charge transfer salt 2,5-$DMAI_3$. The synthesis of both materials proceeds from the same starting compounds. The obtained product depends on the presence of H_3PO_2 and the experimental conditions. The presence of H_3PO_2 promotes the formation of 2,5-$DMASnI_3$ whereas the absence of it results in the non-perovskite material 2,5-$DMAI_3$.[1]

The third compound that will be studied in this chapter is a result of attempts to include a well-known organic charge transfer salt (pyrene-TCNQ (tetracyanoquinodimethane)) in the organic part in two-dimensional hybrid halide perovskites. Such charge transfer salts known to posses exceptional optical and electronic properties including metallicity, photoconductivity, ambipolar charge transport or (low temperature) superconductivity.[2, 3] This offers an attractive approach to incorporate novel functionality in two-dimensional perovskites and it has recently been shown to be possible to make such two-dimensional materials in thin films on a substrate.[4] Crystallization of these compounds, however, results in a different structure in which lead-iodide octahedra organize in one-dimensional structures that are surrounded by pyrene-TCNQ charge transfer complexes.

While these compounds are very different than the perovskites discussed in the other chapters in this thesis, they are related in terms of structure and are formed as (unintended) by-products of the synthesis of two-dimensional perovskites. Additionally,

they have interesting opto-electronic properties that may be of interest for applications. Therefore, we have performed a theoretical study of several of these one-dimensional compounds to explore their electronic properties.

6.2. COMPUTATIONAL METHODS

DFT calculations on the one-dimensional crystals were performed using the VASP ab initio simulation package. The charge density of the structures was computed using projector augmented wave (PAW) pseudopotentials with the Van der Waals corrected PBE-sol exchange-correlation functional as implemented in VASP 5.4.1.[5–10] Relativistic effects were included fully for the core electrons, and the scalar-relativistic approximation was applied for the valence electrons. An energy cutoff of 500 eV and a gamma centered K-point grid in the Brillouin zone sampling with grid of 4 X 4 X 4 were chosen for the calculations. Band structures of the different different crystal geometries were then computed at the DFT level with a denser mesh in the direction of high symmetry.

6.3. 2,5-DMASnI$_3$

6.3.1. STRUCTURE OF 2,5-DMASnI$_3$

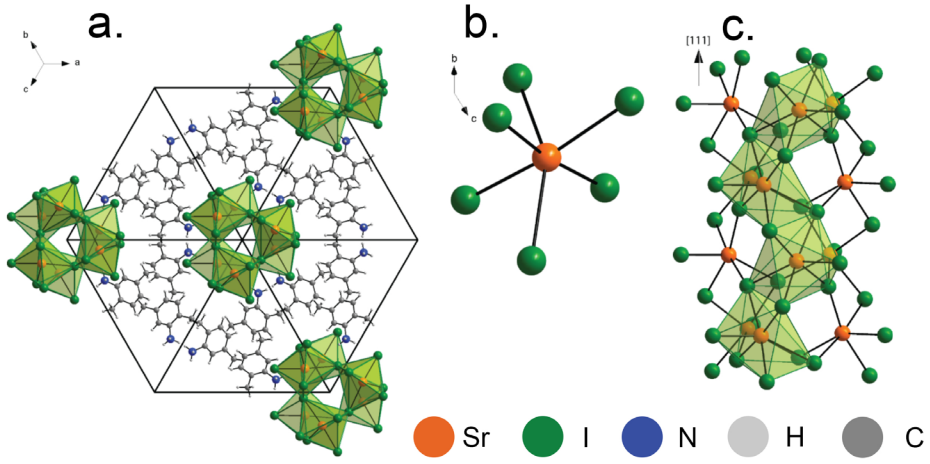

Figure 6.1: Crystal structure of 2,5-DMASnI3. (a) Polyhedral model of the full crystal structure, projected along the [111] direction. (b) A single SnI6-octahedron, showing severe distortion. (c) A single inorganic ribbon. Shading represents the strip of SnI6-octahedra that share edges. The total inorganic ribbon consists of three such edge-sharing strips that are connected through corner-sharing.

The crystal structure of 2,5-DMASnI3 is shown in Figure 6.1a. It is characterized by a one-dimensional rhombohedral structure, containing chains of SnI_6 octahedra sharing corners and edges along the [111] direction. After the refinement of the structure, the polar space group was determined as R3c. These crystals do not exhibit phase transitions between the temperatures of 100 K and 300 K as measured by thermogravimetric

analysis (TGA) and differential scanning calorimetry (DSC). It was also observed that these crystals grow as needles with [111] direction being the prominent growth direction. Figure 6.1b shows the distortion of the SnI_6 octahedra. The I-Sn-I angles deviate from 180° to 171°, 166.2° and 154.8°. The interaction between the lone pairs of the NH_+^3 groups in DMA with Sn^2+ results in this considerable distortion of the SnI_6 octahedra. The the DMA molecules that are attached to the SnI_6 octahedra arrange in a herringbone structure that leads to a relatively small $\pi - \pi$ interaction between neighboring organic molecules.

6.3.2. ELECTRONIC STRUCTURE OF 2,5-DMASnI$_3$

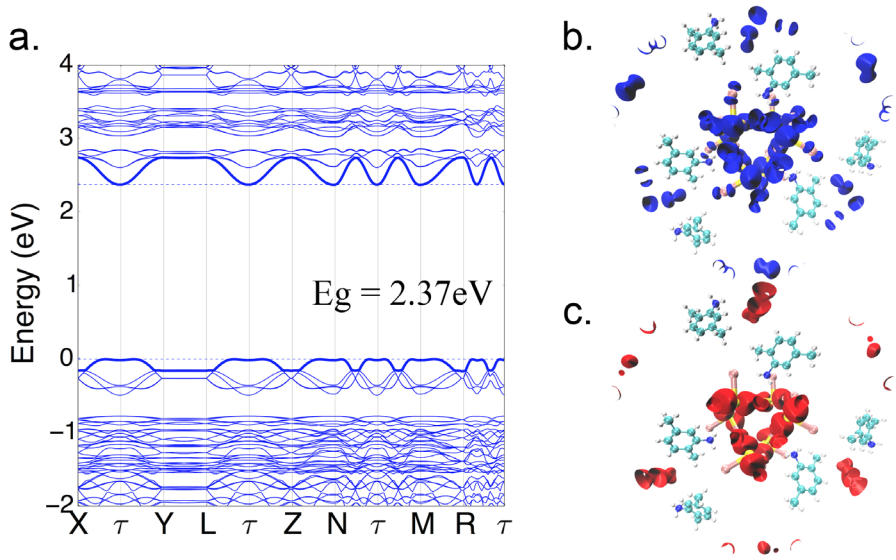

Figure 6.2: (a) Bandstructure of 2,5-DMASnI$_3$ calculated along the high symmetry path along the brillouin zone. (b) Charge density of 2,5-DMASnI$_3$ in the valence band maximum along the 1d crystal. (c) Charge density of 2,5-DMASnI$_3$ in the conduction band minimum along the 1d crystal.

In Figure 6.2 the results of the DFT calculations on 2,5-DMASnI$_3$ are shown. The band structure shown in Figure 6.2a shows that both highest valence band and lowest conduction bands are dispersive, although the valence band has a flatter structure. In Table 6.1 basic electronic properties obtained from the DFT calculations are summarized. The bandwidth of the valence band of 2,5-DMASnI$_3$ is 0.16 eV, while that of the conduction band is more than double (0.37 eV). The band gap as calculated at GGA-PBE level is 2.37 eV, which is consistent with the color of the crystals. The charge density plots for the highest valence band and the lowest conduction band are shown in Figure 6.2b,c. Both of these bands are localized on the inorganic rods of SnI_6 framework of octahedra. This indicates that excess electrons and excess positive charges will both be localized on the inorganic tin-iodide part of the material. This also means that photoexcitation of this materials results in electron and holes in the same part of the material and hence

the probability of charge separation is very low. The effective masses obtained from the DFT calculations reveal that the electrons are slightly heavier in this material than the holes, as summarized in Table 6.1.

6.4. 2,5-DMAI$_3$

6.4.1. Structure of 2,5-DMAI$_3$

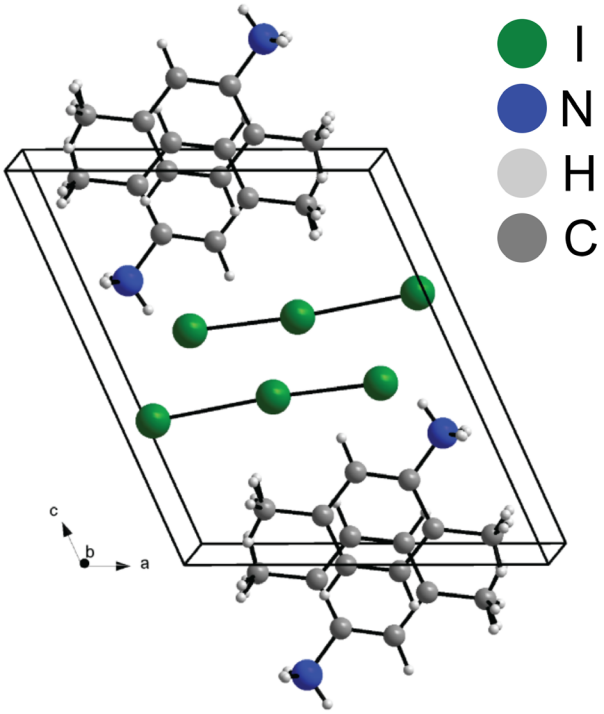

Figure 6.3: Crystal structure of DMAI$_3$. The hydrogen atoms of the methyl groups are split over two positions by symmetry and should be considered illustrative only.

Depending on the synthesis conditions, it is possible to form a crystalline organic charge transfer salt from the same precursors as used for the synthesis of 2,5-DMASnI$_3$ without inclusion of a Sn ion. This charge transfer salt, DMAI$_3$ crystallizes in a columnar structure as shown in Figure 6.3. The structure is characterized by columns of triiodide ions that are separated from each other by the DMA cations. The DSC and TGA measurements show no phase transitions between 100 K and 300 K for 2,5-DMAI$_3$. The crystals decompose at a temperature of 410 K. The distances between the two pairs of iodine atoms in a triiodide ion are 3.1373(4) Å and 2.779(3) Å. This asymmetry suggests a strong ionic character for the complex. The DMA molecules lie parallel to each other at a distance of 3.3026(6) Å, indicating good $\pi - \pi$ overlap between adjacent aromatic rings.

6.4.2. ELECTRONIC STRUCTURE OF 2,5-DMAI$_3$

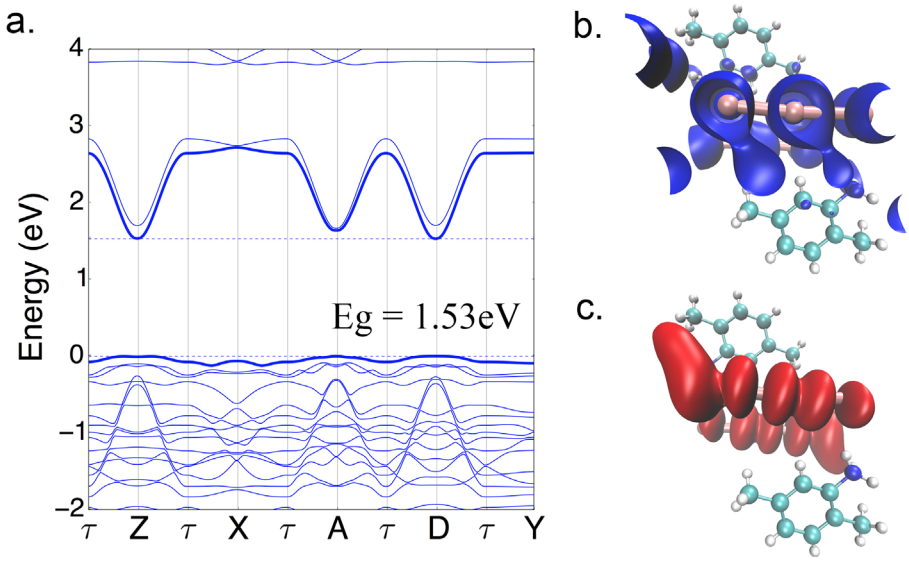

Figure 6.4: (a) Bandstructure of 2,5-DMAI$_3$ calculated along the high symmetry path along the brillouin zone showing dispersive conduction band minimum and considerably flatter valence band maximum. (b) Charge density of 2,5-DMAI$_3$ in the valence band maximum along the 1d crystal. (c) Charge density of 2,5-DMAI$_3$ in the conduction band minimum along the 1d crystal.

In Figure 6.4 the results from the electronic structure calculations on 2,5-DMAI$_3$ are shown. The calculated band structure in Figure 6.4a shows that the valence band is much flatter than the conduction band. In Table 6.1 basic electronic properties obtained from the DFT calculations on DMAI$_3$ are summarized. The width of the highest valence band (0.12 eV) is an order of magnitude smaller than that of the lowest conduction band (1.19 eV). This is also reflected in the effective masses. For the hole an effective mass of 60.88 m_0 is found, while for the electron it is only 0.59 M_0. The bandgap calculated for this structure if 1.53 eV, which is considerably smaller than for 2,5-DMASnI$_3$. Both the highest valence and the lowest conduction band are localized on the triiodide ions in the structure as can be seen in Figure 6.4b,c.

Table 6.1: Band gap, band width and effective mass of charge carriers at the top of the valence band and bottom of the conduction band for for 2,5-DMASnI3 and 2,5-DMAI3.

	2,5-DMASnI3	**2,5-DMAI3**
Bandgap (eV)	2.37	1.53
HOMO band width (eV)	0.16	0.12
LUMO band width (eV)	0.37	1.19
Hole effective mass (m*)	0.12	60.88
Electron effective mass (m*)	1.06	0.59

6.5. (PyrC4:TCNQ)Pb_2I_8

6.5.1. Introduction of charge transfer complex PyrC4:TCNQ

As discussed in the introduction section of this chapter and in Chapter 5, it is of considerable interest to introduce additional functionality in the large organic cations. In Chapter 5 the introduction of strong electron acceptors and donors was described, which was predicted to result in improved charge separation, as compared to non-functional cations such as butylammonium or phenyl-ethyl-ammonium. Another approach is to introduce strong donors **and** acceptors in the same materials. An example of this is the charge transfer salt pyrene:TCNQ, where pyrene is a moderately string donor with an ionization potential of 7.47 eV[11] and TCNQ is a string acceptor with and electron affinity of 2.33 eV.[11] It was shown recently that is is possible to incorporate such charge transfer complexes in two-dimensional perovskite film appending an alkyl-linker with an ammonium ion to the pyrene. In this way the pyrene can be incorporated in the two-dimensional perovskite structure and in addition, molecular TCNQ can be mixed in.[4] This was shown to result in a two-dimensional perovskite that exhibits the characteristic charge transfer bands that are also found in the pyrene:TCNQ charge transfer salt.[12, 13] When attempts are made to obtain single crystals of this compounds a different, one-dimensional structure is found, which by itself has interesting properties. Among the expected properties are the formation of a charge transfer state where electrons and holes localize on different part of the material, similar to the two-dimension materials in Chapter 5.

6.5.2. Structure of (PyrC4:TCNQ)Pb_2I_8

The crystal structure of the one-dimensional (PyrC4:TCNQ)Pb_2I_8 is shown in Figure 6.5. The structure shows one-dimensional chains of PbI_6 octahedra to which pyrene-alkylammonium ions are coordinated. The TCNQ molecules are intercalated between the pyrene moieties, as is characteristic for a charge transfer salt.

6.5.3. Electronic structure of (PyrC4:TCNQ)Pb_2I_8

The band structure calculated for (PyrC4:TCNQ)Pb_2I_8 is shown in Figure 6.6. The calculated band gap for this crystal is 0.35 eV, which is considerably lower than the experimental value, 1.1 eV. This is not unexpected as DFT usually underestimates the band gap unless range-separated exchange correlation functionals are used. This is especially true for the energy of states that have a pronounced charge transfer character. In Figure 6.6 bands are color-coded to indicate the major contributing species to the individual bands. The bands marked in blue are localized mainly on the lead iodide part of the crystal. The ones in red have the major density on the TCNQ molecule, while the ones marked in green are mostly localized on pyrene.

It is clear from this color coding that the highest valence band is mainly localized on the lead-iodide part of the materials, with states on pyrene only just below it. The lowest valence band is localized on the string electron acceptor, TCNQ. This is also reflected in the charge densities calculated at the gamma point in the Brillouin zone, as shown in

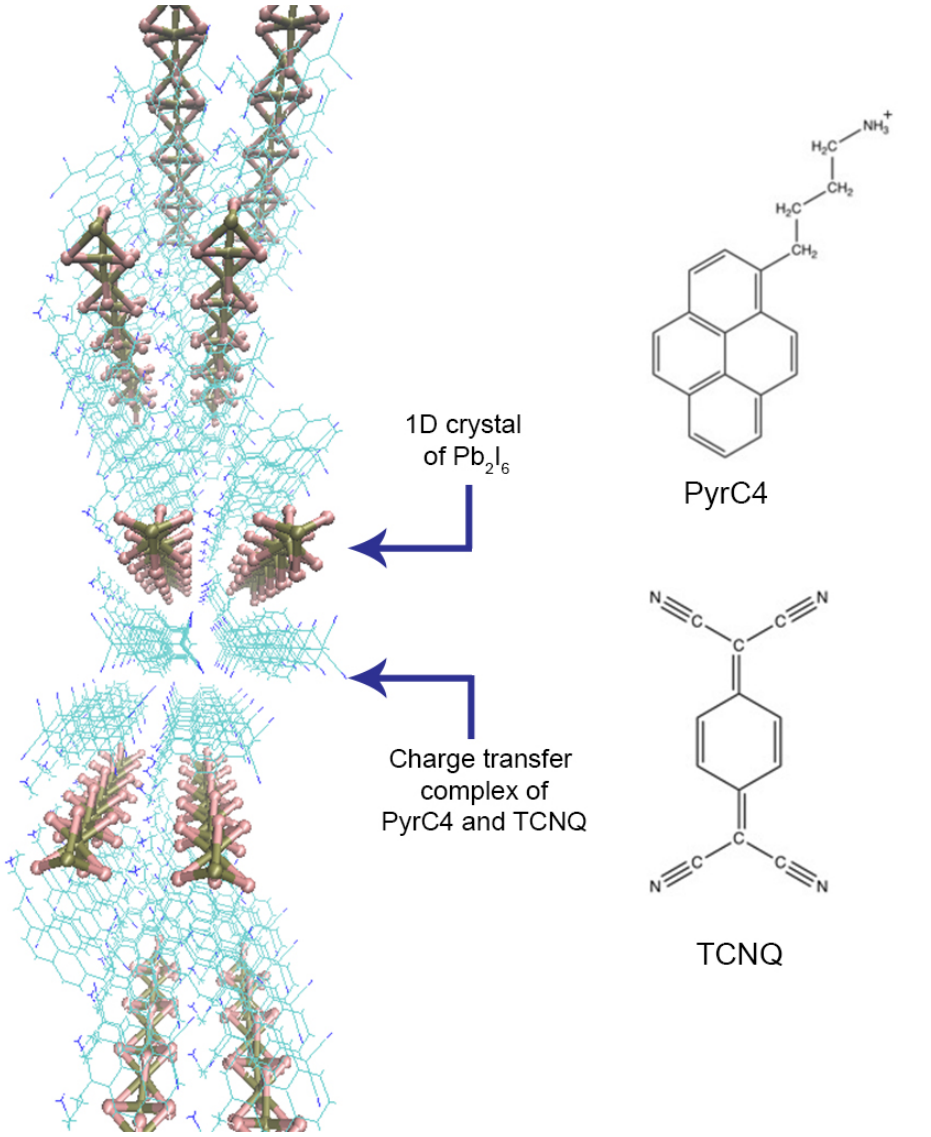

Figure 6.5: Structure of (PyrC4:TCNQ)Pb_2I_8 on the left showing the 1d inorganic crystals separated from each other by the charge transfer organic complex of PyrC4 and TCNQ. On the right are the structures of PyrC4 and TCNQ

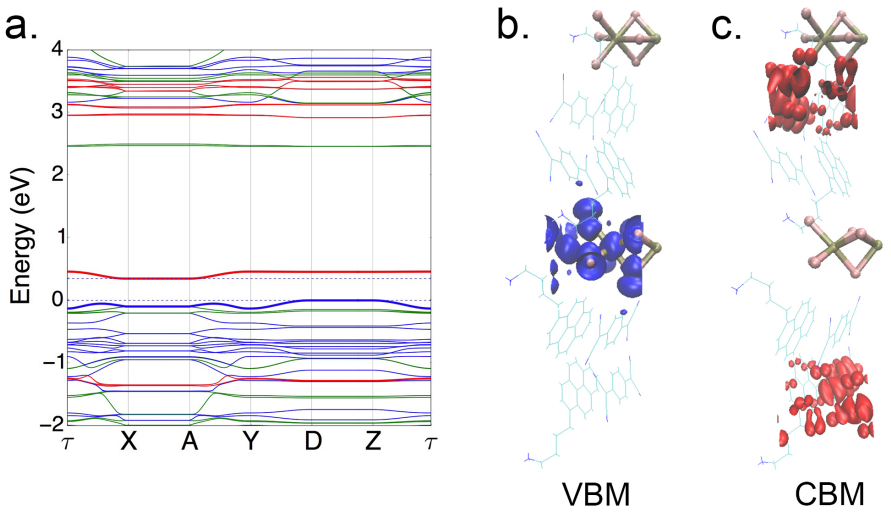

Figure 6.6: (a) Bandstructure of (PyrC4:TCNQ)Pb_2I_8 calculated along the high symmetry path along the brillouin zone. (b) Charge density of (PyrC4:TCNQ)Pb_2I_8 in the valence band maximum along the 1d crystal. (c) Charge density of (PyrC4:TCNQ)Pb_2I_8 in the conduction band minimum along the TCNQ.

Figure 6.6 b,c. The valence band maximum is dispersive in the direction of the repeating units of lead iodide in Brillouin zone, while for the other (perpendicular) directions they are relatively flat. This indicates that charge transport will be mostly along the lead iodide chains and not in other directions for these crystals. The lowest conduction band is largely localized on the TCNQ molecules, with minor contributions on the pyrenes that separate the TCNQ molecules in the stack. This band is dispersive in the direction of the π-stack consisting of pyrene and TCNQ molecules. This means that charge transport mainly takes place along this stacking direction.

REFERENCES

[1] Kamminga, M. E.; Gélvez-Rueda, M. C.; Maheshwari, S.; van Droffelaar, I. S.; Baas, J.; Blake, G. R.; Grozema, F. C.; Palstra, T. T. Electronic mobility and crystal structures of 2,5-dimethylanilinium triiodide and tin-based organic-inorganic hybrid compounds. *J. Solid State Chem.* **2019**, *270*, 593 – 600.

[2] Goetz, K. P.; Vermeulen, D.; Payne, M. E.; Kloc, C.; McNeil, L. E.; Jurchescu, O. D. Charge-transfer complexes: new perspectives on an old class of compounds. *J. Mater. Chem. C* **2014**, *2*, 3065–3076.

[3] Zhang, J.; Xu, W.; Sheng, P.; Zhao, G.; Zhu, D. Organic Donor–Acceptor Complexes as Novel Organic Semiconductors. *Acc. Chem. Res* **2017**, *50*, 1654–1662.

[4] Van Gompel, W. T. M.; Herckens, R.; Van Hecke, K.; Ruttens, B.; D'Haen, J.; Lutsen, L.; Vanderzande, D. Towards 2D layered hybrid perovskites with enhanced functionality: introducing charge-transfer complexes via self-assembly. *Chem. Commun.* **2019**, *55*, 2481–2484.

[5] Blöchl, P. E. Projector augmented-wave method. *Phys. Rev. B* **1994**, *50*, 17953–17979.

[6] Kresse, G.; Joubert, D. From ultrasoft pseudopotentials to the projector augmented-wave method. *Phys. Rev. B* **1999**, *59*, 1758–1775.

[7] Grimme, S.; Antony, J.; Ehrlich, S.; Krieg, H. A consistent and accurate ab initio parametrization of density functional dispersion correction (DFT-D) for the 94 elements H-Pu. *J. Chem. Phys* **2010**, *132*.

[8] Perdew, J. P.; Burke, K.; Ernzerhof, M. Generalized Gradient Approximation Made Simple [Phys. Rev. Lett. 77, 3865 (1996)]. *Phys. Rev. Lett.* **1997**, *78*, 1396–1396.

[9] Perdew, J. P.; Burke, K.; Ernzerhof, M. Generalized Gradient Approximation Made Simple. *Phys. Rev. Lett.* **1996**, *77*, 3865–3868.

[10] Perdew, J. P.; Ruzsinszky, A.; Csonka, G. I.; Vydrov, O. A.; Scuseria, G. E.; Constantin, L. A.; Zhou, X.; Burke, K. Restoring the density-gradient expansion for exchange in solids and surfaces. *Phys. Rev. Lett.* **2008**, *100*, 136406.

[11] Osada, Y.; Yu, Q. S.; Yasunaga, H.; Wang, F. S.; Chen, J. Preparation and electrical properties of polymeric TCNQ and TCNE films by plasma polymerization. *J. Appl. Phys.* **1988**, *64*, 1476–1483.

[12] Vincent, V. M.; Wright, J. D. Photoconductivity and crystal structure of organic molecular complexes. *J. Chem. Soc., Faraday Trans. 1* **1974**, *70*, 58–71.

[13] Dillon, R. J.; Bardeen, C. J. Time-Resolved Studies of Charge Recombination in the Pyrene/TCNQ Charge-Transfer Crystal: Evidence for Tunneling. *J. Phys. Chem. A* **2012**, *116*, 5145–5150.

SUMMARY

Hybrid halide perovskites are currently the most studied optoelectronic materials. They have been successfully employed as the active material in solar cells. Despite the achieved success of these materials, the properties of these hybrid frameworks of an inorganic lattice that includes organic cations are not fully understood. This is because of the multiple complex processes that are operative in these materials and it is very hard to unravel them just on basis of experiments. Therefore, computational studies of these materials are important to gain insight in the material structure, the electronic structure and the processes dictated by these properties. An additional advantage of computational studies is that properties can be predicted without actually making the materials in the lab. Such computational study thus give insights in the functioning of hybrid perovskite materials and gives directions to their further development. Of particular interest in this thesis is the role of the organic cation. In some earlier studies it has been pointed out that he role and presence of the organic cations is just limited to stabilizing the structure of hybrid perovskites without influencing the electronic energy states. In this thesis we examine the role of the organic cation in detail, demonstrating that the organic cation has a distinct effect on the electronic structure of hybrid halide perovskites.

In **Chapter 2** the influence of the orientation or direction of the organic cations on the electronic structure of three-dimensional hybrid perovskites is investigated. In a series of electronic structure calculations based on density functional theory it is shown that the substitution of cations with varying size and dipole moment in the lead iodide framework can have a pronounced effects on the electronic structure of the material. These modulations affect the size of the unit cell and also the Pb-I-Pb bond angles and thus have a direct effect on the electronic coupling between the lead and iodide orbitals. The relative orientation of the dipoles of the organic cations also affects the electronic structure and band gap of the material significantly. These effect were found to be stronger with organic cations having large dipole moment. The presence of antiparallel dipoles in the material can lead to localized electronic states of valence and conduction bands, induced by a non-uniform distribution of the electrostatic potential. These localized states can lead to localization of electrons and holes in different spatial part of the material. The localization of states is accompanied by an increase of the effective masses of these charge carriers.

In **Chapter 3** relation between the dynamics of the organic cation (methylammonium) in methylammonium lead iodide and the phase transitions observed in this materials are investigated. This study was performed using molecular dynamics simulations in which the interactions between the atoms a described using a simplified force field model. This allows the use of much larger systems, and in this work a system consisting of 1000 unit cells was considered. The simulations were performed at various temper-

atures varying over a range where structural phase transitions occur in methyl ammonium lead iodide. It was found that the force field model used gives a good description of the phase transitions observed in this material experimentally. The rotational dynamics of the organic cations were found to vary significantly with temperature and sharp phase transitions are observed at distinct temperatures. Methylammonium cations are shown to form organized domains in which the methylammonium cations arrange in an ordered, energetically favorable structure. This domain formation is already observed for model calculation including only dipole-dipole interactions. The domain formation effect becomes much stronger if the cations are embedded in the Pb-I lattice especially when the lattice is allowed to deform in reaction to the alignment. This shows that the phase transition is a concerted phenomenon of mutual alignment of the dipoles, both by interactions with neighboring dipoles and specific interactions between the methylammonium cations and the Pb-I lattice. Formamidinium based models were also studied and it was found that the contribution of dipole-dipole interactions in the non-dipolar formamidinium cation are negligible. The formation of domains still takes place in formamidinium based models and it is found that formation of hydrogen-bond like conformations plays an important role in formamidinium lead iodide, which, combined with increased steric interactions leads to slower rotation dynamics of formamidinium.

6

Experimentally, the materials that are most stable and result in the highest device efficiencies contain mixtures of multiple organic cations, for example mixtures of methylammonium (MA) and formamidinium (FA). In **Chapter 4** a molecular dynamics study of mixed organic cation $MA_{0.5}FA_{0.5}PbI_3$ hybrid perovskites is presented using the same molecular dynamics approach as used in Chapter 3. In order to unravel the interactions between the cations of different nature (MA vs. FA) seven different configurations of mixed cation systems were considered. In these seven configurations, the mixing of the two types of cations is systematically varied. The configurations range from fully mixed systems where each MA is surrounded by only FAs to a system where they are fully phase-separated. The simulations show that, based on these molecular dynamics simulations, the organ ic cations prefer a conformation where they are fully separated, i.e. MA prefers to be surrounded by other MA ions to minimize its energy. It is also shown that the dynamics of the organic cations is markedly affected by the mixing. This is, at least in part due to the effect of the interaction between the organic cation and the lead-halide cage.

In **Chapter 5** we explore the possibility to design novel two dimensional versions of hybrid halide perovskites based on density functional theory calculations. The electronic structure is studied of several newly proposed two-dimensional hybrid halide perovskites containing organic cations with specific functionality. Inclusion of organic cations with strongly electron accepting or donating character is shown to result in materials where the lowest conduction band is located in a different part of the materials than the highest conduction band. This may lead to enhanced charge separation upon photoexcitation. This computational study indicates that the organic cations in these materials can not just act as spacers separating inorganic layers but may effectively participate in their electronic properties.

In **Chapter 6** a computational study is presented of one-dimensional perovskite derivatives. DFT calculations have been performed on three different crystals. The first two are based on a dimethyl-aniline cation combined with SnI. Depending on the synthesis conditions, this can lead to a one-dimensional perovskite-like structure where SN-I octahedra are surrounded by dimethyl-aniline ions. These compounds are shown to give band structures where both the valence and conduction bands are mainly located in the Sn-I framework. Under different conditions, a non-perovskite structure is formed that does not contain SN but is a one-dimensional charge transfer salt, dimethy-aniline/triiodide. This compound has interesting properties such as a relatively low band gap and both the conduction bands and valence bands are mostly located on the triiodide. A third compound is a lead iodide based materials that contains the organic charge-transfer complex pyrene-TCNQ. This materials can form as a stable two-dimensional material in thin films but attempts to crystallize it lead to the formation of one-dimensional chains of Pb-I octahedra surrounded by the charge-transfer complexes. Interestingly, the top of the valence band in this material is localized on the Pb-I framework, while the bottom of the valence band is located on the TCNQ molecules.

SAMENVATTING

Hybride halogenide perovskieten zijn momenteel de meest bestudeerde opto-elektronische materialen. Ze zijn met succes toegepast als het actieve materiaal in zonnecellen. Ondanks het bereikte succes van deze materialen zijn de eigenschappen van deze hybriden van een anorganisch rooster dat organische kationen bevat, niet volledig begrepen. Dit komt door de vele complexe processen die in deze materialen een rol spelen en het vrijwel onmogelijk om ze alleen op basis van experimenten. Daarom zijn computer simulaties aan deze materialen belangrijk om inzicht te krijgen in de materiaalstructuur, de elektronische structuur en de processen die door deze eigenschappen worden bepaald. Een bijkomend voordeel van computer simulaties is dat eigenschappen kunnen worden voorspeld zonder de materialen in het laboratorium daadwerkelijk te maken. Een dergelijke computerstudie geeft dus inzicht in het functioneren van hybride perovskietmaterialen en geeft aanwijzingen voor hun verdere ontwikkeling. Van bijzonder belang in dit proefschrift is de rol van het organische kation. In sommige eerdere studies werd er op gewezen dat de rol en aanwezigheid van de organische kationen beperkt is tot het stabiliseren van de structuur van hybride perovskieten zonder de elektronische energietoestanden te beïnvloeden. In dit proefschrift onderzoeken we de rol van het organische kation in detail, wat aantoont dat het organische kation een duidelijk effect heeft op de elektronische structuur van hybride halogenide perovskieten.

In **Hoofdstuk 2** wordt de invloed van de oriëntatie of richting van de organische kationen op de elektronische structuur van drie-dimensionale hybride perovskieten onderzocht. In een reeks berekeningen van de elektronische structuur op basis van de dichtheidsfunctionaaltheorie wordt aangetoond dat de vervanging van kationen met variërende grootte en dipoolmoment in het lood-iodide framework een uitgesproken effect op de elektronische structuur van het materiaal kan hebben. Deze modulaties beïnvloeden de grootte van de eenheidscel en ook de Pb-I-Pb bindingshoeken en hebben dus een direct effect op de elektronische koppeling tussen de lood- en iodideorbitalen. De relatieve oriëntatie van de dipolen van de organische kationen beïnvloedt ook de elektronische structuur en band gap van het materiaal. Dit effect blijkt sterker te zijn met organische kationen met een groot dipoolmoment. De aanwezigheid van antiparallelle dipolen in het materiaal kan leiden tot gelokaliseerde elektronische toestanden van valentie- en geleidingsbanden, geïnduceerd door een niet-uniforme verdeling van de elektrostatische potentiaal. Deze gelokaliseerde toestanden kunnen leiden tot lokalisatie van elektronen en gaten in verschillende ruimtelijke delen van het materiaal. De lokalisatie van toestanden gaat gepaard met een toename van de effectieve massa's van deze ladingdragers.

In **Hoofdstuk 3** wordt de relatie tussen de dynamica van het organische kation

(methylammonium) in methylammonium-loodjodide en de fase-overgangen die in deze materialen worden waargenomen onderzocht. Deze studie werd uitgevoerd met behulp van moleculaire dynamica-simulaties waarin de interacties tussen de atomen beschreven met behulp van een vereenvoudigd 'force field'. Dit maakt simulaties veel grotere systemen mogelijk, en in dit werk werd een systeem bestaand uit 1000 eenheidscellen beschouwd. De simulaties werden uitgevoerd bij verschillende temperaturen die varieerden over een bereik waar structurele faseovergangen voorkomen in methylammonium-leadiodide. Er werd gevonden dat het gebruikte krachtveldmodel een goede beschrijving geeft van de faseovergangen die in dit materiaal experimenteel zijn waargenomen. De rotatiedynamica van de organische kationen bleek significant te variëren met de temperatuur en scherpe faseovergangen werden waargenomen bij verschillende temperaturen. Methylammoniumkationen blijken georganiseerde domeinen te vormen waarin de methylammoniumkationen zich in een geordende, energetisch gunstige structuur rangschikken. Deze domeinvorming is al waargenomen in modelberekening waar alleen dipool-dipool interacties worden meegenomen. De vorming van domeinen wordt veel sterker als de kationen worden ingebed in het Pb-I-rooster, in het bijzonder wanneer het rooster de gelegenheid krijgt om te vervormen in reactie op de uitlijning van de dipolen. Dit toont aan dat de faseovergang een samenspel is van de onderlinge uitlijning van de dipolen, zowel door interacties met naburige dipolen als door specifieke interacties tussen de methylammoniumkationen en het Pb-I-rooster. Op formamidinium gebaseerde modellen werden eveneens bestudeerd en er werd gevonden dat de bijdrage van dipool-dipool-interacties in het niet-dipolaire formamidiniumkation te verwaarlozen is. De vorming van domeinen vindt nog steeds plaats in op formamidinium gebaseerde modellen en er is gevonden dat vorming van waterstofbrug-achtige conformaties een belangrijke rol speelt in formamidinium-loodiodide, wat in combinatie met verhoogde sterische interacties leidt tot een langzamere rotatiedynamica van formamidinium.

Experimenteel bevatten de materialen die het meest stabiel zijn en resulteren in de hoogste zonnecel efficienties mengsels van meerdere organische kationen, bijvoorbeeld mengsels van methylammonium (MA) en formamidinium (FA). In **Hoofdstuk 4** wordt een moleculaire dynamica studie van gemengd organisch kation $MA_{0.5}FA_{0.5}PbI_3$ hybride perovskites gepresenteerd volgens dezelfde moleculaire dynamica benadering zoals gebruikt in **Hoofdstuk 3**. Om de interacties tussen de kationen van verschillende aard (MA versus FA) te ontrafelen, werden zeven verschillende configuraties van gemengde kationsystemen bestudeerd. In deze zeven configuraties wordt menging van de twee soorten kationen systematisch gevarieerd. De configuraties variëren van volledig gemengde systemen waarbij elke MA wordt omringd door alleen FA's tot een systeem waarbij de MA volledig is gescheiden van FA. De simulaties tonen aan dat, gebaseerd op deze moleculaire dynamica-simulaties, de organische kationen de voorkeur hebben voor een conformatie waar ze volledig gescheiden zijn, d.w.z. MA geeft er de voorkeur aan omgeven te zijn door andere MA-ionen om zijn energie te minimaliseren. Er wordt ook aangetoond dat de dynamica van de organische kationen duidelijk wordt beïnvloed door het mengen. Dit is, in elk geval gedeeltelijk, vanwege het effect van de interactie tussen het organische kation en de lood-halogenide-kooi.

In **Hoofdstuk 5** onderzoeken we de mogelijkheid om nieuwe twee-dimensionale versies van hybride halide perovskieten te ontwerpen op basis van dichtheidsfunctionaaltheorieberekeningen. De elektronische structuur is bestudeerd van verschillende nieuw voorgestelde tweedimensionale hybride halide perovskieten die organische kationen met specifieke functionaliteit bevatten. Opname van organische kationen met een sterk elektronenaccepterend of donerend karakter blijkt te resulteren in materialen waarbij de laagste geleidingsband zich in een ander deel van de materialen bevindt dan de hoogste geleidingsband. Dit kan leiden tot een verbeterde ladingsscheiding bij foto-excitatie. Deze computerstudie geeft aan dat de organische kationen in deze materialen niet alleen kunnen fungeren als spacers die anorganische lagen scheiden, maar effectief kunnen bijdragen aan hun elektronische eigenschappen.

In **Hoofdstuk 6** wordt een computationeel onderzoek gepresenteerd van eendimensionale perovskietderivaten. DFT-berekeningen zijn uitgevoerd op drie verschillende kristallen. De eerste twee zijn gebaseerd op een dimethyl-aniline-kation gecombineerd met SnI. Afhankelijk van de synthesevoorwaarden kan dit leiden tot een eendimensionale perovskietachtige structuur waarbij Sn-I-octaëders worden omringd door dimethylaniline-ionen. Van deze verbindingen wordt aangetoond dat ze bandstructuren geven waarbij zowel de valentie- als de geleidingsbanden zich hoofdzakelijk in het Sn-I-framework bevinden. Onder verschillende omstandigheden wordt een niet-perovskietstructuur gevormd die geen Sn bevat, maar een eendimensionaal 'charge-transfer complex', dimethy-aniline / triiodide. Deze verbinding heeft interessante eigenschappen zoals een relatief lage band gap en zowel de geleidingsbanden als valentiebanden bevinden zich meestal op het trijodide. Een derde verbinding is een op loodiodide gebaseerde materiaal die het organische 'charge transfer complex' pyreen-TCNQ bevat. Deze materialen kunnen zich vormen als een stabiel tweedimensionaal materiaal in dunne films, maar pogingen om het te kristalliseren leiden tot de vorming van eendimensionale ketens van Pb-I-octaëders omgeven door de ladingoverdrachtscomplexen. Interessant is dat de bovenkant van de valentieband in dit materiaal gelokaliseerd is op het Pb-I-framework, terwijl de laagste valentieband zich op de TCNQ-moleculen bevindt.

ACKNOWLEDGEMENTS

This thesis is very much a result of a team effort. The team constituted of people involved in my scientific and personal life. In one way or the other way, every encounter has affected me and hence this work. Therefore, I would not mention any individuals at this point. Nevertheless, I am taking the risk of singling out a few people and apologise to the uncredited. On the scientific side, I would like to thank first and foremost my promotor Dr. Ferdinand Grozema for arranging the necessary funding, for his supervision and trust that supported my growth as a researcher and for all his practical contributions to this thesis. I would like to thank the CSER program of SHELL FOM/NWO that enabled me to move to The Netherlands to pursue PhD at Delft. Moreover, my promotor Prof. Dr. Laurens Siebbeles deserves special thanks for cordially welcoming me in his group. Next in line, I would like to thank Dr. Tom Savenije and perovskite meetings for all the fruitful discussions about hybrid perovskites and research in general. I would like to thank all the collaborators who contributed in any form to the publications that built the basis for this thesis. Without Dr. Nicolas Renaud, Sayan Seal and Dr. Jörg Meyer, who helped me run the starting calculations in Chapters 2 to 4, this thesis would have been a lot thinner. I also cannot thank Nico and Jörg enough for my development as a computational chemist. Your patiently explaining me concepts behind the complicated parts of the calculations helped me build the foundations of this thesis. Likewise, I owe a thanks to Magnus Fridricksson for working on the dipole domains for Chapter 3. Finally, on the scientific side, I would like to thank all committee members for taking the time to evaluate this thesis.

On a personal side, I would like to thank Dengyang, Damla, Davide, Valentina, Kevin, Cansel, Maria and Silke for all our interesting talks, coffees and dinners. Of course, I am grateful to all other current and former members of the OM group for any help, advice, stimulation, conversation, cake, drink, etc., and, in general, for being such pleasant company. Thanks to all of you who enriched my life with our interaction. But most of all, I am immensely grateful to be utterly blessed with my ever supporting family.

मैं इस किताब को लिखने के समर्थन के लिए शुक्रगुज़ार हू अपने पिता, अमिता बुआ, तन्वी, नामित, स्वाति और सूर्य का|

A

APPENDIX TO CHAPTER 3

A.1. MOLECULAR DYNAMICS PARAMETERS

The force field used for the molecular dynamics (MD) simulations in Chapter 3 and 4 is composed of inorganic-inorganic interactions (U_{II}) which are in between the Pb-I atoms. These parameters are composed of Buckingham potential. The U_{II} parameters are mentioned in Table A.1 described by Equation A.1. The hybrid interactions (U_{IO}) which are in between the Pb-I atoms and the organic cations are described by mix of both Buckingham and Lennard-Jones potential described by Equations A.1 and A.2. The hybrid interaction parameters are mentioned both in Table A.2 and A.1. Parameters for U_{II} and U_{IO} are taken from the previous work of Mattoni et. al. and Bischak et. al. [1, 2] The U_{OO} term contains the intermolecular and intramolecular interactions of the organic cations and is described by the CHARMM force field that includes bonds, angles, dihedrals and impropers where applicable.[3–5] U_{OO} interaction parameters for methylammonium are mentioned in Table A.4 and the parameters for formamidinium are mentioned in Table A.6. The charges on each of these atoms are mentioned in Table A.3 for methylammoniumleadiodide and in Table A.5 for formamidiniumleadiodide. Both of these molecules have two different species of hydrogen where one is connected to Nitrogen (N) and another is connected to Carbon (C). These two types of hydrogens are named as HC (connected to C) and HN (connected to N).

$$U(r) = Ae^{-r\rho} - \frac{C}{r^6} \tag{A.1}$$

$$U(r) = 4\epsilon[(\frac{\sigma}{r})^{12} - (\frac{\sigma}{r})^{6}] \tag{A.2}$$

A.2. DIRECTIONAL SCATTER PLOTS

A

Table A.1: Buckingham Pairing coefficients

Pairs	$A(Kcal/mol)$	ρ (Å)	C (Å^6 $*$ $Kcal/mol$)
Pb-Pb	70359906.62970	0.13126	0.00000
Pb-I	103496.13301	0.32174	0.00000
I-I	22793.33858	0.48222	696.94954
Pb-N	32690390.93800	0.15095	0.00000
Pb-C	32690390.93800	0.15095	0.00000
I-N	112936.71421	0.34243	0.00000
I-C	112936.71421	0.34243	0.00000

Table A.2: Lennard Jones Pairing coefficients

Pairs	$\epsilon(Kcal/mol)$	σ (Å)
Pb-HN	0.01400	2.26454
Pb-HC	0.01400	2.70999
I-HN	0.05740	2.75000
I-HC	0.05740	3.10000
C-HN	0.04140	2.23440
C-HC	0.04140	2.67980
N-HN	0.05170	2.15950
N-HC	0.05170	2.60500
HN-HC	0.01570	1.51450
C-N	0.13640	3.32480

Table A.3: Partial charges used for MAPI

Species	Pb	I	HN	N	C	HC
Charges	2.030	-1.130	0.540	-1.100	0.771	0.023

Table A.4: Molecular parameters used for MA

Bond Coefficients				
Bonds	$K\,(Kcal/mol/Å^2)$	r_0 (Å)		
C-HC	342.991	1.093		
N-HN	443.528	1.028		
C-N	276.638	1.48		
Angle Coefficients				
Angles	$K\,(Kcal/mol/rad^2)$	ϕ_0 °		
HC-C-HC	37.134	108.836		
HN-N-HN	41.596	107.787		
HN-N-C	41.452	111.206		
HC-C-N	62.754	106.224		
Dihedral Coefficients				
Dihedrals	$K\,(Kcal/mol)$	n	d°	weighing factor
HN-N-C-HC	0.13	3	0	0

Table A.5: Partial charges used for FAPI

Species	Pb	I	HN1	HN2	N	C	HC
Charges	2.030	-1.130	0.514	0.549	-0.759	0.515	0.238

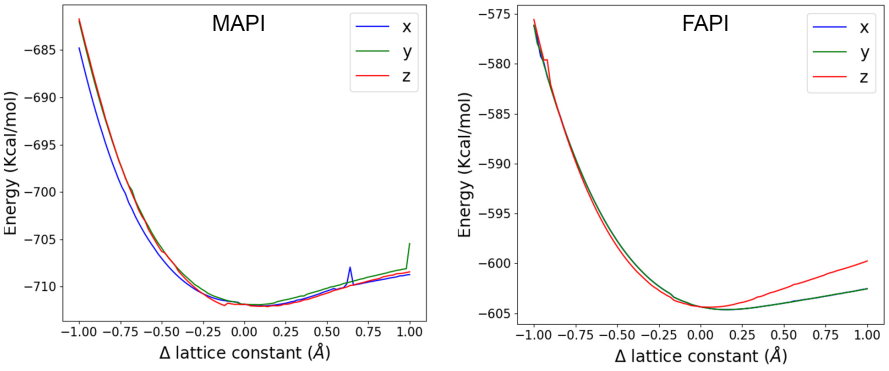

Figure A.1: Model validation calculation, (left) Energy with change of lattice constant for MAPI and (right) Energy with change of lattice constant for FAPI.

A

Table A.6: Molecular parameters used for FA

Bond Coefficients				
Bonds	$K\,(Kcal/mol/Å^2)$		r_0 (Å)	
C-HC	405.386		1.076	
N-HN	485.340		1.014	
N-C	520.100		1.319	
Angle Coefficients				
Angles	$K\,(Kcal/mol/rad^2)$		ϕ_0 °	
C-N-HN	47.713		119.499	
HN-N-HN	25.548		117.729	
N-C-HC	48.505		116.747	
N-C-N	61.531		126.476	
Dihedral Coefficients				
Dihedrals		$K\,(Kcal/mol)$	n	d°
HN-N-C-N	1	0.137	1	0
	2	4.013	2	180
	3	0.346	3	0
HN-N-C-HC	1	-0.134	1	0
	2	4.038	2	180
	3	-0.403	3	0
Improper Coefficients				
Angles	$K\,(Kcal/mol/rad^2)$		ϕ_0 °	
C-N-N-HC	2.735		0	
HN-C-HN-N	1.439		0	

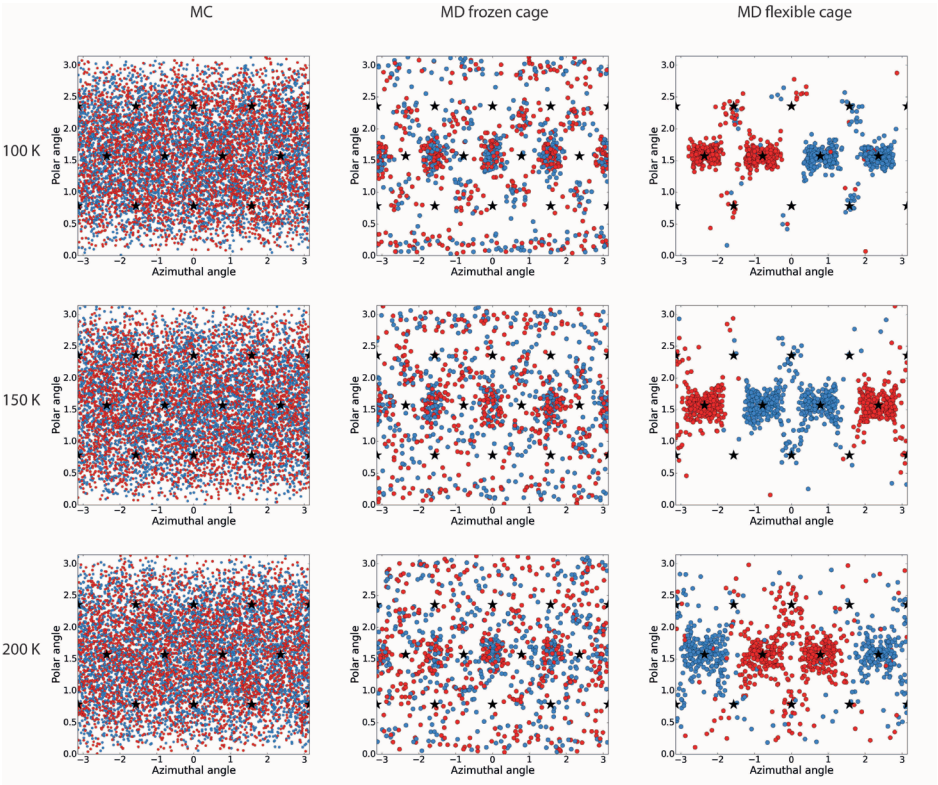

Figure A.2: Directional scatter plots of Methylammonium dipoles simulated with MC, MD with frozen cage and MD with flexible cage. The temperature ranges from 100 K to 200 K with a 50 K interval.

A

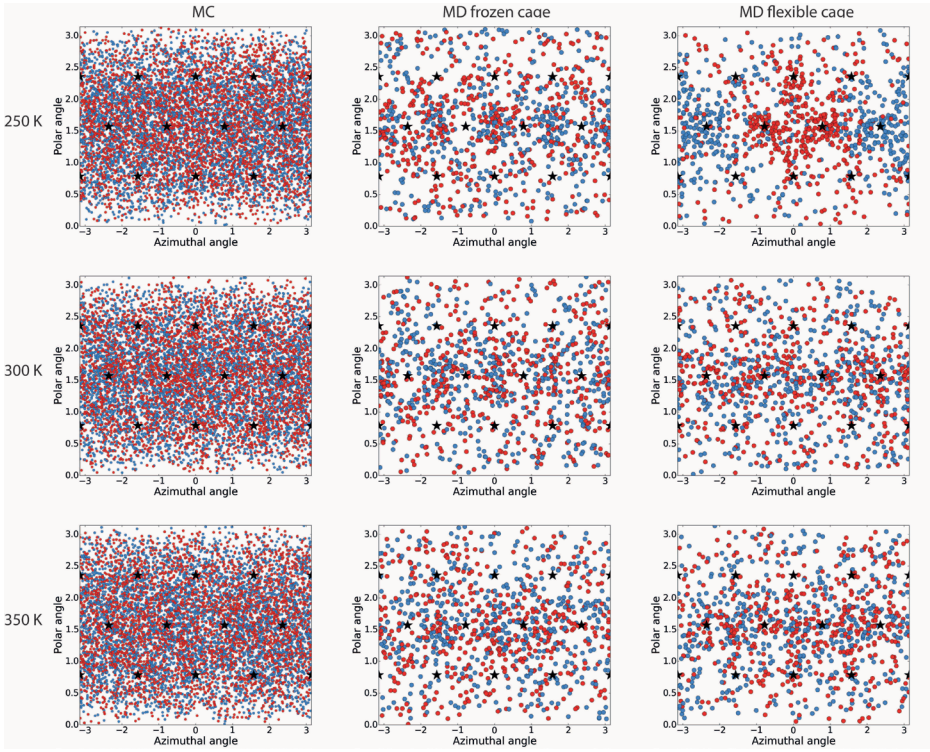

Figure A.3: Directional scatter plots of Methylammonium dipoles simulated with MC, MD with frozen cage and MD with flexible cage. The temperature ranges from 200 K to 350 K with a 50 K interval.

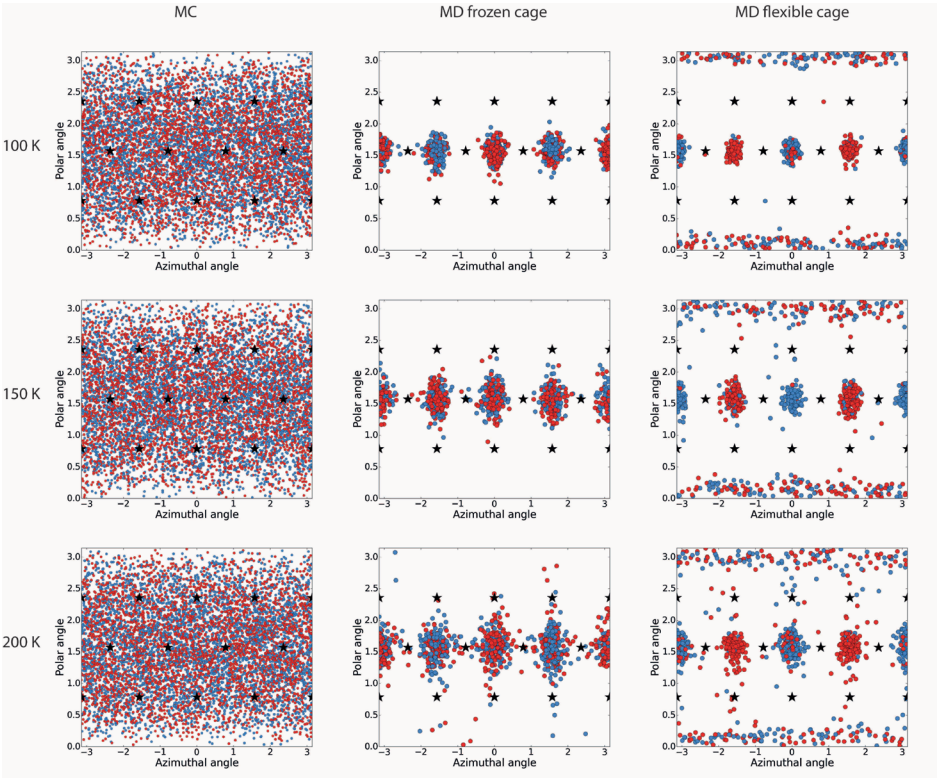

Figure A.4: Directional scatter plots of Formamidinium dipoles simulated with MC, MD with frozen cage and MD with flexible cage. The temperature ranges from 100 K to 200 K with a 50 K interval.

A

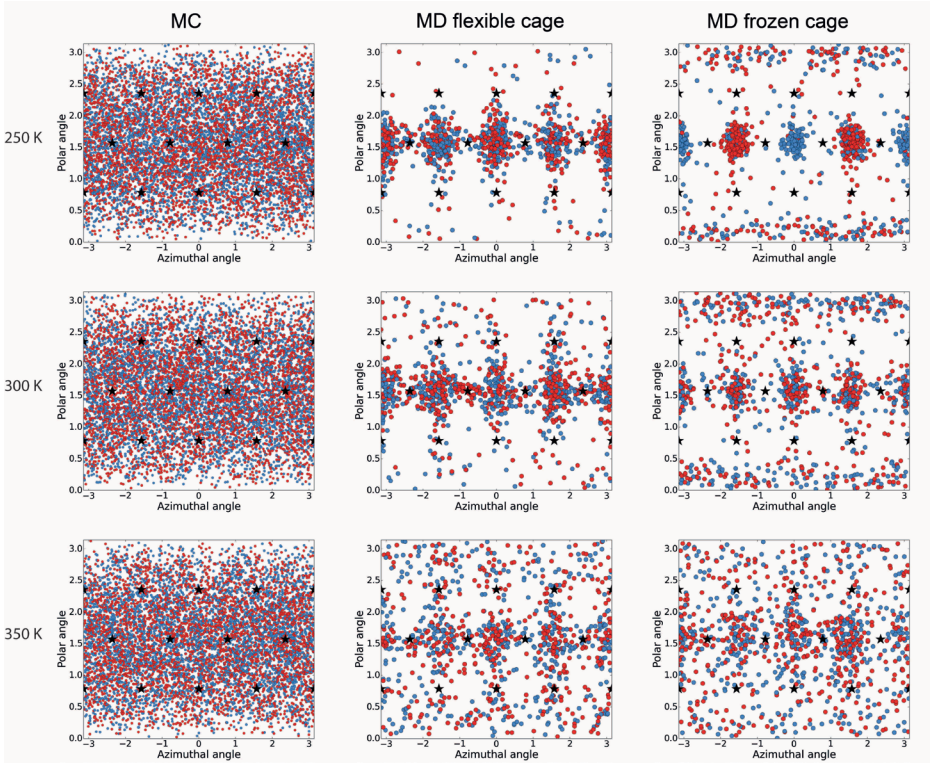

Figure A.5: Directional scatter plots of Formamidinium dipoles simulated with MC, MD with frozen cage and MD with flexible cage. The temperature ranges from 200 K to 350 K with a 50 K interval.

REFERENCES

[1] Mattoni, A.; Filippetti, A.; Saba, M. I.; Delugas, P. Methylammonium Rotational Dynamics in Lead Halide Perovskite by Classical Molecular Dynamics: The Role of Temperature. *The Journal of Physical Chemistry C* **2015**, *119*, 17421–17428.

[2] Bischak, C. G.; Hetherington, C. L.; Wu, H.; Aloni, S.; Ogletree, D. F.; Limmer, D. T.; Ginsberg, N. S. Origin of Reversible Photoinduced Phase Separation in Hybrid Perovskites. *Nano Letters* **2017**, *17*, 1028–1033.

[3] Vanommeslaeghe, K.; Hatcher, E.; Acharya, C.; Kundu, S.; Zhong, S.; Shim, J.; Darian, E.; Guvench, O.; Lopes, P.; Vorobyov, I.; Mackerell Jr., A. D. CHARMM general force field: A force field for drug-like molecules compatible with the CHARMM all-atom additive biological force fields. *Journal of Computational Chemistry* **2010**, *31*, 671–690.

[4] Vanommeslaeghe, K.; MacKerell, A. D. Automation of the CHARMM General Force Field (CGenFF) I: Bond Perception and Atom Typing. *Journal of Chemical Information and Modeling* **2012**, *52*, 3144–3154.

[5] Vanommeslaeghe, K.; Raman, E. P.; MacKerell, A. D. Automation of the CHARMM General Force Field (CGenFF) II: Assignment of Bonded Parameters and Partial Atomic Charges. *Journal of Chemical Information and Modeling* **2012**, *52*, 3155–3168.

CURRICULUM VITÆ

Sudeep MAHESHWARI

Sudeep Maheshwari, was born on July 8, 1990 in Farrukhabad (Uttar Pradesh), India where he did his schooling until he was nine. After that he moved to Jaipur with his parents. The later part of his schooling was in India International School, Jaipur. During this time he prepared for engineering entrance exams and cleared the IIT-JEE exam. With his high rank in the exam and his interests in Physics and Chemistry, he got a seat in the Integrated BS-MS program in Indian Institute of Science Eucation and Reseach Mohali. During his studies in Mohali he worked with leading scientists in short research projects in the field of Quantum chemistry and Material synthesis. This shaped his interests to work on novel research. Sudeep chose to do masters in Chemistry and his final year thesis was based on Computational study of C–H···F–C hydrogen bonds under the supervision of Dr. A. R. Choudhury. After completing his studies of Master in Chemistry, he got an offer to work at Shell technology centre in Bangalore in Computational Centre of Excellance team. His work here was modeling systems of fuels under the supervision of Dr. F. Thakkar and Dr. I. Rudra. During his work at Shell, he got a seat in the prestigious SHELL-CSER program to pursue a PhD in Delft University of Technology, The Netherlands. Subsequently, from April 2015 to April 2019, he was a PhD student at the Optoelectronic Materials Section at Delft University of Technology. Here, he carried out computational research on hybrid halide perovskite materials under the supervision of Dr. F.C. Grozema. During his PhD he got an exposure to many different aspects of computational modeling, simulations and artificial intelligence. After finishing his thesis he got an offer from the financial risk modeling team of ABN AMRO Bank in Amsterdam to work on risk models. He is currently working there as a Quantitative Risk Analyst.

LIST OF PUBLICATIONS

6. **Submitted:** M. Nadège, W. V. Gompel, M. C. Gélvez-Rueda, K. Vandewal, K. V. Hecke, H. Boyen, B. Conings, R. Herckens, **S. Maheshwari**, L. Lusten, C. Quarti, F. C. Grozema, D. Vanderzande, D. Beljonne, *Lead-halide perovskites meet donor-acceptor charge-transfer complexes*, Chem. Mater.

5. **S. Maheshwari**, S. Patwardhan, G. C. Schatz, N. Renaud, and F. C. Grozema, *The effect of the magnitude and direction of the dipoles of organic cations on the electronic structure of hybrid halide perovskites*, Phys. Chem. Chem. Phys. **21**, 16564-16572 (2019).

4. M. E. Kamminga, M. C. Gélvez-Rueda, **S. Maheshwari**, I. S. van Droffelaar, J. Baas, G. R. Blake, F. C. Grozema and T. T. M. Palstra, *Electronic mobility and crystal structures of 2,5-dimethylanilinium triiodide and tin-based organic-inorganic hybrid compounds*, J. Solid State Chem. **270**, 593-600 (2019).

3. **S. Maheshwari**, M. B. Fridriksson, S. Seal, J. Meyer and F. C. Grozema, *The Relation between Rotational Dynamics of the Organic Cation and Phase Transitions in Hybrid Halide Perovskites*, J. Phys. Chem. C **123**, 23, 14652–14661 (2019).

2. **S. Maheshwari**, T. J. Savenije, N. Renaud, and F. C. Grozema, *Computational Design of Two-Dimensional Perovskites with Functional Organic Cations*, J. Phys. Chem. C **122**, 30, 17118–17122 (2018).

1. S. Dev, **S. Maheshwari** and A. R. Choudhury, *Insights into the C–H···F–C hydrogen bond by Cambridge Structural Database analyses and computational studies*, RSC Adv. **5**, 26932-26940 (2015).